University of Southampton

National Oceanography Centre

Diabatic Eddies in Idealised Channel Models

Thesis for the degree of Doctor of Philosophy

Author:
Helen Burns

Supervisors:
Sybren Drijfhout and
Alberto Naveira Garabato

6th June 2018

Abstract

UNIVERSITY OF SOUTHAMPTON

FACULTY OF NATURAL AND ENVIRONMENTAL SCIENCES

National Oceanography Centre

Doctor of Philosophy

Diabatic eddies in idealised channel models

by Helen Burns

The Southern Ocean is a unique and climatically important region where mesoscale eddies are of first order importance. The circulation of the Southern Ocean controls the amount of carbon stored in the ocean and is an integral part of the worlds global overturning circulation. It is therefore of great importance to understand the dynamics of the Southern Ocean and the possible response of the overturning circulation to changing forcing i.e. climate change. Because of the role eddies play in setting that circulation, the dynamics are still not fully understood.

This thesis explores one poorly understood aspect of the Southern Ocean; diabatic eddies. Using the Massachusetts Institute of Technology General Circulation Model (MITgcm) to set up an idealised channel we close the northern boundary which causes the Southern Ocean overturning to collapse. This is to be expected as the circulation is part of the global overturning and must be connected to the rest of the world's ocean. We use Transformed Eulerian Mean (TEM) theory to suggest this collapse is achieved via diabatic eddies altering the effective surface buoyancy forcing. We then alter the northern boundary condition to show that diabatic eddies can be related to the northern boundary stratification. However the response of the diabatic eddies is also dependent on the surface forcing, particularly the sense of the forcing: changing from fixed-fluxes to surface restoring can have dramatic effects. Surface restoring alters the dynamics of the mixed layer, eddy compensation and saturation. This suggests that when exploring Southern Ocean dynamics in regional models, the effect of the imposed boundary conditions must always be considered. Our results suggest if the background stratification is altered we may see a very different circulation in the Southern Ocean, but to what extent would also depend on the response of the atmosphere and hence the surface forcing.

Acknowledgements

I would like to thank my supervisor, Sybren Drijfhout for many helpful discussions over the years. I would also like to thank Jeff Blundell who has given hours of his time imparting some of his vast knowledge of ocean modelling to me and training a PhD student how to use super computers and what all these flags and compilers mean! Thanks also to Jeff for wrangling me advance testing access to both Iridis 4 and Mobilis in order to test out many different set ups and simulations. I would also like to thank Dave Munday for all the helpful suggestions in the troubleshooting phase of model set up. I'm also grateful for the NERC studentship that allowed this work to be done and funded a number of conferences to engage in stimulating discussion with scientists across the world. I have much gratitude to the whole open source community, thanks to the 1000s of people that have worked and contributed to the MITgcm, python and Ubuntu to allow research like this to be completed.

Over the past 4 years I have enjoyed great company in the office, keeping me fuelled with coffee and banding together against the weather elements (when it rained indoors). These years have been a pleasure to spend with Matt, Zoe and Jon and great to welcome the new faces of Jess and Sam who have put up with whining final year PhDs! I would also like to thank the many great friends I've met at NOC, in particular: Anna who's kept me active climbing, Maike who shares my love of gin and intolerance of gluten and Jesse who has put up with me and supported me over the last couple years! Lastly I'd like to thank my parents who have supported me greatly throughout my whole life always giving me love and encouragement. A huge thank you to my dad for proof reading this entire thesis while fighting off cancer: a total hero.

Academic Thesis: Declaration Of Authorship

I, Helen Burns, declare that this thesis and the work presented in it are my own and has been generated by me as the result of my own original research.

I confirm that:

1. This work was done wholly or mainly while in candidature for a research degree at this University;

2. Where any part of this thesis has previously been submitted for a degree or any other qualification at this University or any other institution, this has been clearly stated;

3. Where I have consulted the published work of others, this is always clearly attributed;

4. Where I have quoted from the work of others, the source is always given. With the exception of such quotations, this thesis is entirely my own work;

5. I have acknowledged all main sources of help;

6. Where the thesis is based on work done by myself jointly with others, I have made clear exactly what was done by others and what I have contributed myself;

7. Either none of this work has been published before submission, or parts of this work have been published as:

Signed:_____

Date:_____

Contents

List of Tables

List of Figures

Symbolslist

Symbol	Description	Unit
C_p	Specific heat capacity	$\mathrm{JKg}^{-1}K^{-1}$
D	Material derivative	
Ek	Ekman number	
$F()$	Function (variables)	
H	Water Depth	m
J	Jacobian	
K	Eddy transfer coefficient	
N^2	Brunt Väisälä frequency	s^{-1}
N_d	Stratification depth	m
P_b	Bottom Pressure	$\mathrm{N/m}^2$
Q	Heat Flux	$\mathrm{W/m}^2$
Ro	Rossby number	
S_p	Isopycnal slope	
T	Temperature	K or ^{o}C
Ψ	Stream function, * denotes eddy, $_{res}$ denotes and an over bar denotes time mean Eulerian	m^2 /s
α	thermal expansion	K^{-1}
β	Coriolis ratio	$m^{-1}s^{-1}$
χ	Sources and sink term	
η_b	Bottom topography	m
η	Sea Surface Height	m
κ	Eddy diffusivity constant	m^2s^{-1}
$\mathbf{\Omega}$	Earth rotation vector	s^{-1}
∇	Gradient operator $\left(\frac{\partial}{\partial x}, \frac{\partial}{\partial y}, \frac{\partial}{\partial v}\right)$	m^{-1}
$\mathcal{B}$	Buoyancy forcing	

Symbol	Description	Unit
$\mathcal{G}$	Source term e.g. temperature or density	K kg $m^{-3}s^{-1}$
$\mathcal{O}$	Of order of magnitude	
$\nabla \times \tau_s$	Wind Stress Curl	
π	Geometrical value Pi	
ρ	Density, $_0$ denotes reference density.	kg/m^2
τ_r	Relaxation timescale	s
τ_s	Wind Stress	N/m^2
θ	Potential temperature	^{o} C
$'$	denotes deviation from mean	
$_a$	denotes ageostophic	
b	buoyancy	ms^{-2}
f	coriolis frequency	s^{-1}
g	gravitational acceleration	ms^{-2}
hml	Mixed layer Depth	m
p		Nm^{-2}
q	potential vorticity	$m^{-1}s^{-1}$
t	time	s
xyz	x=zonal distance, y=meridional distance, w=vertical distance	m or km
$\mathbf{u}$	Velocity vector (x,y,z,t), u=zonal, v=meridional, w=vertical	m/s
L	Length	m

Acronyms

AABW Antarctic Bottom Water.

AAIW Antarctic Intermediate Water.

AC14 Abernathy and Cessi 2014.

ACC Antarctic Circumpolar Current.

AMOC Atlantic Meridional Overturning Circulation.

APE Available Potential Energy.

CDF Cumulative Distribution Frequency.

CDW Circumpolar Deep Water.

CFL Courant Friedrich Lewy.

DIC Dissolved Inorganic Carbon.

EKE Eddy Kinetic Energy.

EOS Equation of State.

EPE Eddy Potential Energy.

FORTRAN Formula Translating System.

GCM General Circulation Model.

GPE Gravitational Potential Energy.

KE Kinetic Energy.

KPP K-profile parameterization.

LCDW Lower Circumpolar Deep Water.

L.H.S Left Hand Side.

MITgcm Massachusetts Institute of Technology General Circulation Model.

MOC Meridional Overturning Circulation.

NADW North Atlantic Deep Water.

NCEP National Centers for Environmental Prediction.

NERC Natural Environment Research Council.

netCDF Network Common Data Form.

NOC National Oceanography Centre.

OSMP7 One Step Monotonicity Preserving 7th order.

PF Polar Front.

PV Potential Vorticity.

QG Quasi-Geostophic.

QGPV Quasi-Geostophic Potential Vorticity.

RBCS Relaxed Boundary Condition Scheme.

R.H.S Right Hand Side.

RMOC Residual Meridional Overturning Circulation.

ROC Residual Overturning Circulation.

SAF Southern Antarctic Front.

SAM Southern Annular Mode.

SAMW Sub Antarctic Mode Water.

SO Southern Ocean.

SO ROC Southern Ocean Residual Overturning Circulation.

SSH Sea Surface Height.

SST Sea Surface Temperature.

STEM Statistical Transformed Eulerian Mean.

TEM Transformed Eulerian Mean.

TKE Turbulent Kinetic Energy.

U Zonal Velocity in m/s.

UCDW Upper Circumpolar Deep Water.

V Meridional Velocity in m/s.

Chapter 1

Introduction

Overview

The Southern Ocean (SO) is unique, containing a band of latitudes where there is no mean water depth shallower than 1800 m (*Hallberg and Gnanadesikan*, 2006). Strong polar Westerlies allow for a strong zonal Antarctic Circumpolar Current (ACC) that flows Eastwards around the continent between 56°& 62°S (*Johnson and Bryden*, 1989). This lack of topography and zonal flow results in unique dynamics that play an important role in connecting all the ocean basins as well as completing the global Meridional Overturning Circulation (MOC) (*Marshall and Speer*, 2012) as seen in Fig. 1.1. The Southern Ocean is an important sink of CO_2 with the ACC accounting for around 40% of the global uptake (*Mignone et al.*, 2006).

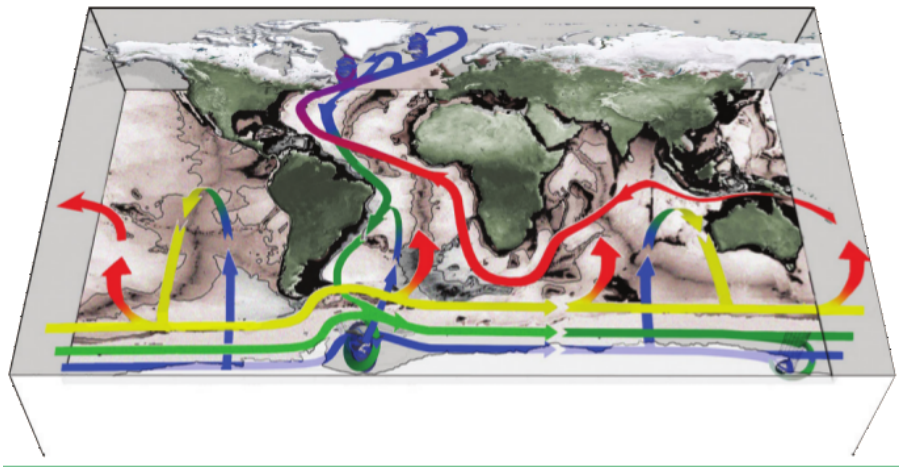

Figure 1.1: The Southern Ocean's role in the global overturning. A schematic from *Marshall and Speer* (2012), with blues and purples representing denser water masses and reds and yellows less dense water masses.

Changes in the Southern Ocean overturning would alter the Southern Ocean carbon sink changing the upwelling of deep waters rich in Dissolved Inorganic Carbon (DIC), and altering the partial pressure of CO_2 in the ocean. Between 1981 and 2004 the Southern Ocean sink decreased by 0.08 petagrams of C per year attributed to increased wind stress, showing that the CO_2 sink cannot be assumed to stay constant (*Le Quéré et al.*, 2007). This has been reinvigorated after 2002 as the Southern Ocean sink began to increase due to decadal variability (*Landschützer et al.*, 2012).

However, the dynamics of the Southern Ocean are complex and poorly understood, with sparse observations in time and space. It is therefore of great interest to fully understand the dynamics of the Southern Ocean and the response to future climate change. Of particular interest in this thesis is how changes in the Northern Hemisphere might alter the SO. Inter-hemispheric links between the SO ROC and Northern Hemisphere circulation were demonstrated in a number of studies (*Gnanadesikan and Hallberg*, 2000; *Wolfe and Cessi*, 2011). We wish to identify the SO processes involved in this connection. First, we give a basic overview of Southern Ocean dynamics and theory to give context for our investigations before outlining modelling techniques used to investigate them.

1.1 Introduction to Southern Ocean Dynamics

As the SO plays such a vital role in heat and carbon transport and the global overturning circulation there has been much interest over the years to understand its complex dynamics and how the circulation might change in response to a changing climate. The SO is weakly stratified with wind stress generating very strongly tilted isopycnals across the ACC due to a lack of continental boundaries. This large isopycnal tilt supports a large geostrophic flow in the ACC and provides a route for deep water to move along isopycnals towards the surface. Many isopycnals outcrop and this allows for many density classes to feel direct buoyancy and momentum forcing from the atmosphere, allowing forcing of density classes well below the thermocline.

Wind stress is around a maximum at 50^oS, which corresponds to a change in sign of wind stress curl ($\nabla \times \tau$). The Southern Hemisphere westerly τ is associated with equatorward Ekman transport, this leads to a surface divergence where the $\nabla \times \tau < 0$ and convergence where $\nabla \times \tau > 0$. Thus, a weak vertical velocity shoals isopycnals to the south and depresses them to the north, critical for the ACC and the overturning circulation. In the Northern Hemisphere mid-latitudes

this is balanced by the development of a mean meridional velocity supported by a zonal pressure gradient, that relaxes isopycnal tilt. In the SO, there is no zonal pressure gradient to force a mean meridional flow. However, some local anomalies in the zonal pressure gradient do arise and are crucial for the ACC.

1.1.1 Eddies in the Southern Ocean

Eddies play a significant and vital role in the SO. In this thesis turbulent flows on spatial scales greater than or equal to the Rossby radius $\mathcal{O}$ (10km) in the SO are referred to as mesoscale eddies, distinct from the mean flow by spatial and temporal perturbations rather than coherent eddies alone. We will denote eddy components using a prime ($'$) symbol to indicate a deviation from the time mean.

Oceanic eddies derive their energy primarily from baroclinic and barotropic instability which has an important impact on the large scale circulation. In principle, energy exchange between waves and mean flow can take place in both directions (to and from the mean flow). The energy exchange related to the Reynolds stress ($\overline{u'v'}$) takes both signs, whereas the term related to the horizontal eddy density flux ($\overline{v'\rho'}$) is predominantly positive so that energy is transferred from the mean flow to the waves, meaning that the mean flow is unstable to small perturbations. Two physically different mechanisms can be distinguished, corresponding to energy transfer, namely barotropic and baroclinic instability, both of which are important. Sloping isopycnals act as a source of potential energy which can be released as kinetic energy. If two fluid parcels are exchanged and a denser fluid parcel sinks to be replaced with less dense fluid then kinetic energy is released through a vertical exchange or fluid parcels can move along a sloping path between isopycnals maximising at a slope of half that of the isopycnal slope in a slantwise exchange. The slantwise exchange normally transfers heat poleward. This occurs through baroclinic instability.

Eddies can also be generated through time varying winds as well as horizontal shear in the horizontal velocity though barotropic instability. Barotropic instability is associated with the engergy conversion term:

$$-\frac{\partial U}{\partial y} < u'v' >$$

and can only occur if there is a horizontal shear of the background velocity i.e.

$$-\frac{\partial U}{\partial y} \neq 0.$$

Since no vertical shear of U is needed (in contrast to baroclinic instability) a barotropic background current can produce the instability. Analysis of the energetics of the mean current shows that the energy is exchanged with the kinetic energy of the mean flow.

One of the important consequences of barotropic instability is that flows with small length scales are likely to be unstable. In fact, it can be shown that interacting short Rossby waves are unstable (*Gill et al.*, 1974), which helps to explain the turbulent nature of mesoscale motions in the ocean.

With both sloping isopycnals and strong barotropic flows, there is a very large amount of eddy activity in the SO playing an important role in both the ACC and the SO overturning.

1.1.2 Meridional Overturning Circulation

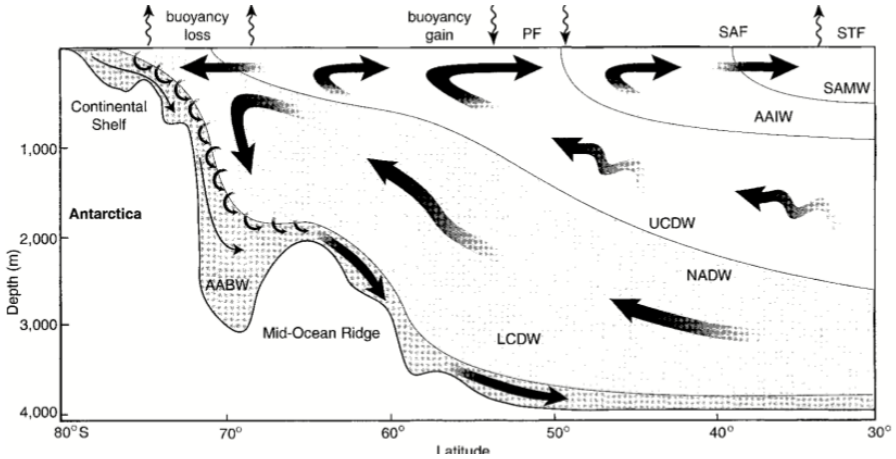

Figure 1.2: Southern Ocean circulation schematic from *Speer et al.* (2000). Showing the main water masses and overturning circulations with the buoyancy forcing. Acronyms are defined in the glossary section for reference.

One of the motivations of this work is to understand the overturning response to altered ocean physics to begin to understand how this might change in future climates. A general schematic is shown in Fig. 1.2 consisting of upper and lower cells that are counter rotating (*Meredith et al.*, 2012). In the lower cell North Atlantic Deep Water (NADW) upwells near Antarctica and is converted to Antarctic Bottom Water (AABW) that sinks to the deep ocean. In the upper cell, the upwelling water is converted into Antarctic Intermediate Water (AAIW) and Sub Antarctic Mode Water (SAMW) through the addition of heat and fresh water in the surface waters, which have a northward Ekman flow. The upper cell is controlled by eddy

and air-sea forcing (*Rintoul et al.*, 2012) and this upper cell is the main focus of the overturning in this thesis.

It used to be thought that there was a strong diapycnal overturning circulation driven by winds called the Deacon cell (*Döös and Webb*, 1994). However strong polar westerlies drive a mean Ekman overturning circulation ($\overline{\Psi}$) that in turn steepens isopycnals while baroclinic instability drives an opposing eddy-induced circulation (Ψ^*) (*Marshall and Radko*, 2003), this is shown in eddy permitting and resolving models *Hallberg and Gnanadesikan* (2006). This partly compensates the Ekman circulation leading to a small residual circulation that acts to advect tracers along mean isopycnals (*Speer et al.*, 2000):

$$\psi_{res} = \underbrace{\overline{\psi}}_{mean} + \underbrace{\psi^*}_{eddy}. \tag{1.1}$$

Exactly how eddies interact to contribute to the mean flow is outlined in section 1.2.3. Due to this residual nature of the SO overturning the Meridional Overturning Circulation is referred to as the SO ROC. This simple residual-mean decomposition allows for the parameterisation of eddies combining Gent-McWilliams and Green and Stone schemes (*Visbeck et al.*, 1997). *Toggweiler and Russell* (2008), *Marshall and Radko* (2003) and *Speer et al.* (2000) showed that in the limit of weak interior diapycnal mixing the SO ROC transport must be along mean isopycnal surfaces and can only cross isopycnals in the surface diabatic layer and by deep convective mixing outside the SO to connect the surface branch with the deep branch Fig. 1.2. This limit does not apply to the deep cell of the SO ROC, associated with Antarctic Bottom Water formation, but is relevant for the pole-to-pole overturning circulation associated with North Atlantic Deep Water formation (*Wolfe and Cessi*, 2011). These parametrisations which have been refined over the years (*Jansen et al.*, 2015, e.g.), but all assume largely adiabatic eddy fluxes.

Some models show up to a 70% disparity in models using full eddy compensation or no eddy compensation, which would have major implications for future anthropogenic CO_2 uptake (*Le Quéré et al.*, 2007).

1.1.3 Antarctic Circumpolar Current

In contrast to gyre circulations strong zonal flows are parallel to wind forcing $\mathbf{u} \cdot \tau_s$ generating the ACC, the Worlds longest and strongest current system, extending 24,000 km long and around 137$\pm$ 7 Sv (*Meredith and Woodworth*, 2011). Like much of SO dynamics the ACC is also unique, barotropically flowing eastward at almost

all depths [1]. Although the ACC is actually composed of filaments of jet streams bound by fronts, the ACC is often simplified to one flow that can be approximated in a model by channel domain with periodic flow in the zonal direction. From a momentum balance, Eq. (1.2), it can be seen that wind stress is balanced by bottom form stress that arises from correlation between zonal gradients in bottom topography and pressure anomalies.

$$\overline{\tau}^{x}_{wind} = p_b \overline{\frac{\partial \eta_b}{\partial x}}, \tag{1.2}$$

where τ^x_{wind} is the zonal wind stress, P_b is bottom pressure and η_b is the bottom topography. High pressure anomalies in SSH are found upstream of bathymetric features and low pressure anomalies are found in lee of topography. The bottom form stress transfers momentum directly from the ocean into the solid earth. If topography is removed the ACC is seen to be roughly an order of magnitude larger than the observed values as first pointed out in *Munk and Palmén* (1951).

1.1.4 Eddy saturation.

In recent years there has been much debate on the response of the ACC and SO ROC to increasing wind stress associated with a strong positive trend in the Southern Annular Mode (SAM) index (*Thompson and Solomon*, 2002); this has been one of the strongest observed climatic trends (*Sallée et al.*, 2010). However, longer time series of the SAM index and the inclusion of satellite observations show large inter annual and decadal variability and suggests this trend is not as dramatic as it first appeared in the late 1990s (*Hogg et al.*, 2015). None the less, variations in response between the ACC and the SO overturning to intensification of the polar westerlies allowed for a lot of research into the mechanisms of eddies in the SO and their role in SO dynamics. With increasing wind stress there has been little response observed in isopycnal slope (*Böning et al.*, 2008). It is thought there is a near linear response in EKE to increased τ_s. Rather than accelerating the ACC transport, the momentum imparted by the wind is transferred to the bottom via interfacial form stress (*Meredith and Hogg*, 2006) (eddy saturation). *Morrison and Hogg* (2013) showed a marked difference between eddy saturation and eddy compensation (Ekman cancelling), indicating the differing depth scales for eddy driving of ACC and overturning can lead to differing responses to changing momentum forcing. Making the ACC response to altered forcing a worthwhile investigation as it may not have a similar response to the SO ROC.

[1] Surface pressure gradient and stratification yields a positive shear to reduce the velocity with depth but, rarely enough to lead to a reversal.

1.2 Residual Mean and Transformed Eulerian Mean Theory

Due to the unique dynamics of the SO the large scale mean circulation is influenced by the small scale time-varying components. If the zonally averaged time mean velocity on z-level is used to calculate the overturning the fictitious Deacon cell is found rather than the true overturning circulation (*Döös and Webb*, 1994). Most of the Deacon cell overturning circulation is due the east-west isopyncal slope associated with standing eddies and ocean gyres and in fact there is not cross isopycnal flow associated with it (*Ballarotta et al.*, 2013). Therefore, time varying eddies need to be taken into account to establish the residual circulation. Thus, SO dynamics must be approached in terms of residuals which will be done throughout this thesis and the background theory is outlined here.

1.2.1 Assumptions and Approximations:

When investigating the complex theory behind Southern Ocean dynamics we must consider approximations in order arrive at a system that can be analysed more easily focusing on desired processes. As these approximations impose constraints on the relationships derived it is important to be aware of the approximations used and the limitations they may impose on the resulting equations.

Boussinesq Approximation

We assume a Boussinesq fluid (Volume is conserved) as variations in density with depth in the ocean are just 2-3 % . These small variations can be ignored and thus $\rho_0(z)$ becomes ρ_0. With the same accuracy the reference pressure $p_c(z) \approx p_0(z)$ is linear with depth. One more approximation is used relating to the magnitude of density changes due to the equation of state. The relative contribution from changes in pressure does not exceed 2-3% so is removed. Giving the equations of motion in the Boussinesq approximation:

$$\rho_0 \frac{D\mathbf{u}}{Dt} = -2\rho_0 \mathbf{\Omega} \times \mathbf{u} - \nabla \tilde{p} - \tilde{p} \nabla \Phi + \mathcal{F}, \tag{1.3}$$

$$\nabla \cdot \mathbf{u} = 0, \tag{1.4}$$

$$\rho_0 \frac{D(\theta, S)}{Dt} = (\mathcal{G}_S, \mathcal{G}_\theta), \tag{1.5}$$

$$\tilde{\rho} = F(S, \theta, \rho_0) + F(S_0, \theta_0, \rho_0(z)), \tag{1.6}$$

where Eq. (1.4) is the Incompressibility equation in an adiabatic system. The symbols are defined in the list of symbols section in the glossary. The Boussinesq approximation is commonly used in large-scale oceanic circulation models such as the MITgcm.

Small Rossby number

The Rossby number is the ratio of inertial terms to Coriolis terms in the horizontal momentum equation.

$$R_o = \frac{U}{f_o L} << 1, \tag{1.7}$$

If we assume that the Rossby number (R_o) is small then Eq. (1.7) suggest that the Coriolis frequency (f) is important compared with inertial terms (advection terms) [2].

f-plane:

The β effect (variations in f with latitude) is small so that:

$$\frac{\beta L}{f} \leq R_o \tag{1.8}$$

Static Stability

Brunt Väisälä frequency (N^2) is a function of depth (z) only so

$$N^2(z) = \frac{\partial b}{\partial z} \tag{1.9}$$

where b is buoyancy.

Small Aspect Ratio and Hydrostatic Balance

Isopycnals have small slope as horizontal dimensions of ocean basins are much larger than vertical dimensions. This assumption gives small vertical motions and allows for terms to be neglected from the momentum budget.

$$\frac{\partial_x b}{\partial_z b} \,\&\, \frac{\partial_y b}{\partial_z b} \leq R_o. \tag{1.10}$$

[2] Must be modified near the equator and poles.

Only buoyancy terms can balance the pressure gradient and small aspect ratio flows are hydrostatically balanced:

$$\frac{\partial \psi}{\partial z} = \frac{b}{f_o}, \tag{1.11}$$

where ψ is a stream function. This leads to a neglect of all terms except pressure gradient and gravitation force in the vertical momentum equation (hydrostatic approximation). Many ocean models use the hydrostatic approximation.

Small Ekman Number:

The Ekman number is the ratio of frictional terms to coriolis terms in the horizontal momentum equation.

$$Ek \equiv \frac{\nu}{\Omega H^2} << 1, \tag{1.12}$$

Taylor (1922), where Ω is the angular velocity of planetary rotation, H is the ekman layer thicknes and ν is the kinematic viscosity. When the ratio of viscous forces to Coriolis forces is small then frictional forces are small the ekman layer is small and disturbances are able to propagate before decaying, meaning the surface boundary condition can be approximated to the frictionless geostrophic solution.

Quasi-Geostrophy

The Quasi-Geostophic (QG) approximation uses the above approximations and assumptions alongside the restriction that we consider density as a perturbation about a stratified background state QG assumptions imply there is no mean advection and no vertical component of eddy Potential Vorticity (PV) flux. This allows us to describe small perturbations of a stratified background state.

Writing the primitive equations in terms using the above approximations and assumption, the QG equations are written:

$$\underbrace{\frac{D}{DT}}_{\text{time derivative}} u_g - \beta y v_g - \underbrace{f_o v_a}_{\text{ageostrophic velocities}} = \underbrace{\mathcal{G}_x}_{\text{External forcing on momentum}}, \tag{1.13}$$

$$\frac{D}{DT} v_g - \beta y u - f_o u_a = \mathcal{G}_y, \tag{1.14}$$

$$\frac{\partial u_a}{\partial x} + \frac{\partial v_a}{\partial y} + \frac{\partial w_a}{\partial z} = 0, \tag{1.15}$$

$$\frac{D}{DT} b + N^2 w_a = \underbrace{\mathcal{B}}_{\text{nonconservativie buoyancy forces}} - \frac{\partial \overline{v_g' b'}}{\partial y}. \tag{1.16}$$

where $\frac{D}{DT}$ is the material derivative:

$$\frac{D}{DT} = \frac{\partial}{\partial t} + u\frac{\partial}{\partial x} + v\frac{\partial}{\partial y}. \tag{1.17}$$

and N^2 is the Brunt Väisälä frequency associated with the background state (denoted by a '$_b$'):

$$N^2(z) = g\left(\alpha\frac{\partial\theta_p}{\partial z} - \gamma\frac{\partial S_b}{\partial z}\right) \tag{1.18}$$

(Other symbols are defined in the list of symbols). The ageostrophic velocity is the difference between the actual velocity and the geostrophic one. The external forcing ($\mathcal{G}$) arises from wind, stress and friction etc. The non-conservative buoyancy forcing ($\mathcal{B}$) is from small scale mixing, and surface heat fluxes etc.

Deriving the QG equations is non trivial (*Pedlosky*, 1987) and lengthy so here we state the QG primitive equations, vorticity balance and Quasi-Geostophic Potential Vorticity (QGPV) to be used in residual mean theory. QG assumes small Rossby number so that when considering the absolute vorticity of a column of fluid is determined by vertical stretching rather than tilting of Taylor columns by thermal wind. A QG vorticity balance considers advection of relative and planetary vorticity, a stretching term and frictional forces:

$$\frac{D}{Dt}\left(\nabla_h^2\Psi + \beta y + \frac{\partial}{\partial z}\frac{f_0^2}{N^2}\right) = \text{curl}\mathcal{F} - f_0 g\frac{\partial}{\partial z}\frac{\mathcal{G}_p}{N^2}, \tag{1.19}$$

where Ψ is a streamfunction demeriting the entire flow at any give instant with the following relations[3]:

$$u = -\frac{\partial\Psi}{\partial y}, \tag{1.20}$$

$$v = \frac{\partial\Psi}{\partial x}, \tag{1.21}$$

$$w = -\frac{f_0}{N^2}\frac{D}{Dt}\frac{\partial\Psi}{\partial z} - \frac{g\mathcal{G}_p}{N^2}, \tag{1.22}$$

$$\rho = -\frac{f_0}{g}\frac{\partial\Psi}{\partial z}. \tag{1.23}$$

This vorticity balance describes properties of planetary waves, barotropic and baroclinic instabilities, geostrophic turbulence and mesoscale eddies.

The QG vorticity balance looks at a balance of potential vorticity:

$$Q_{qg} = \nabla_h^2\Psi + f + \frac{\partial\Psi}{\partial z}\frac{f_0^2}{N^2}. \tag{1.24}$$

[3]to zero order approximations except w which is first order

1.2.2 Eliassen-Palm Theorem

We now use the QG vorticity equations to examine eddy contributions to the time mean flow. Taking temporal and zonal means of Eq. (1.24) we get:

$$\overline{Q} = f + \frac{\partial^2 \overline{\Psi}}{\partial y^2} + \frac{\partial}{\partial z}\left(\frac{f^2}{N^2}\frac{\partial \overline{\psi}}{\partial z}\right). \tag{1.25}$$

If we define an eddy streamfunction as a deviation from a time mean streamfunction (Reynolds averaging):

$$\Psi' = \Psi - \overline{\Psi},$$

and then use $q' = q - \overline{q}$ (Eq. (1.24)-Eq. (1.25)) the eddy vorticity (q') can be described as:

$$q' = \frac{\partial^2 \psi'}{\partial y^2} + \frac{\partial^2 \psi'}{\partial x^2} + \frac{\partial}{\partial z}\left(\frac{f^2}{N^2}\frac{\partial \psi'}{\partial z}\right). \tag{1.26}$$

Using the streamfunction relations Eq. (1.20) - Eq. (1.23) the eddy PV flux can be described by:

$$\overline{v'q'} = \frac{\partial(-\overline{u'v'})}{\partial y} + \frac{\partial\left(\frac{f_o}{N^2}\right)(\overline{v'b'})}{\partial z}. \tag{1.27}$$

Eq. (1.27) is a relation between fluxes of eddy momentum, buoyancy and potential vorticity sometimes referred to as the Taylor identity (*Taylor*, 1914) This can be simplified defining the Eliassen-Palm flux $\mathbf{F}$ (*Andrews and McIntyre*, 1976)

$$\mathbf{F} = \begin{pmatrix} -\overline{u'v'} \\ \frac{f_o}{N^2}\overline{v'b'} \end{pmatrix}, \tag{1.28}$$

where the meridional component is the negative of the zonal eddy momentum and the vertical is proportional to the meridional eddy buoyancy flux allowing the eddy PV flux to be written simply as:

$$\overline{v'q'} = \nabla.\mathbf{F}. \tag{1.29}$$

1.2.3 Transformed Eulerian Mean Theory

Most of this theory is outlined in *Marshall and Radko* (2003) and (*Andrews and McIntyre*, 1976). Eddy buoyancy and momentum fluxes change the mean zonal state through the terms $\frac{\partial(\overline{v'b'})}{\partial y}$ and $\frac{\partial(\overline{u'v'})}{\partial y}$ in equations Eq. (1.16) and Eq. (1.13). Now considering the mean buoyancy budget in terms of an ageostrophic streamfunction Eq. (1.16)

$$\frac{D}{DT}b + \frac{\partial\overline{\psi_a}}{\partial y}N^2 = \mathcal{B} - \frac{\partial\overline{v'b'}}{\partial y}.$$

$$\frac{\partial\overline{b}}{\partial t} + \frac{\partial}{\partial y}\left(\overline{\psi_a}N^2 + \overline{v'b'}\right) = \overline{\mathcal{B}}. \tag{1.30}$$

Moving N^2 out of the brackets as it doesn't vary with latitude (static stability assumption where N^2 varies only with depth (z)):

$$\frac{\partial\overline{b}}{\partial t} + \frac{\partial}{\partial y}\left(\overline{\psi_a} + \frac{\overline{v'b'}}{N^2}\right)N^2 = \overline{\mathcal{B}}. \tag{1.31}$$

Here $\frac{\overline{v'b'}}{N^2}$ is the eddy flux term represented as a mean advection if we define ψ^* as the eddy induced mean stream function:

$$\psi^* = \frac{\overline{v'b'}}{N^2} \tag{1.32}$$

So using Eq. (1.32) we can write:

$$\frac{\partial\overline{b}}{\partial t} + \frac{\partial(\overline{\psi} + \psi^*)}{\partial y}N^2 = \overline{\mathcal{B}}. \tag{1.33}$$

The residual stream function is defined as a balance between eddy terms and ageostrophic motions:

$$\underbrace{\psi_{res}}_{\text{residual}} = \underbrace{\overline{\psi}}_{\text{ageostrophic}} + \underbrace{\psi^*}_{\text{eddy}} \tag{1.34}$$

This allows us to define a residual circulation:

$$(\overline{v_{res}}, \overline{w_{res}}) = \left(-\frac{\partial\psi_{res}}{\partial z}, \frac{\partial\psi_{res}}{\partial y}\right). \tag{1.35}$$

Ψ_{res} can be used as a new definition of a mean circulation, incorporating both eddy and ageostrophic terms. Substituting in Ψ_{res} into the mean buoyancy budget Eq. (1.33) we arrive at:

$$\frac{\partial\overline{b}}{\partial t} + \frac{\partial\psi_{res}}{\partial y}N^2 = \overline{\mathcal{B}}.$$

Which using Eq. (1.35) gives the transformed mean buoyancy budget as:

$$\frac{\partial\overline{b}}{\partial t} + \overline{w_{res}}N^2 = \overline{\mathcal{B}}. \tag{1.36}$$

Using this residual term we can also "transform" the other primitive equations to give:

$$\frac{\partial\overline{u}}{\partial t} - f_o\overline{v_{res}} = \overline{\mathcal{G}_x} + \underbrace{\overline{v'q'}}_{\nabla\cdot\mathbf{F}\text{ eddy forcing (EP flux)}}. \tag{1.37}$$

$$f_o \frac{\partial \overline{u}}{\partial z} = -\frac{\partial \overline{b}}{\partial y}. \tag{1.38}$$

$$\frac{\partial \overline{v_{res}}}{\partial y} + \frac{\partial \overline{w_{res}}}{\partial z} = 0. \tag{1.39}$$

This gives equations where the only explicit eddy terms arise from the term $\nabla \cdot \mathbf{F}$ in Eq. (1.37) representing the eddy forcing of the mean state.

Buoyancy Balances

The final aspect we wish to consider is a further examination on the buoyancy budget and the break down of eddy contributions. Starting with the mean buoyancy budget and following the method of (*Marshall and Radko*, 2003):

$$\overline{v}\frac{\partial \overline{b}}{\partial y} + \overline{w}\frac{\partial \overline{b}}{\partial z} + \underbrace{\frac{\partial \overline{v'b'}}{\partial y}}_{\text{EP flux}} + \frac{\partial \overline{w'b'}}{\partial z} = \underbrace{-\frac{\partial B}{\partial z}}_{\text{Buoyancy forcing due to air-sea interactions and small scale mixing}} \tag{1.40}$$

Assuming that $\overline{v'b'}$ is in the $\overline{b}$ surface (assume all the eddy fluxes are along isopycnals) so that $\nabla.\overline{v'b'}$ can be written as fluxes along isopycnals as advective transport $\mathbf{v}^*\nabla\overline{b}$:

$$\nabla.\overline{v'b'} = v'\frac{\partial \overline{b}}{\partial y} + w'\frac{\partial \overline{b}}{\partial z}. \tag{1.41}$$

Replacing $\overline{v}$ and $\overline{w}$ with:

$$\overline{w} = \frac{\partial \psi_{res}}{\partial y} - \frac{\partial \psi^*}{\partial y}$$

$$\overline{v} = -\frac{\partial \psi_{res}}{\partial z} + \frac{\partial \psi^*}{\partial z}$$

Then decomposing the eddy flux $(v'b', w'b')$ into along $\overline{b}$ components: $(\frac{\overline{w'b'}}{S_p}, \overline{w'b'})$ and horizontal components $(\overline{v'b'} - \frac{\overline{w'b'}}{S_p}, 0)$ where:

$$S_p = \frac{-\overline{b_y}}{\overline{b_z}}. \tag{1.42}$$

The buoyancy budget can be written in terms of a residual flux:

$$\left(\frac{-\partial \psi_{res}}{\partial z} + \frac{\partial \psi^*}{\partial z}\right)\frac{\partial \overline{b}}{\partial y} + \left(\frac{\partial \psi_{res}}{\partial y} - \frac{\partial \psi^*}{\partial y}\right)\frac{\partial \overline{b}}{\partial z} + \frac{\partial(\overline{v'b'} - \frac{\overline{w'b'}}{S_p})}{\partial y} + \frac{\partial(\frac{\overline{w'b'}}{S_p})}{\partial y} + \frac{\partial \overline{w'b'}}{\partial z} = \frac{\partial B}{\partial z}$$

Using definitions of ψ^* and Eq. (1.41) this condenses to:

$$\underbrace{\frac{\partial \psi_{res}}{\partial y}\frac{\partial \overline{b}}{\partial z} - \frac{\partial \psi_{res}}{\partial z}\frac{\partial \overline{b}}{\partial y}}_{\text{Jacobian } J(\psi_{res}, \overline{b})} = \frac{\partial B}{\partial z} - \frac{\partial(\overline{v'b'} - \frac{\overline{w'b'}}{S_p})}{\partial y}$$

If we define a parameter μ as:

$$\mu = (\frac{\overline{w'b'}}{\overline{v'b'}})(\frac{1}{S_p}),$$

where μ controls the magnitude of diapycnal eddy flux. We get:

$$J(\psi_{res}, \bar{b}) = \frac{\partial B}{\partial z} - \frac{\partial (1-\mu)\overline{v'b'}}{\partial y} \tag{1.43}$$

When $\mu = 1$ there are no diapycnal fluxes and the eddy flux is solely along $\bar{b}$ (adiabatic). The ocean interior is assumed to be closely adiabatic (*Karsten et al.*, 2002). Mostly these surface fluxes are taken to be negligible and the adiabatic components are assumed to be the significant components. In the surface layers $\overline{w'b'}$ tends to zero so that μ tends to zero, here diapycnal fluxes are important as eddy fluxes are across buoyancy surfaces giving a diabatic surface layer. In the surface In the limit of adiabatic eddies, vanishingly small mixing and air-sea buoyancy fluxes ($\mu = B = 0$) so that:

$$\psi^* = -\frac{\overline{w'b'}}{\bar{b}_y} = \frac{\overline{v'b'}}{\bar{b}_z} \tag{1.44}$$

to give:

$$\frac{\partial \psi_{res}}{\partial y}\frac{\partial \bar{b}}{\partial z} - \frac{\partial \psi_{res}}{\partial z}\frac{\partial \bar{b}}{\partial y} = 0 \tag{1.45}$$

So $\bar{b}$ is advected by ψ_{res}. Evaluating Eq. (1.43) at the base of the mixed layer *Marshall and Radko* (2003) devised a useful diagnostic. Assuming that $\frac{\partial b}{\partial z} = 0$ (vertical isopycnals) we can remove a term from the LHS:

$$\cancel{\frac{\partial \psi_{res}}{\partial z}\frac{\partial b}{\partial z}} - \frac{\partial \psi_{res}}{\partial z}\frac{\partial b_0}{\partial y} = \frac{\partial B}{\partial z} - (1-\mu)\frac{\partial}{\partial y}(\overline{v'b'}),$$

and integrate over the mixed layer to give:

$$\int_{-h_{ml}}^{0} -\frac{\partial \psi_{res}}{\partial z}\frac{\partial b_0}{\partial y}\mathrm{d}z = \int_{h_{ml}}^{0} \frac{\partial B}{\partial z} - (1-\mu)\frac{\partial}{\partial y}(\overline{v'b'})\mathrm{d}z.$$

Evaluating at the base of the mixed layer; ψ_{res} goes to zero at the surface. This allows us to write the LHS as the $\psi_{res}|_{z=0} - \psi_{res}|_{z=h_{ml}}$

$$0 - \psi_{res}|_{z=h_{ml}}\frac{\partial b_0}{\partial y} = B_0 - (1-\mu)\int_{h_{ml}}^{0}\frac{\partial}{\partial y}(\overline{v'b'})\mathrm{d}z$$

which is often condensed to:

$$\psi_{res}|_{z=h_{ml}}\frac{\partial b_0}{\partial y} = \underbrace{\tilde{B}_0}_{\text{net buoyancy supplied to the mixed layer by air-sea fluxes and lateral adiabatic eddy fluxes}} \tag{1.46}$$

This allows for a simple diagnostic tool: If $\tilde{B} > 0$ (Buoyancy gain (heating)) then $\frac{\partial b_0}{\partial y} > 0$ so $\psi_{res}|_{z=h_{ml}} > 0$. Relating surface buoyancy gain/loss to the sign of the SO ROC. Often we see this buoyancy gain/loss to be taken as simply the surface heat fluxes where the diabatic eddy contribution is assumed to be negligible.

1.3 Motivation

The resolution of current climate models is restricted by computational limitations. A typical lateral resolution of coupled climate models is 1° , thus, the complex interaction of eddy processes in the SO are not be fully captured in those models. Hence they require parameterisation of eddies, however the debate is still open as to whether eddy parametrisations should be purely adiabatic or have additional diapycnal mixing terms (*Gent*, 2011). Currently these parameterisation schemes do not represent diabatic eddy fluxes well, which could lead to missing feedbacks in global climate models. It is of great interest to understand what possible feedbacks are being neglected in climate models and what the physical processes behind them are, thus we use idealised models to gain a better understanding of processes that are important when we consider the future response of the SO.

Marshall and Radko (2003) showed that in most realistic cases the diabatic eddy contribution is generally small compared to the surface forcing and that the SO ROC can be predicted from the surface forcing using Eq. (1.46). Many studies, however, show an inter-hemispheric connection via the Atlantic meridional overturning circulation (AMOC) and North Atlantic Deep Water (NADW) formation, which acts as a control on the SO ROC (e.g. *Wolfe and Cessi* (2009), *Nikurashin and Vallis* (2012), and from the *Marshall and Radko* (2003) schematic Fig. 1.3). This suggests that the inter-hemispheric control on the SO ROC, occurs via changes in the budget of Eq. (1.43). When investigating the SO ROC in a channel model the rest of the world's ocean must be represented via a northern boundary condition, i.e. the stratification north of the channel, impacting the isopycnal slope in the interior of the channel. We wish to investigate the effects of that northern boundary condition on setting the SO ROC in a channel model and dynamics set by the northern boundary.

Within the *Marshall and Radko* (2003) framework we can see that the SO is not disconnected from the rest of the world's oceans, and must rely on outside diabatic processes to close the SO ROC see Fig. 1.3. We wish to investigate in a very idealised, theoretical, way the possible mechanisms and controls on the SO ROC. This will allow us to illuminate possible considerations that may be overlooked

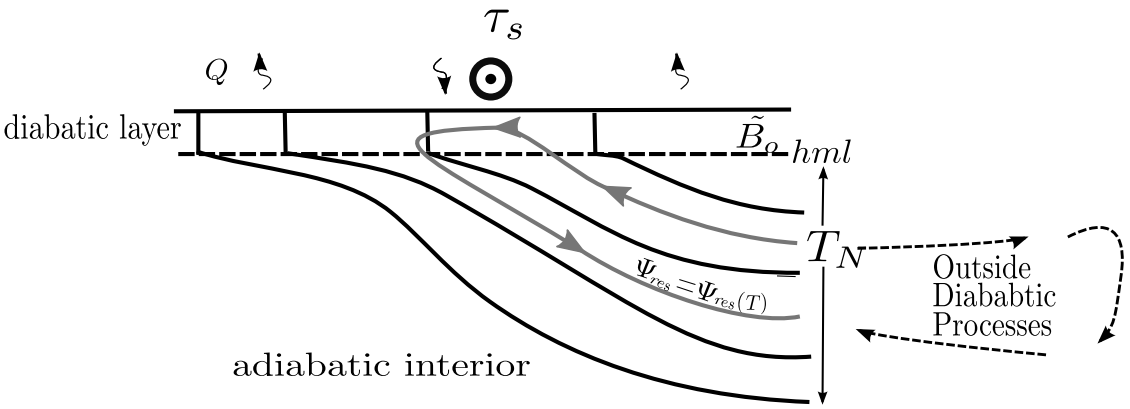

Figure 1.3: Southern Ocean Overturning Circulation directed along isopycnals related to surface forcing and outside diabatic processes. Adapted from figure 3 in *Marshall and Radko* (2003).

when setting up channel models and glimpse possible interactions with boundary conditions that may have been previously unconsidered.

1.4 Outline of Model

1.4.1 MITgcm Overview

The model code used is the Massachusetts Institute of Technology general circulation model (MITgcm) (*Marshall*, 1997). The MITgcm is a finite volume primitive equation model solving the incompressible Navier-Stokes equations. Assuming the flow is incompressible:

$$D_t\rho << \rho\nabla\cdot\mathbf{v}, \tag{1.47}$$

to filter the acoustic modes. Density perturbations are assumed to be smaller compared to the reference density:

$$\rho' = (\rho - \rho_0) << \rho_0. \tag{1.48}$$

This allows the use of the Boussinesq approximation to make the momentum equations linear. Therefore, the incompressible Boussinesq equations are:

$$\begin{aligned} \rho_0 D_t\mathbf{v} + 2\Omega\times\rho_0\mathbf{v} + g\rho\hat{\mathbf{k}} + \nabla\rho &= \mathbf{F} \\ \rho_0\nabla\cdot\mathbf{v} &= 0 \\ \partial_t\eta + \nabla\cdot(H+\eta)\mathbf{v} &= P - E \\ D_t\theta &= Q_\theta \\ D_t s &= Q_s \\ \rho &= \rho(s,\theta,p) \end{aligned} \tag{1.49}$$

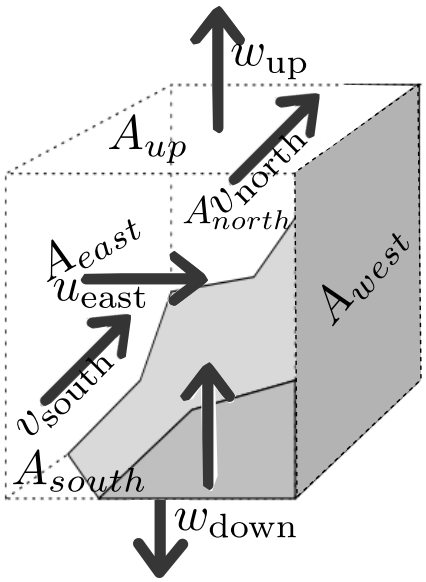

Figure 1.4: Schematic of model cell, faces are labelled with an A flow through faces are labelled with their corresponding velocity component.

where $\mathbf{v}$ is velocity, p is pressure ρ is density, η is the displacement of free surface from resting sea-level, θ is potential temperature, s is salinity, ρ_0 is the reference density, g is gravitational acceleration, H is bottom depth (*Adcroft et al.*, 2004). The hydrostatic approximation is also be made for horizontal resolutions coarser than 1 km (*Adcroft et al.*, 2004). Many of these approximations were discussed and used in section 1.2.3. The model is then discretized using finite volume methodology (*Adcroft et al.*, 1997), where the governing equations are integrated over finite volumes and applying the Gauss-divergence theorem to give a continuity in the form:

$$A^u_{east}u_{east} - A^u_{west}u_{west} + A^v_{north}v_{north} - A^v_{south}v_{south} + A^w_{up}w_{up} - A^w_{down}w_{down} = 0, \tag{1.50}$$

written in terms of the normal flow (u, v, w) across cell faces $A_{\text{direction}}$. With no normal flow at rigid boundaries (volume flux though a rigid boundary is set to zero) (see Fig. 1.4). The components of velocity are staggered on an Arakawa C grid (*Chang et al.*, 1977) in the horizontal and a Lorenz grid in the vertical (*Lorenz*, 1960) - see Fig. 1.5.

The model then discretizes the momentum equations between time levels and substitutes then into the discrete continuity equation to obtain an elliptic equation for pressure, refer to *Marshall* (1997) for detailed explanation of Algorithms used in the MITgcm. Specific choices for the model set up are outlined in the next section and in appendix A. Information referring to finite volume advection is discussed in appendix C. In the following section we outline the parameters and boundary

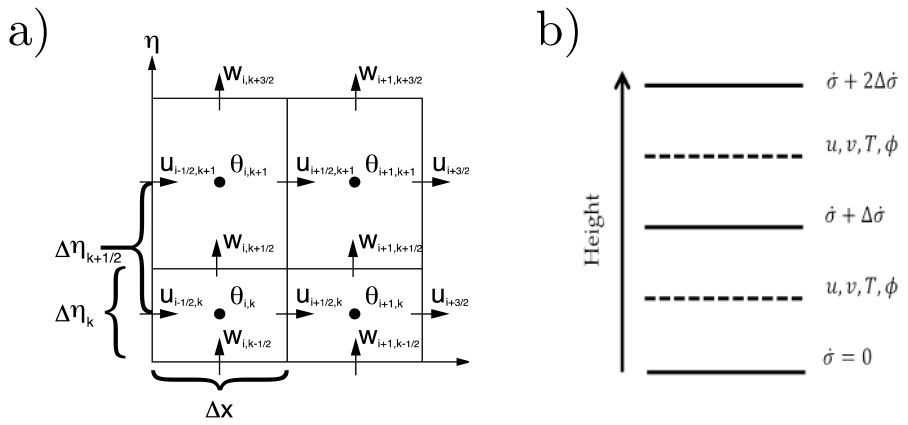

Figure 1.5: A illustration of the horizontal and vertical grid spacing. a) Arakawa C grid and b) Lorenz vertical grid. *Adapted from* (*Collins et al.*, 2013)

conditions applied to set up the MITgcm for our purpose.

1.4.2 Considering Model Set Up

First we have to consider the best approach to modelling this problem within temporal and computational limits. It is not feasible to run a high resolution eddy resolving coupled climate model altering NADW formations and analysing the SO ROC and diabatic eddy response. This would also be too complex to fully understand the important factors controlling the diabatic eddy response and the underlying physics. In order to reduce computational costs, we can run an idealised channel model with periodic flow, applying boundary conditions to mimic the processes outside of the Southern Ocean. We then have to apply surface and bottom boundary conditions and forcing to generate the appropriate flow and circulation. A simple box ocean can then be used to run a high resolution simulation to enable us to examine the basic physics controlling Southern Ocean diabatic eddies.

Here we outline the rationale for the most basic parameters, before going on to give a full overview of the generalised set up that all the simulations will be based on.

Fundamental Parameters

A few fundamental parameters must decided to establish a trade off between computational cost, most appropriate physics and ease of analysis to test the basic theory. In order to gain a better understanding we require a model setup that can be run many times with altered boundary conditions.

Domain size:

Domain size is minimised for computational efficiency, we choose a narrow channel to mimick drake's passage. The meridional length is set by the boundary conditions; it must be long enough to allow for space to include a northern boundary condition that allows for an overturning to be maintained and it must be long enough for heat and wind forcing to have sensible gradients so we have set the meridional length to 2000km. The zonal length can be very short in the In absence of topography as the channel set up will be a zonally re-entrant; 1000 km will suffice. If topography is included standing eddies will form and a much longer channel will be required to account for meanders in the ACC. Depth can be set quite shallow in the absence of topography, we use 3000km, however when topography is included we increase the depth to 4000km to allow for flow over topography.

Resolution:

Once again a trade off with computational efficiency is considered to decide on horizontal resolution. Higher resolution both increases the number of grid points and requires shorter time steps to satisfy the CFL condition (discussed separately later) therefore increases in resolution rapidly increasing computational cost. For the purpose of investigating eddy dynamics the coarsest resolution that is acceptable will be "just about" eddy resolving. The Rossby radius of deformation (L_d) is calculated by:

$$L_d = \frac{NH}{f}, \tag{1.51}$$

where N is the buoyancy frequency typically 3 x 10^{-3} s^{-1}, H is thickness scale (typically 1000 m) and f is the Coriolis parameter (1 x 10^{-4} s^{-1}-1.3 x 10^{-4} s^{-1}). Using those typical values we can estimate the Rossby radius 10-30 km. To resolve for eddies a minimum of 2 grid spacing per radius is required, therefore we can use 5km as our horizontal resolution.

Diffusion:

To achieve an approximately adiabatic interior the Laplacian diffusion of heat is set to zero both horizontally and vertically.

Equation of state:

For simple idealised models a linear Equation of State (EOS) can be used to establish qualitative results ideal for starting to understand a poorly understood mechanism. In more complex models this would not suffice.

Time Stepping:

Adam-Bashforth staggered baroclinic time setting is used rather than synchronous so allow for the most recent velocities to be used in order to compute the advection terms.Set to 450s, depending on resolution to satisfy the Courant Friedrich Lewy (CFL) condition.

Other run time parameters are outlined in appendix B, where we include an example data file. Next, with these constraints in mind, the next most fundamental aspects of the model set up are the boundary conditions applied.

Northern Boundary Conditions

In order to begin to understand how the diabatic eddies might respond to an altered northern boundary condition. We must decide how to represent the rest of the World Oceans in the model, as the SO is not disconnected from the rest of the world and the SO ROC requires diabatic processes to the north of the ACC in order to close. To this end we considered 3 ways of dealing with the outside of the SO:

1. Another additional basin representing the northern hemisphere
2. Enhanced vertical diffusion
3. A sponge layer

1. Similar to *Saenz et al.* (2012), which to be run at a high enough resolution would be far to computationally expensive, when considering the number of model runs to be performed. The *Saenz et al.* (2012) model was run at a resolution of $1/4^\circ$ and at least $1/12^\circ$ would be required to investigate the eddy dynamics in the SO. These factors ruled out the additional basin method.
2. With no heat flux through the northern boundary a shallow thermocline will be generated. Therefore, excess vertical diffusion can be applied near the northern edge of the domain to increase the thermocline depth, north of the most northernmost front. Enhanced diffusion in the north of the domain represents the over-

turning circulation, wind-driven circulation and vertical mixing acting throughout the global ocean. Changes in stratification due to variations in surface buoyancy are felt very quickly compared with slow (millennia) equilibration times in the real ocean *Allison et al.* (2010). Preliminary experiments using enhanced vertical diffusion, following variations of the model set up used in *Hogg* (2010), were unsuccessful in generating a sensible overturning (*not shown here*). The average EKE of these tests were too low and generated little eddy compensation (overturning was not the focus of the *Hogg* (2010) experiments). Therefore, enhanced diffusion is not suitable for investigating changes in the SO ROC and diabatic eddies.
3. Sponge layer models where temperature/density is relaxed to a prescribed profile have shown promising results in a number of other studies (*Abernathey et al.*, 2011; *Abernathey and Cessi*, 2014; *Zhai and Munday*, 2014). Preliminary experiments using a sponge layer to relax to a set temperature profile as in *Abernathey et al.* (2011) were able to generate a sensible SO ROC by mimicking diabatic processes outside the Southern Ocean. [4]

Preliminary experiments helped us to establish the most appropriate northern boundary condition as a sponge layer relaxing to a set temperature profile, which are outline later in detail in section 1.5.

Surface Boundary Conditions

For the surface boundary condition a number of aspects must be taken into consideration. The first step is to deicide on the model configuration; atmosphere-ocean or ocean only. To reduce complexity and computational cost we chose an ocean only model noting that coupling to an atmosphere would perhaps be a very interesting addition for future work. With an ocean only model the atmospheric fluxes and forcing must be prescribed, for a set up with a linear equation of state in temperature we need only consider mechanical and thermal forcing.

Heat forcing

Buoyancy forcing in the absence of an atmosphere for heat exchange can be achieved via a number of methods in the MITgcm. As we are using an equation of state linear in temperature only, we only consider buoyancy forcing from heat forcing and not from evaporation and precipitation/ freshwater forcing. The simplest buoyancy forcing would be a fixed surface heat flux Q (W/m^2) varying only in x and/or y.

[4] NB: A very small amount of random noise: $O10^{-5}$ must be added to the temperature layers to prevent laminar flow (*Abernathey Pers coms*)

Time varying heat fluxes to generate seasonal cycles is not appropriate in such an idealised set up. Another method is surface restoring where temperature/density is restored to a set profile in the uppermost layer. The initial set up will be using fixed surface heat fluxes, discussed in section 1.5. Buoyancy forcing will be discussed in much greater detail in chapter 3.

Wind forcing

Wind forcing can be applied in a zonal and/or meridional direction. Again we have chosen to apply a fixed surface wind stress rather than time varying due the idealised nature of our model and for ease of interpretation. We use a fixed zonal wind stress in order to generate an ACC to be described in section 1.5.

Free surface

The MITgcm allows a free surface or rigid lid surface boundary condition, the only additional complication with a free surface boundary condition is the additional requirement of a free surface correction in vertically integrated tracer budgets[5]. The upper surface of the ocean is a free surface which is driven by the divergence of volume flux in the interior. We chose a linear free-surface which permits surface gravity waves with finite phase speed and introduces a Helmholtz term in the surface pressure equation. This is a very good approximation for deep water where $\eta << H$ (*Campin et al.*, 2004) such as in our channel model setup. Using a non-linear free surface has many additional complications and extra computational cost with no benefits, so is not considered appropriate here.

Bottom Boundary Conditions

As the southern boundary will be a fixed wall and the zonal boundaries will be periodic. The last set of boundary conditions to be applied are those at the bottom of the domain.

1. Slip
2. Topography
3. Linear drag

1. The sides and bottom of the model must have a boundary condition defining

[5]On calculation this is very small and can be neglected. This correction term is outlined later in budget analysis when applied in the relevant chapters.

the flow at these boundaries. Usually this is either no slip or free slip. As the computational cost is not severely constrained, we use a no slip boundary condition which maintains zero flow at the boundary by adding in an additional source term in the cells next to the boundary.

2. The Southern Ocean has a continental shelf that helps maintain deep water formation and ridges that slow the zonal flow and enhance eddy activity. Topography steers the ACC flow and generates standing eddies (steady-state meanders). The importance of these standing eddies is a topic sparking a lot of interest. If zonal means are used in the decomposition then it would appear the standing eddy component dominates in both idealised and realistic eddy-permitting models *Tréguier et al.* (2007). However observational studies e.g. *Britain et al.* (1981) suggest that there is no mean flow heat flux across depth averaged contours of temperature, this is only achieved by transient eddies suggesting the large scale dynamics in flat bottom models closely resemble the stream wise averaged models with topography. This would suggest the approach of stream-wise averaging should be used instead of zonal averaging in models with topography, but this a more complex framework to use so was often neglected in earlier studies: (*Hallberg and Gnanadesikan*, 2006; *Farneti and Delworth*, 2010) leading to different results on the importance of standing eddies and whether they alter the stratification of the ACC, or just the path (*Abernathey et al.*, 2013). Studies that have investigated the effect of topography using a stream-wise framework (*Viebahn and Eden*, 2012) and (*Abernathey et al.*, 2013), investigating heat fluxes across the ACC, suggest the standing eddy component is not negligible and qualitatively effects the generation and distribution of transient eddies. For initial runs we use a flat bottom to reduce computational cost, as little zonal variation arises in the ACC. It should be noted that some topography runs must be used to validate the flat bottom runs and the possible missing effects must be considered. We also note the lowermost overturning cell in our experiments with flat bottoms should not be interpreted as meaningful.

3. In the absence of topography, Hidaka's Dilemma must be considered (*Hidaka and Tsuchiya*, 1953). For a flat bottom scenario with zero bottom friction, zonal transport would scale only with viscosity, channel width and wind stress would generate an unrealistically large ACC. *Hidaka and Tsuchiya* (1953) showed the only way to generate a sensible sized ACC was either to alter viscosity or diffusivity to unreasonable values, or they found that this can be mitigated by a no-slip boundary condition and a linear bottom drag, which is the approach we use.

Advection Schemes

There are many options for advection schemes in the MITgcm for a variety of setups. These vary in computational cost and spurious numerical mixing (*Ilcak et al.*, 2012; *Hill et al.*, 2012). In preliminary experiments we investigated the most appropriate advection scheme. In general there are some schemes more appropriate for high resolution than for coarse resolution set ups and vice versa, with a higher order scheme being more appropriate for higher resolution. For propagating fronts, a flux limiting scheme must be employed. When the time step is limited by advection, then multi-dimensional non-linear schemes offer the most stability, however they reduce the ability to calculate accurately diffusion/dissipation. We investigated schemes 33; as in *Hogg* (2010), 81 as in *Abernathey et al.* (2011) and advection scheme 7 as used in *Zhai and Munday* (2014).

Advection scheme 33: A third order direct space time flux corrected scheme, for 5 km resolution this produced a slightly noisy tracer field and is perhaps not of high enough order for the increased resolution required in our experiments (twice the resolution used in *Hogg* (2010)). This scheme was considered when running the preliminary experiments to establish the most suitable northern boundary condition, as *Hogg* (2010) formed the basis of our enhanced diffusion experiments, the scheme was later checked in the sponge layer experiments as well.

Advection scheme 81: A Second order moment scheme based on *Prather* (1986). Has a significant increase (20%) in computational cost. This scheme is favoured in

many studies of the Southern Ocean such as (*Abernathey et al.*, 2011; *Abernathey and Cessi*, 2014; *Wolfe*, 2014) after *Hill et al.* (2012) and showed a reduction in spurious diapycnal mixing.

Advection scheme 7: Seventh-order one-step method with monotonicity-preserving limiter OS7MP, *Daru and Tenaud* (2004) with modifications from Adcroft and Campin, (*MITgcm support mailing list communications 2010*), in many cases compares adequately with the more computationally expensive scheme 81 *Ilcak et al.* (2012).

With diffusion set to zero in the interior and at high resolution the effects of spurious diapycnal mixing between OSMP7 and a Prather advection scheme are negligible for this study. Preliminary experiments not shown here showed no noticeable difference other than computational cost between advection scheme 7 and 81, motivating us to use scheme 7.

Mixing Parameterisation

Some sub grid mixing must be included in order to maintain a stable mixed layer. In the MITgcm this can be achieved through a number of methods of varying complexity: Turbulent Kinetic Energy (TKE), K-profile parameterization (KPP) and convective adjustment. Many models employ the widely used KPP mixing scheme (*Large et al.*, 1994), which greatly enhances vertical diffusion in the upper 50 m as well as introducing a non-local transport term to represent convective transport, as all other convection parametrisations must be disabled in the model. KPP requires additional terms to be introduced into buoyancy budgets, in order to estimate the diffusion term as well as careful and considered adjustment to ensure a sensible mixing. Convective adjustment (*Cox and Bryan*, 1984) is the most basic method of maintaining a stable mixed layer as it simply restratifies statically unstable density configurations. Convective adjustment is simpler to analyse than using KPP and requires little consideration on overall impact on the

physics of the model. It can only be used in idealised models with reasonably coarse vertical resolution otherwise the computational cost of the iterative method of stabilisation would be too high and the mixing not sufficient. Studies comparing convective adjustment and KPP, such as *Boccaletti et al.* (2007), show only slight differences in EKE, which is the same order of magnitude for both, suggesting convective adjustment is adequate for the physics of an idealised model and offers the advantage of simplicity. Although convective adjustment is a sensible choice for a highly idealised model, with finer vertical resolution or in a less idealised case such as the inclusion of topography, this method may not be suitable as evaluated in *Griffies et al.* (2000). The turbulent kinetic energy (TKE) scheme, described in *Gaspar et al.* (1990); *Madec and Delecluse* (1998), is another method, favoured in runs such as the NEMO ORCA models (*Kazantsev*, 2013). TKE requires no explicit convective scheme so allows for a more flexible model set up, offering an alternative to KPP where convective adjustment alone will not suffice. Given these considerations, for our starting model set up with a flat bottom we use the least complex mixing parameterisation: convective adjustment.

1.5 Channel Model Set Up

Here we outline the basic model set up for a flat bottom channel to test the initial effects of closing the northern boundary. All subsequent models will be variants of the model outlined here and the specifics described in detail in the relevant chapters. An example python script generating the model grid and forcing is given in appendix A. The initial channel domain is 1000 km by 2000 km and 2985 m deep with a horizontal resolution of 5 km with 30 geopotential layers ranging in thickness from 10m at the surface to 250 m at the bottom. To allow for a small domain size and reduced computational cost the channel was setup with no topography as rationalised in *Abernathey et al.* (2011) (see section 1.4.2).

The model was forced using similar zonal wind stress sine bell curve, to *Abernathey et al.* (2011) to generate an appropriate zonal flow.

$$\tau_s(y) = \tau_0 sin(\frac{\pi y}{L_y}), \tag{1.52}$$

where L_y is the meridional width, $Q_0 = 10$ W m^{-2} and $\tau_0 = 0.2$ N m^{-2}. The magnitude of τ_0 roughly approximates the observed surface wind stress *Large and Yeager* (2009). We also employed a similar heat forcing to *Abernathey et al.* (2011)

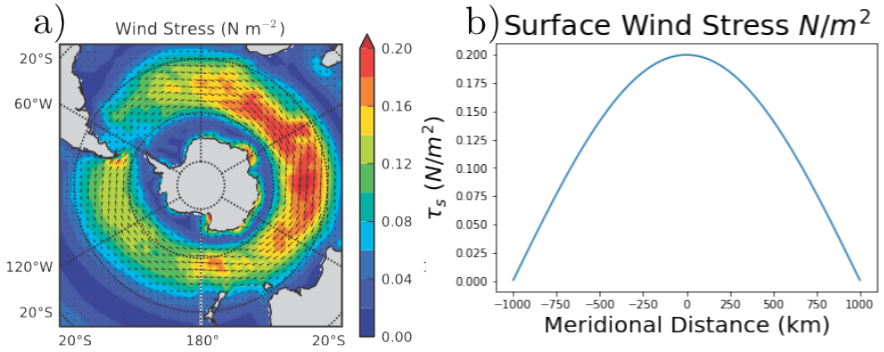

Figure 1.6: a) Taken from *Abernathey et al.* (2011) the net surface wind from CORE 2 (*Large and Yeager*, 2009). b) A simplified version of the observed surface wind stress used in our model.

(fixed surface flux). However, as the northern boundary is fully closed, the surface heat flux has to be adjusted so that there is no net cooling at the surface:

$$Q(y) = \begin{cases} -Q_0\, cos(\frac{18\pi y}{5Ly}) & \text{for } y \leq \frac{5Ly}{36} \text{ and } \frac{22Ly}{36} \geq y \geq \frac{30Ly}{36}, \\ -Q_0\, cos(\frac{18\pi y}{5Ly} - \frac{\pi}{2}) & \text{for } \frac{5Ly}{36} \geq y \geq \frac{20Ly}{36}, \\ 0 & \text{for } y \geq \frac{5Ly}{6}. \end{cases} \tag{1.53}$$

Surface buoyancy forcing in the Southern Ocean is poorly constrained, (*Cerovečki et al.*, 2011) so the buoyancy forcing applied is a simplification of the buoyancy loss/gains associated with AABW , NADW and AAIW, roughly matching the CORE2 estimates from *Large and Yeager* (2009) Fig. 1.7.

Previous idealised channel models such as *Cerovečki et al.* (2009); *Cessi et al.* (2006) tried to model the Southern Ocean without representation of the rest of

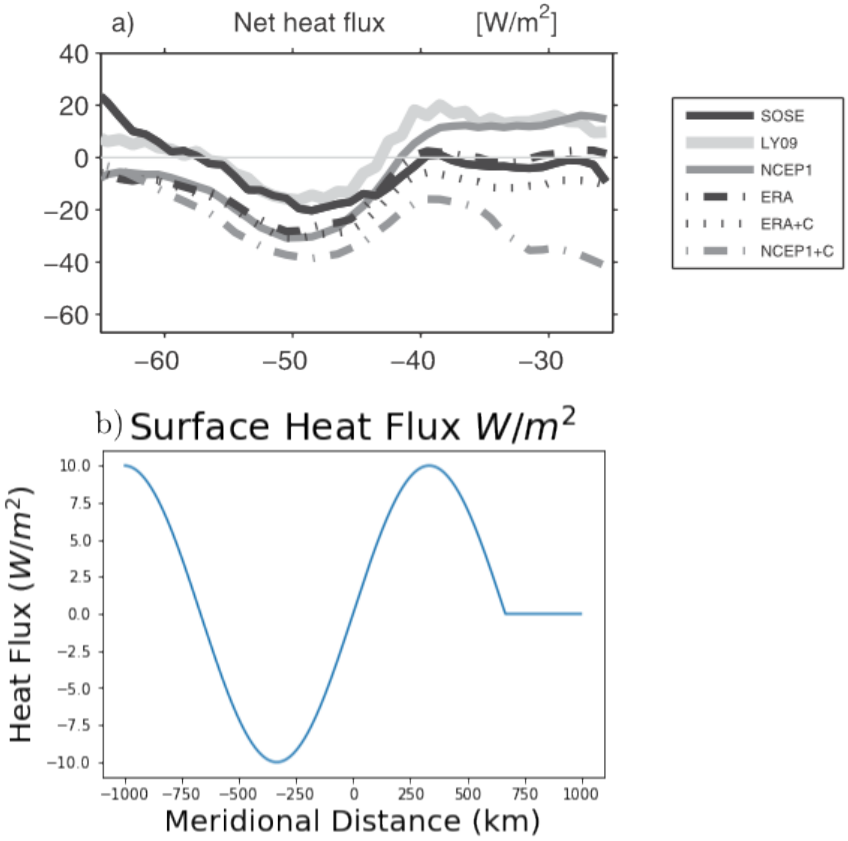

Figure 1.7: a) Taken from *Cerovečki et al.* (2011) the net surface heat flux from various estimates b) A simplified version of the LY09 line (*Large and Yeager*, 2009) to force our model in a simple cooling, heating, cooling pattern.

the global basins, which leads to a vanishingly small deep residual overturning circulation. *Abernathey et al.* (2011) used a sponge layer to relax the northern boundary temperature (T) profile to a prescribed temperature profile:

$$T^*(z) = \Delta T \frac{(e^{z/N_d} - e^{-H/N_d})}{1 - e^{-H/N_d}}, \tag{1.54}$$

assuming a natural stratification $N_d = 1000$ m and a temperature difference (ΔT) of 8°C. This exponential is taken from *Abernathey et al.* (2011) based on modelling and observational studies (*Karsten et al.*, 2002; *Wolfe et al.*, 2008). This allows a return pathway for deep overturning that requires crossing of isopycnals to exist and is computationally inexpensive, allowing a small domain eddy resolving set up. The sponge is set using a mask (M_{rbcs}) of values between 0 and 1 (0 = no relaxation, 1 = relaxing rate ($\frac{1}{\tau_R}$) where τ_R is the relaxation time scale in seconds).

The tendency of temperature at each grid point is modified to:

$$\frac{\mathrm{d}T}{\mathrm{d}t} = \frac{\mathrm{d}T}{\mathrm{d}t} - \frac{M_{rbcs}}{\tau_R}(T - T^*). \tag{1.55}$$

With the mask decaying from 1 to 0 in the northern 100 km domain from North to South in a parabolic decay function.

This is the basis for our channel model configurations. The first stage of our investigation is to understand what physical processes are altered when the northern boundary is closed and whether this is a step function response or a smooth transition. As this model is highly idealised, we use the results as a qualitative guide to provide insight on how to quantitatively and more definitively investigate this in the future.

Chapter 2

Diabatic Eddies Setting Buoyancy Forcing

This chapter focuses on the SO ROC response to closing the northern boundary condition in a highly idealised setting to understand the most basic fundamentals of this process and establish if in fact the SO ROC vanishes with a closed northern boundary.

2.1 Introduction

Changes to the Southern Ocean Residual Overturning Circulation (SO ROC) could have large effects on ocean circulation and climate, making it of great interest to understand what sets the strength and sense of the SO ROC. The upper cell of the SO ROC is closed outside the Southern Ocean; connecting the surface branch with the deep branch (Fig. 2.1).

We look at this within a modelling context where a northern boundary condition must be applied in order to close the SO ROC. In the framework of *Marshall and Radko* (2003) the SO ROC can be related to the effective buoyancy forcing in the

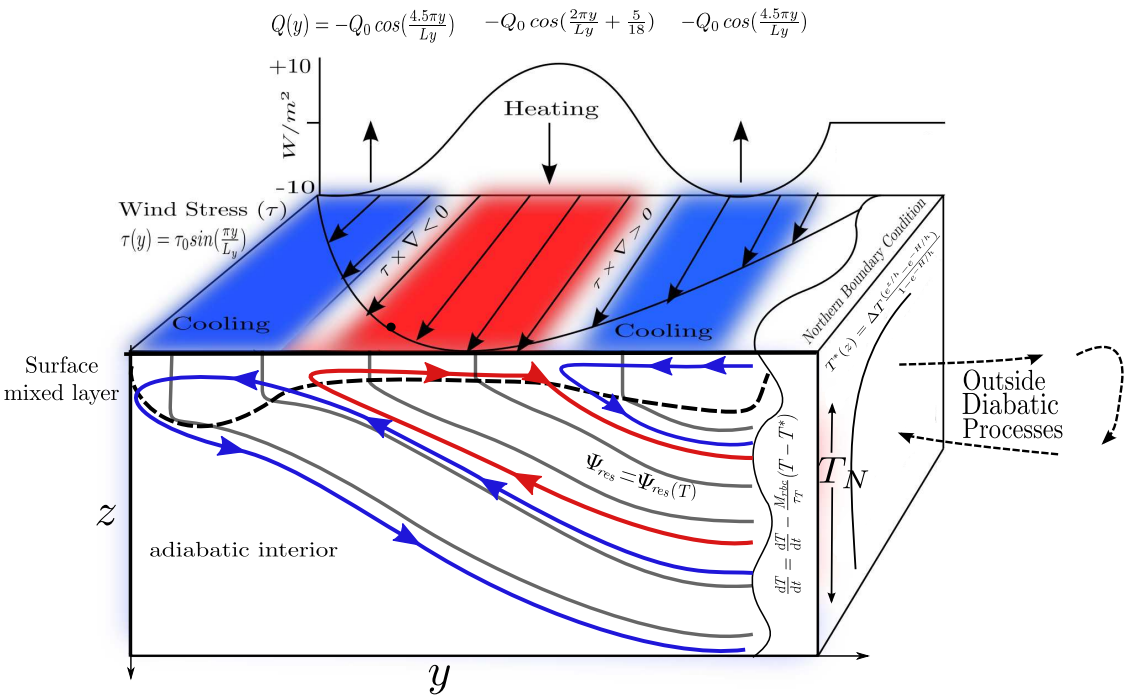

Figure 2.1: An illustration of the channel model configuration, showing the surface forcing and the sponge layer at the northern boundary, with the expected residual circulation from the surface forcing at short sponge relaxation time scales depicted. The SO ROC in coloured arrows is determined in the surface mixed layer, which in this configuration can be several hundred meters deep, and directed along mean isopycnals in the interior.

Southern Ocean channel. However, without an open boundary the SO ROC cannot be maintained, implying that the effective buoyancy forcing in the Southern Ocean must go to zero. This part of the SO ROC circulation must be represented when considering the SO in isolation; *Marshall and Radko* (2003) argued that in the present climate the effective surface buoyancy forcing in the Southern Ocean is dominated by surface buoyancy exchange between ocean and atmosphere. In a set-up of fixed surface fluxes and no diapycnal mixing (consistent with the adiabatic pole-to-pole circulation), either convective mixing, or diabatic eddy fluxes must increase to cancel the surface fluxes and alter the effective buoyancy forcing. This suggests the choice of northern boundary condition may have a large impact on the dynamics of the model impacting the outcome of any theory investigated.

Here we start in a very idealised theoretical framework considering the closure of the northern boundary. This is used as the initial starting point in our investigation before proposing other factors to investigate. Our first line of investigation is to establish if indeed the SO ROC ceases to exist when we close the northern boundary without altering the surface forcing and if that change is a step change or a smooth transition.

2.2 Theory

We investigate the overturning adjustments associated with changes in diabatic processes outside the Southern Ocean by considering an idealised channel model in which diabatic processes further north are represented through a diabatic sponge layer at the northern side of the channel. The diabatic forcing of the sponge layer is decreased by increasing the specified relaxation time scale in which the stratification is restored to a prescribed profile. When the northern boundary condition is changed, we expect a response in the diabatic eddy fluxes, adjusting the net diabatic forcing in the surface mixed-layer to accommodate the change in

diabatic forcing, and as a result in stratification, at the northern boundary. Also, because the unchanged winds will leave the Eulerian MOC unaffected, a change in the SO ROC must be accommodated by a change in the eddy-driven overturning. So, the change in eddy-driven overturning must be associated and consistent with a change in net buoyancy forcing in the diabatic mixed-layer. Here, we focus on how the time-mean heat budget is affected. To simplify the analysis we consider a model setup with a linear equation of state, equating buoyancy to temperature. Starting from the time mean heat budget we write:

$$\nabla \cdot \overline{\mathbf{u}T} = -\frac{\partial Q/C_p\rho_0}{\partial z}, \tag{2.1}$$

where Q is the heat flux supplied to the surface through air-sea fluxes and other diabatic processes like diapycnal mixing and convective overturning.

Starting from this time mean heat budget *Marshall and Radko* (2003) created a widely used diagnostic by decomposing the eddy fluxes into adiabatic and diabatic components and removing the diabatic eddy fluxes from the L.H.S of Eq. 2.1 to the RHS. The background theory for this is described this in detail in section 1.2.3 where we arrive at Eq. (1.43). Evaluated at the base of the mixed layer, below which the SO ROC is constant along mean isopycnals, the SO ROC is related to the diabatic forcing over the mixed layer. Putting Eq. (1.43) from *Marshall and Radko* (2003) in terms of temperature alone, as per our model's equation of state, gives:

$$-\Psi_{res}|_{hml}\frac{\partial T}{\partial y} = Q - \int_{hml}^{0} \frac{\partial\left(\overline{v'T'} - \frac{\overline{w'T'}}{S_T}\right)}{\partial y}\mathrm{d}z, \tag{2.2}$$

where Ψ_{res} is the SO ROC and $S_T = -\overline{T_y}/\overline{T_z}$ is the slope of mean temperature surfaces. *Marshall and Radko* (2003) showed that in most realistic cases the diabatic eddy contribution and other diabatic forcing terms are small compared with the surface forcing and that the SO ROC can be predicted from $Q = Q_{surflux}$,

neglecting diapycnal mixing and convective overturning. As our motivation for this study is the idea of far field forcing altering the SO ROC we look to the role of northern boundary conditions in channel models. For a different stratification north of the ACC, the diabatic eddy component may become as important as the surface buoyancy forcing term, or deeper convective mixing in the SO channel must come into play. This could mean when setting up a channel model to evaluate the SO ROC response to altered surface forcing the fundamental dynamics may have been determined by the boundary condition applied to maintain a 3 cell SO ROC.

In some scenarios the diabatic eddy contribution to the heat budget may not be negligible and must be considered. To do this Eq. 2.2 must be reformulated to become compatible with the model equations. Part of this reformulation is due to the model's discretization, but another part is more fundamental. When deriving Eq. (2.2) the QG stream function is represented by Eq. (1.32) which means the left-hand side of Eq. (2.2) is appropriate for the base of the mixed layer and below, in the surface mixed layer a simple eddy stream function cannot be defined (*Plumb and Ferrari*, 2005). This makes evaluating the residual mean heat budget more complicated than would first appear. If we keep in a Cartesian framework and start from Eq. 2.1 and making a Reynolds decomposition the budget is split into eddy and mean transport terms:

$$\frac{\partial \overline{v}\overline{T}}{\partial y} + \frac{\partial \overline{w}\overline{T}}{\partial z} + \frac{\partial \overline{v'T'}}{\partial y} + \frac{\partial \overline{w'T'}}{\partial z} = \frac{\partial \overline{Q}}{\partial z}. \tag{2.3}$$

Traditionally the eddy fluxes are decomposed into an along $\overline{T}$ component and a remaining horizontal component (*Marshall and Radko*, 2003). Here we decompose the transport terms into an along $\overline{T}$ component and a remaining vertical component:

$$\left(\overline{v'T'}, \overline{w'T'}\right) = \underbrace{\left(\overline{v'T'}, \overline{v'T'}S_T\right)}_{\text{along } \overline{T}} + \underbrace{\left(0, \overline{w'T'} - \overline{v'T'}S_T\right)}_{\text{remaining vertical}}. \tag{2.4}$$

Diabatic eddy fluxes should be down the mean buoyancy gradient. The eddy fluxes are more traditionally decomposed into an along isotherm and a remaining horizontal components (*Tréguier et al.*, 1997). We have chosen this decomposition because of numerical noise when diving by very small numbers as noted in (*Abernathey and Wortham*, 2015) when calculating eddy diffusivity over vanishingly small temperature gradients. This methods allows us to make a direct comparison possible between diabatic forcing by surface heat fluxes and by diabatic eddies in the surface mixed layer:

$$\underbrace{\frac{\partial \overline{v}\overline{T}}{\partial y}+\frac{\partial \overline{w}\overline{T}}{\partial z}+\frac{\partial \overline{v'T'}S_T}{\partial z}+\frac{\partial \overline{v'T'}}{\partial y}}_{\text{Adiabatic advective fluxes } (\nabla\cdot\overline{\mathbf{u_A}T})}=\underbrace{\frac{\partial Q}{\partial z}}_{\text{air-sea fluxes}}-\underbrace{\frac{\partial\left(\overline{w'T'}-\overline{v'T'}S_T\right)}{\partial z}}_{\text{Diapycnal fluxes}}=\frac{\partial(Q-D)}{\partial z}, \tag{2.5}$$

with

$$D=\overline{w'T'}-\overline{v'T'}S_T \tag{2.6}$$

It is noted in *Plumb and Ferrari* (2005) that these "raw" eddy fluxes contain reversible diapycnal mixing as well as irreversible mixing and will typically be much larger than the true irreversible diabatic eddy fluxes. The L.H.S will only represent the residual flux divergence when the flow is adiabatic below the surface mixed layer. In a Cartesian framework these terms acts as approximations for the heat budget of diabatic eddies and adiabatic fluxes but will differ from the residual mean counter parts that require additional surface mixed layer assumptions (discussed in chapter 1) in order to calculate. When we refer to diabatic eddy heat flux divergence we acknowledge by this definition additional reversible fluxes will be included so these fluxes will be quantitatively larger than the true irreversible diabatic fluxes.

It should be stressed that the diabatic surface mixed layer is the layer over which Q and D go to zero. This layer equals the depth of the (winter) convective mixing or (winter) mixed layer. In our model seasonality is excluded, but the mixed layer

depth can still be O (100 m), or even O (1000 m) in some experiments we will discuss later in this chapter.

Tracer evolution by the SO ROC is purely advective (non divergent), so that:

$$\nabla \cdot \overline{\mathbf{u}T} = \overline{\mathbf{u}} \cdot \nabla \overline{T}. \tag{2.7}$$

This arises from the continuity equation:

$$\overline{\nabla \cdot \mathbf{u}} = 0. \tag{2.8}$$

In continuous equations if Eq. (2.8) is true then Eq. (2.7) must be true. This however, does not hold in a discrete model due to tracer and velocity grid alignment when using Reynolds decompositions. This has implications for discretizing the continuous equations from *Marshall and Radko* (2003), in fact we must use $\nabla \cdot \overline{\mathbf{u}T}$. With out Eq. (2.7) we can not write the bouyancy budget in terms of stream-functions. For this reason we will use the heat budget of Eq. 2.5 to diagnose the contribution by the residual circulation, diabatic eddies, surface heat fluxes, and remaining terms. The L.H.S of Eq. (2.5) is the advective transport and the R.H.S is the diapycnal divergent terms. The L.H.S will disappear when the circulation is adiabatic but will be larger than the true irreversible diabatic transport.

From the derivation of the buoyancy budget put in a TEM framework it can be noted that if the local buoyancy forcing is kept constant, in order for the heat budget (Eq. 2.5) to hold, there must be a response in the diabatic eddy heat flux if the residual circulation changes in response to changing northern boundary conditions. This is illustrated in Fig. 2.1 where the surface temperature gradient is related to the northern boundary stratification through geometrical arguments:

$$T_(y) = T_N(z = yS_T), \tag{2.9}$$

Table 2.1: Model Setup for flat bottom fixed-surface flux experiments.

Symbol	Description	Value
L_x, L_y, H	Domain	1000 km, 2000 km, 2985 m
L_{sponge}	Length scale of sponge layer	100 km
Q_0	Surface heat flux magnitude maximum	10 W m^{-2}
τ_0	Max surface wind stress	0.2 N m^{-2}
dx, dy	Horizontal grid spacing	5 km
dz	Vertical grid spacing	10-280 m
Adv Scheme	7^{th} order centred	7
τ_R	Sponge relaxation time scale	3-day - ∞
r_b	Linear bottom drag parameter	1.3 x 10^{-3} m s^{-2}

so that

$$\frac{\partial T}{\partial y} = -S_T \left(\frac{\partial T_N}{\partial z} \right). \tag{2.10}$$

2.3 Model Setup

We use an idealised channel model setup similar to *Abernathey et al.* (2011) and *Zhai and Munday* (2014). The model is based off the set up described in section 1.5 and we give a brief overview of the exact set up used here. Key model parameters are outlined in Table 2.1 and the setup is shown schematically in Fig. 2.1.

In modelling studies of the Southern Ocean, sponge layers can be used to provide a northern boundary condition representing outside processes that would maintain a background stratification, enabling the SO ROC to close (*Abernathey et al.*, 2011; *Abernathey and Cessi*, 2014; *Zhai and Munday*, 2014). By altering the relaxation rate of the sponge layer we can show how important the choice of the northern boundary condition is. We do this by changing the relaxation time scale τ_R of the sponge layer to impose a northern boundary condition of varying rigidity.

The northern boundary condition is altered by changing the relaxation time scale τ_R from days to years to decades to an infinite time scale (closed northern boundary). Short relaxation time scales strongly constrain the northern boundary stratification and the SO ROC to a circulation effectively determined by that stratification.

Increased relaxation time scales provide only weak constraints allowing the stratification to free evolve leading to a breakdown of the SO ROC. When τ_R is set to infinity the northern boundary acts like a closed wall.

2.4 Spin Up Phase

Each model run required spin ups of 400-3000 years. This varied with relaxation time scale, longer relaxation time scales greatly increased the time taken to reach equilibrium as indicated by mean Kinetic Energy and SO ROC strength. This is significantly longer than *Abernathey et al.* (2011) due to the longer relaxation time scales used here. Changes in diabatic forcing from the sponge layer also increased the internal variability so once equilibrium is achieved the model is then run for a further 100 years with results averaged over this period [1].

2.5 Overturning Response

The motivation for this study is a) the conjecture that the SO ROC vanishes when the northern boundary is closed, irrespective of the surface forcing and b) that the SO ROC can be determined by the northern boundary condition rather than local forcing. Before moving to a detailed evaluation of the processes involved, we test whether this is the case. A series of experiments were run varying the relaxation time scale τ_R in Eq. 1.55 from 3 days to a fully closed channel ($\tau_R = \infty$). The relaxation time scales used were: 3, 10, 30, 100, 1000, 3000, 10000 days and no relaxation ($\tau_R = \infty$). In this section, we show the results from 4 runs: a sponge layer with relaxation timescale of 3 ,300 and 300 days and a fully closed boundary, to allow us to establish if this is a stepped response or a smooth transition to SO ROC collapse.

[1] the 100 year average is required to close the heat budget

Eulerian Overturning

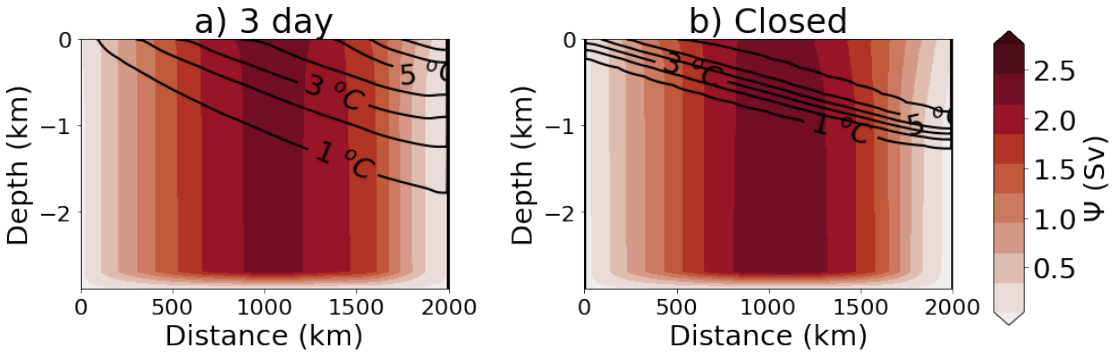

Figure 2.2: The Eulerian mean streamfunction ($\overline{\Psi}$), calculated from 100 years averaged velocities.

The Eulerian mean overturning stream function ($\overline{\psi}$) remains constant Fig. 2.2 (maximum $\approx$ 2.25 Sv, which scales to $\approx$ 60 Sv for a full channel) regardless of the northern boundary condition. This is expected as the Eulerian component is wind driven and throughout all our experiments the surface wind stress remains constant. We will not continue to show the Eulerian mean overturning in subsequent runs unless it differs from Fig. 2.2.

Calculating the Residual Overturning

The SO ROC is calculated as an isothermal stream function, there are various different methods of calculation the residual stream function and different averaging will result in differing circulations *Nurser and Lee* (2004). [2] Here we follow the thickness-weighted averaging method method of *Abernathey et al.* (2011):

$$\psi_{iso}(y,T) = \frac{1}{\Delta t}\int_{t_o}^{t_o+\Delta t}\int_0^{L_x}\int_0^T vh\,\mathrm{d}T\,\mathrm{d}x\,\mathrm{d}t, \tag{2.11}$$

where $h = \dfrac{\partial z}{\partial T}$ is the layer thickness in potential temperature (T) and the averaging period Δt is 100 years. The isothermal stream function is calculated over 42 discrete

[2]The isothermal steamfunction is a very good approximation for the residual stream function, but we note that this deviates from the complete ROC in the surface layers.

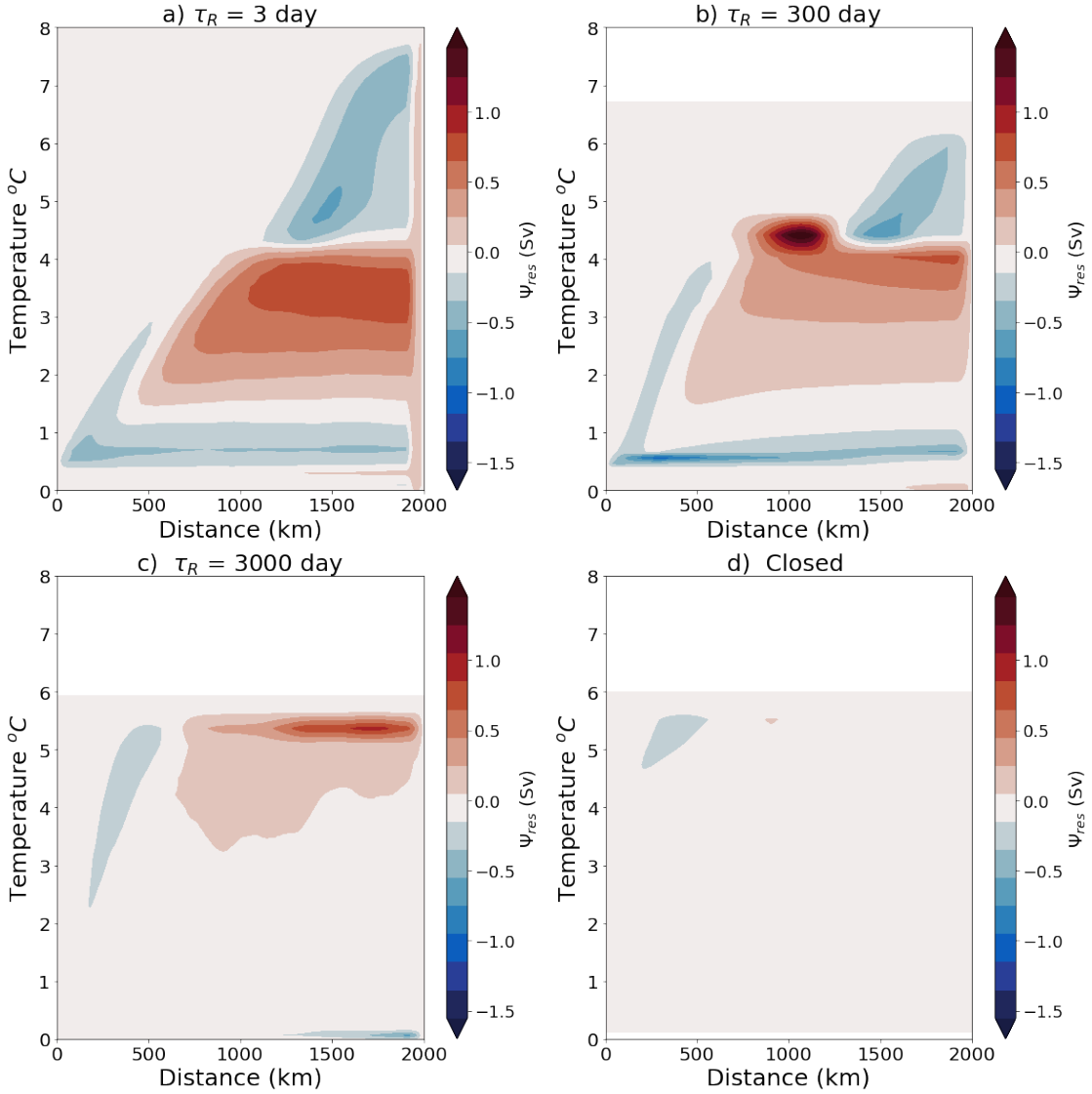

Figure 2.3: The isothermal stream function $\Psi_{res}(y, T)$ for a) $\tau_R = 3$ day, b) $\tau_R = 300$ day, c) $\tau_R = 3000$ day and d) no relaxation.

potential temperature layers shown in Fig. 2.3. This is done as an online calculation using the MITgcm layers package, which calculates the along-layer transport, averaging over every time-step. As we use the isothermal streamfunction as a good approximation of the residual overturning streamfunction we use $\Psi_{iso} = \Psi_{res}$. This isothermal streamfunction is then remapped onto depth coordinates to give $\psi_{res}(y, z)$ shown in Fig. 2.4. This is done by taking the isothermal streamfunction and calculating the depth of each layer by summing the layer thickness (calculated online) and interpolating the layer depth on the model grid centered z-points. It should be noted using this method the surface value in plots will actually be

$z = -10m$ for these runs rather than $z = 0m$.

Residual Overturning

When a short relaxation time scale of 3 days is applied the ROC features 3 distinct cells directed along mean isopycnals, reproducing the result of *Abernathey et al.* (2011). The SO ROC has a maximum of ± 0.75 Sv (30% of the mean) away from the surface. This is a realistic result as scaled to a full-length channel (approximately a factor of 25 times larger), a transport of 15 Sv would be obtained. This three cell structure disintegrates with increasing relaxation time scale and virtually disappears below the surface mixed layer when the northern boundary is closed Fig. 2.4.d. The mixed layer is shown as a grey line on these plots, the MITgcm can diagnose a mixed layer depth using a simple temperature difference criterion of 0.8^o C *Kara et al.* (2000), however, this is not ideal for a weakly stratified southern ocean where such temperature difference may encompass the entire water column in places. Instead here we plot the 95% Cumulative Distribution Frequency (CDF) of surface temperatures as an effective measure of surface diabatic layer depth, following the method of (*Abernathey et al.*, 2011). This is calculated using the layer probability at 95% that layer is very likely to be found at the surface and therefore be exposed to diabatic forcing. Both the CDF defined layer and MITgcm diagnosed mixed layer depth are qualitatively similar outside of the southernmost part of the domain.

When the northern boundary of the Southern Ocean is closed, there is a complete collapse of the SO ROC and very weak diabatic circulations remain that are completely confined to the surface mixed layer i.e. the depth of the convective overturning in the model. Below the surface mixed layer no circulation connected to the northern boundary can be maintained as there is no longer a means to close such a circulation away from the adiabatic interior. This underscores the SO ROC being part of an adiabatic pole-to-pole circulation (*Wolfe and Cessi*, 2011). When

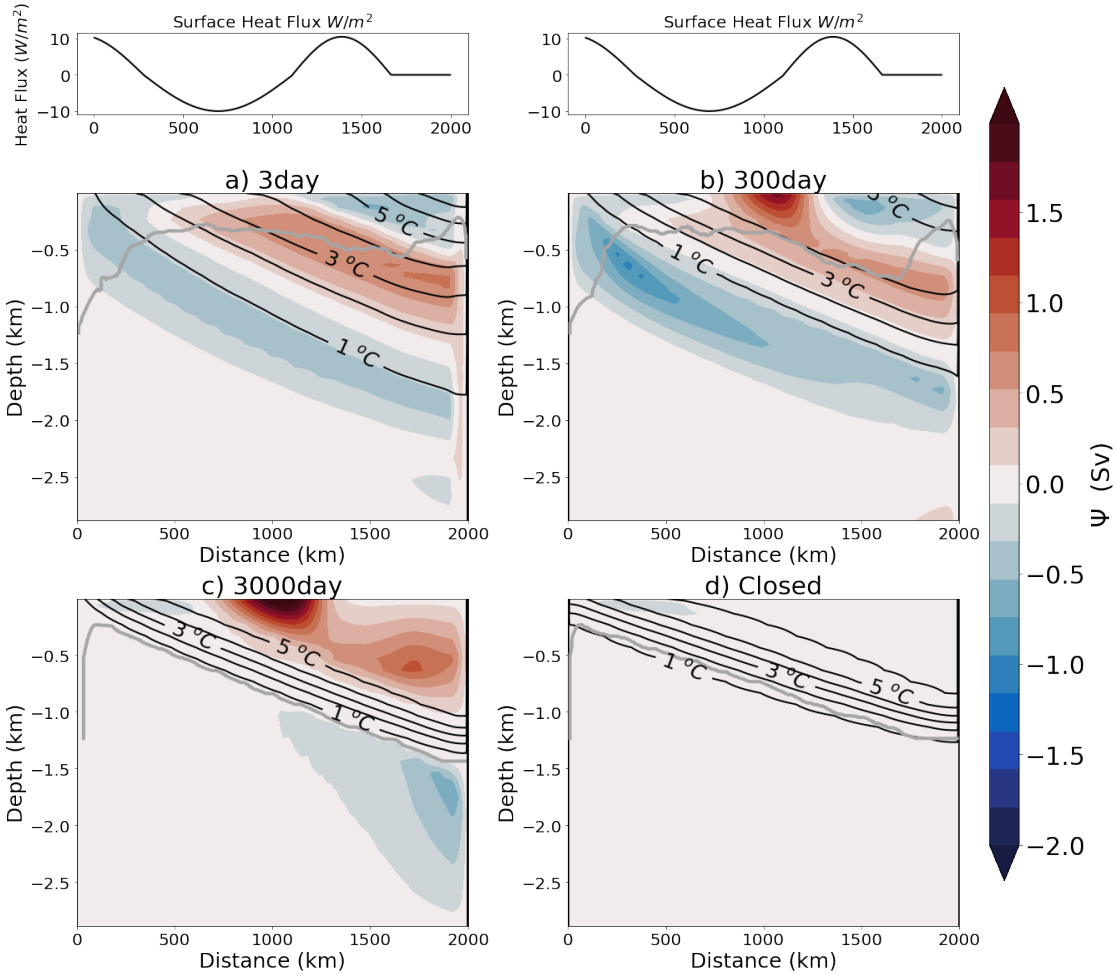

Figure 2.4: The isothermal stream function $\Psi_{res}(y, \theta)$ remapped onto depth coordinates, to give $\Psi_{res}(y, z)$ for a) $\tau_R = 3$ day, b) $\tau_R = 300$ day, c) $\tau_R = 3000$ day and d) no relaxation.The mixed layer depth is shown as a grey line. Isotherms in multiples of 1°C are overlaid as solid black contours. The surface heat forcing is displayed above.

the circulation at the northern end collapses, the circulation at the southern end is doomed to disappear as well.

Fig. 2.4 shows that changing the northern boundary condition completely alters the domain-wide stratification and the diabatic layer-depth is increased with increasing τ_R. Short relaxation time scales show the top-to-bottom stratification of today's Southern Ocean, while longer relaxation time scales set up an alternative state with a deep unstratified surface layer and a sharp internal boundary layer (Fig. 2.4. c-d). The northern boundary stratification T_N also plays an important role in setting the isopycnal slope in the interior of the domain, which can be associated

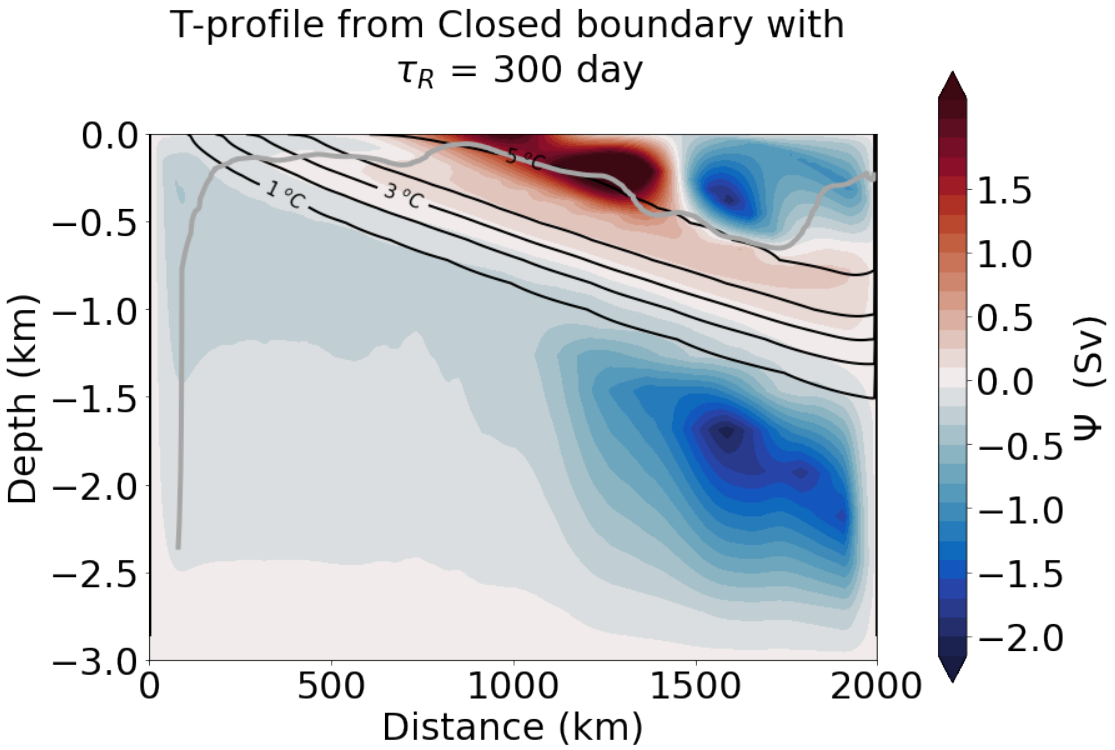

Figure 2.5: The isothermal stream function $\Psi_{res}(y, \theta)$ remapped onto depth coordinates, to give $\Psi_{res}(y, z)$ for a sponge layer relaxing to the closed boundary profile with a relaxation time scales of 300 days. Isotherms in multiples of 1°C are overlaid as solid black contours.

with a meridional buoyancy gradient allowing for the SO ROC. This result implies that not only diabatic eddy fluxes may cancel the surface heat flux in the mixed-layer, but also the role of convective mixing becomes more prominent and might be instrumental in collapsing the net surface forcing over the mixed layer. These results suggest that the SO ROC must be connected to the north of the domain in order to be maintained.

A question that arises is what is the cause of this collapse? Is it the change in stratification or the decrease in diabatic forcing in the sponge-layer? As a test we ran an experiment where the stratification is restored on a short timescale towards the profile displayed in the closed boundary run (Fig. 2.4.d. The isothermal streamfunction produced for a sponge with a 300-day relaxation timescale is shown in Fig. 2.5. The stratification becomes inconsistent with the diabatic forcing in the sponge-layer, implying an unstable solution. A small perturbation from the

prescribed profile due to an eddy, invokes a diabatic forcing term that drives the circulation further away from the prescribed profile. Using shorter relaxation timescales (3 days) results in an equally strong oscillating ROC that does not reach a steady state. These oscillations have peak to peak variations in total kinetic energy of 40% of the mean value, one to two orders of magnitude larger than in other spin-up runs. We conclude that the SO ROC is associated with net diabatic forcing and that the stratification associated with a collapsed SO ROC is inconsistent with net diabatic forcing. We address the impact of altering the boundary stratification and surface forcing systematically in chapter 3.

2.6 Heat Budget

To assess if a collapse in the SO ROC is at least partly due to a response in the diabatic eddy heat flux divergence we now move to plotting the terms of the heat budget Eq. (2.5) in Fig. 2.6. The difference between the thin grey line and the red line indicates the role of convective mixing and diabatic processes in the sponge layer. We also have included a free surface correction term required due to the linear free surface boundary condition used in the model. This is calculated by dividing the vertical mass-weighted transport of potential temperature at the surface (a diagnostic that can be calculated online) by the depth of surface cells. Although included in the thin black line term to assess how well the heat budget closes, this term is $\mathcal{O}(10^{-7})\,^{\circ}Cs^{-1}$, so essentially negligible, being 1-2 orders of magnitude less than our flux divergence terms. We plot the L.H.S of Eq. (2.5), the advective transport head divergence term as the SO ROC heat divergence (below the surface diabatic layer) in black in Fig. 2.6 and the down gradient eddy heat flux divergence as our diabatic eddy term in blue. These terms are larger than the real ROC/ diabatic eddy divergence terms due to the decomposition used. In all cases diabatic eddy heat fluxes nearly cancel the heat transport by the adiabatic ROC, with the surface heat flux being a small residual. These results suggest that for this

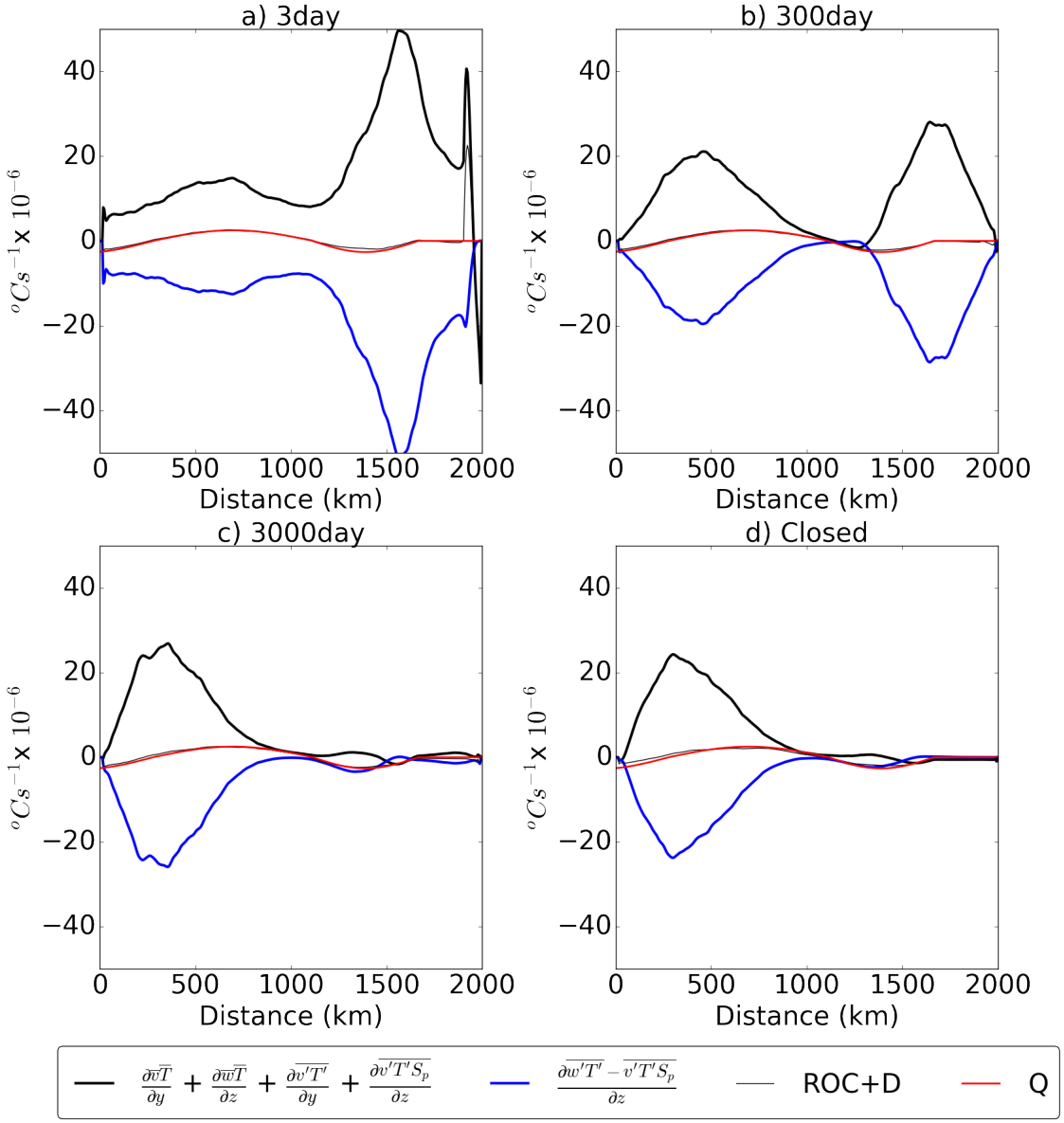

Figure 2.6: The components of the full depth buoyancy budget evaluated in as in Eq. 2.5. The advective transport component is show in black and diapycnal transport in blue, surface heat forcing in red and the total in thin black line.

set up there is no regime where diabatic eddy heat fluxes can be neglected in the budget of Eq. (2.2). In the northern 75% of the domain the heat transport by the ROC gradually decreases with increasing restoring time scale, until in the closed basin case heat transport divergence by the ROC drops to zero and the diabatic eddy fluxes almost exactly cancel the surface forcing. In the southern part of the domain a surface confined ROC cell remains and here the diabatic eddy fluxes at first order cancel the heat transport accomplished by this residual cell. Changes in convective mixing are negligible in affecting the net surface forcing over the surface mixed layer. Figure 2.6 highlights the changing diabatic eddy heat flux divergence and indicates the role of diabatic eddies in redistributing heat. However, as this figure shows the depth integrated divergence, we do not see the full spatial pattern. To investigate the distribution of the diabatic eddy heat flux divergence with depth, we plot the zonally averaged diabatic eddy heat flux divergence in latitude-depth space revealing the full extent of the diabatic eddy heat flux divergence changes (Fig. 2.7).

The figure reveals that the magnitude of the diabatic eddy heat flux convergence is increasing almost everywhere with increasing relaxation timescales. The diabatic eddy heat flux divergence/convergence disappears where there is adiabatic flow. Due to our choice of decomposition, this is not the true diabatic eddy heat flux convergence, our term is simply the down temperature gradient diapycnal fluxes. Large changes in the heat redistribution occur in the upper 1250 m. The depth over which the diabatic eddy fluxes are significant increases with increasing mixed layer depth as the relaxation time scale increases. Also, the magnitude of the heat flux divergence increases, but at the bottom of the mixed layer a dipole pattern arises, which contributes little to the integral over depth. The diabatic eddy heat fluxes remove heat from the bottom of the mixed layer and transport it to the middle of the mixed layer, allowing for the creation of a sharp internal boundary layer, as seen in Fig. 2.4b, and a deep surface mixed layer. Heat transport by the ROC (Fig. 2.8) is doing the opposite, bringing the heat downwards. At the southern end,

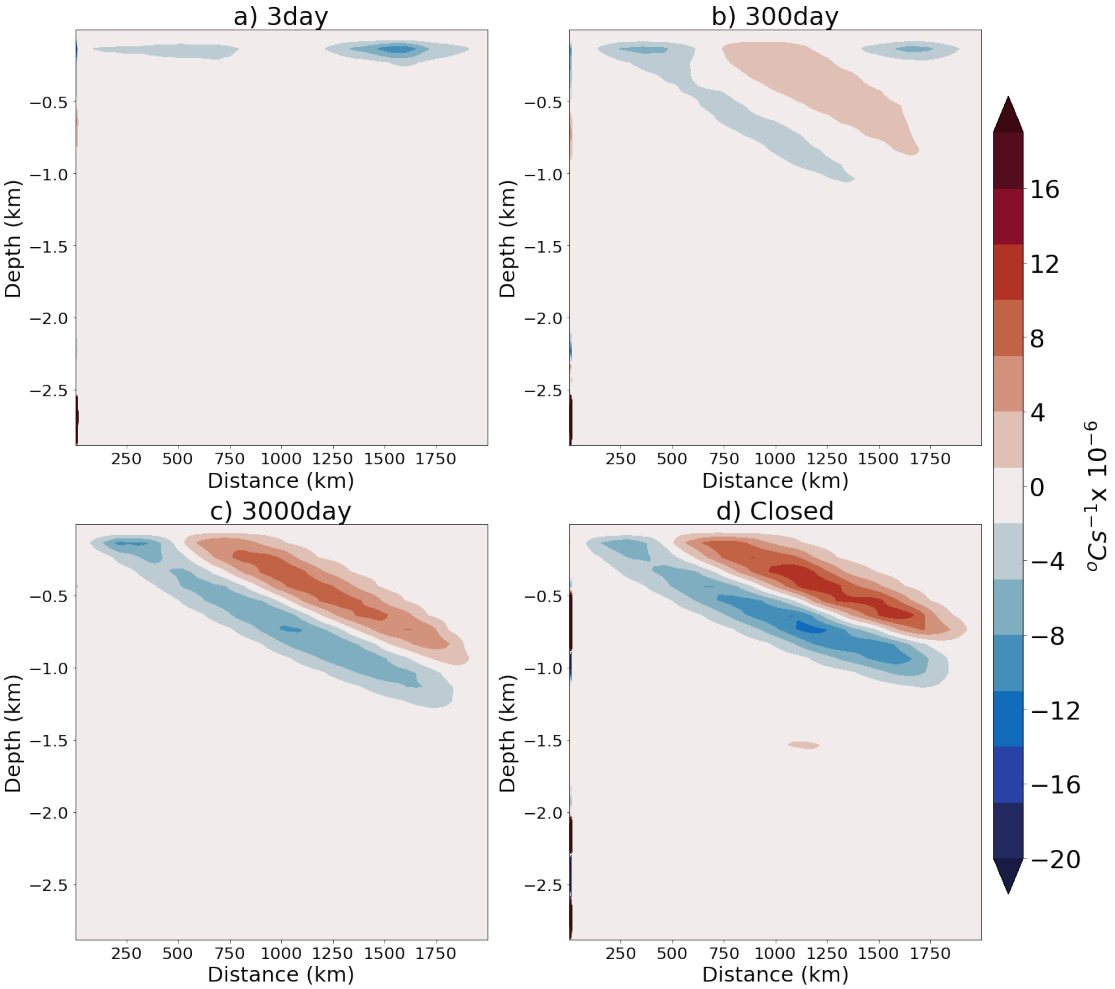

Figure 2.7: Zonal mean diapycnal heat convergence for relaxation timescale 3, 300, 3000 days and no relaxation.

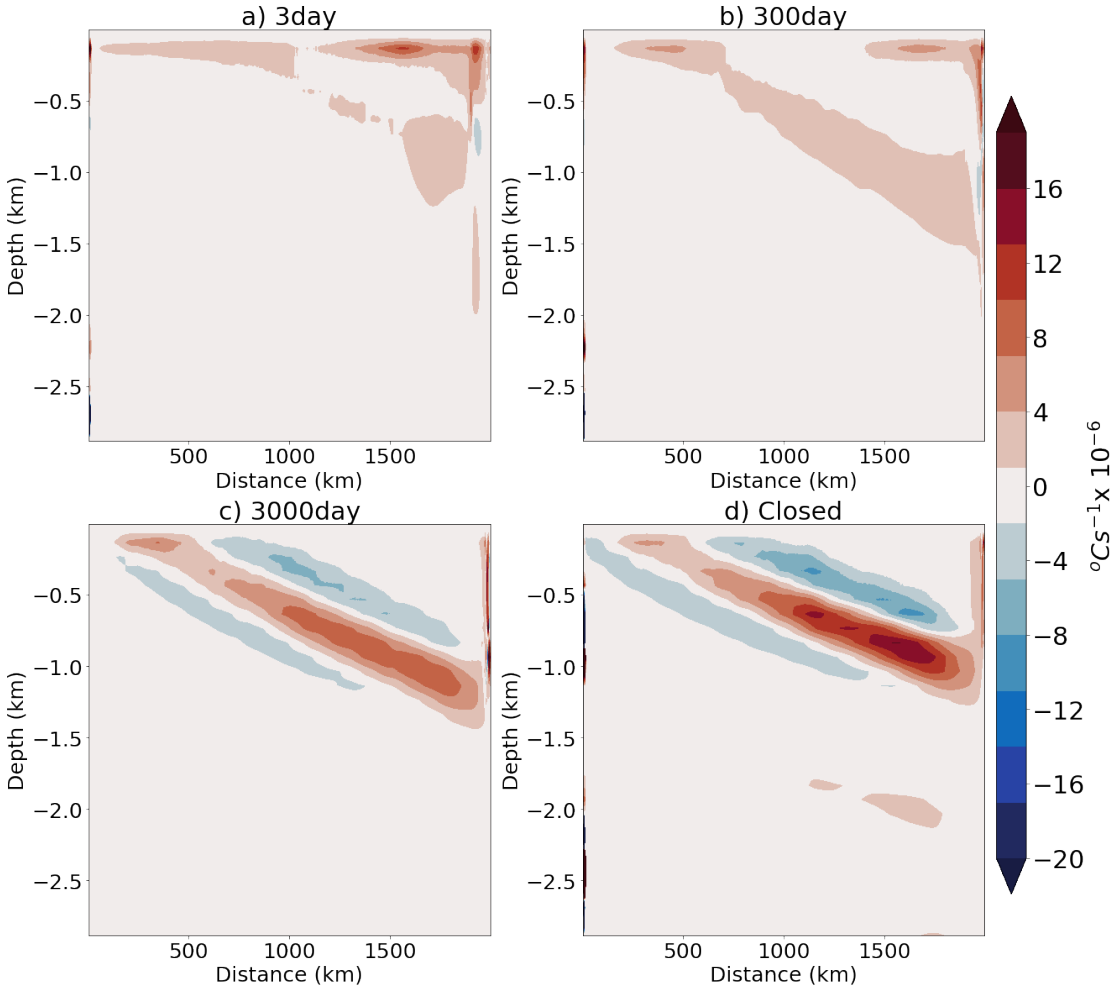

Figure 2.8: Zonal mean advective heat convergence for relaxation timescale 3, 300, 3000 days and no relaxation.

the diabatic eddies cool everywhere, opposing the heating by the surface confined ROC. At the northern end, a large area arises with weak heat convergence in the upper part of the mixed layer, with heating at the bottom due to diabatic eddies, opposing cooling by the ROC. Although the SO ROC nearly collapses, within and across the surface mixed layer a weak cell remains that is associated with non-negligible heat transport due to the increased vertical gradient in temperature. From these figures it is clear that changes in the northern boundary condition lead to large changes in the effective surface heat forcing through a diabatic eddy response. To further understand this adjustment we must consider what sets the strength of the diabatic eddies.

It should be noted that the increase in diabatic eddies is accompanied by a de-

crease of the vertically integrated diabatic eddy heat flux convergence as evidenced by comparing Figs. 2.6d and 2.7d. This occurs as the diabatic eddy heat flux convergence appears to be more and more as a perfect dipole pattern when the diabatic forcing in the sponge layer decreases. After establishment of an internal boundary layer, the diabatic eddies are associated with heating and equally large cooling in the upper and lower half of the internal boundary layer, respectively, the surface-confined ROC is associated with the opposite pattern.

2.7 Controls on Diabatic Eddies

Having found a significant response in the diabatic eddy heat flux divergence, it is now important to understand what establishes this response. The controls on diabatic eddy flux divergence can be thought of as being made up of an eddy velocity perturbation v' , and a temperature perturbation T'. A relative measure of v' can be obtained by taking the square root of the eddy kinetic energy (EKE) and a measure for T' can be obtained from taking the square root of the eddy potential energy (EPE) (*von Storch et al.*, 2012), which is given by:

$$EPE = -\int_V \frac{gT'^2 \mathrm{dz}}{2\mathrm{d}T} \mathrm{d}V \tag{2.12}$$

Gill et al. (1974) noted that changes in stratification in the upper few hundred meters can lead to large changes in stability properties; decreasing stratification leads to greater conversion from potential energy to kinetic energy i.e. increased baroclinic instability (*Legg and McWilliams*, 2001). This is exactly what we see happening when the diabatic forcing in the northern sponge layer decreases.

Figure 2.9 shows the zonally averaged EKE, with isotherms overlaid in black, and a thick grey line to indicate the mixed layer depth. Both the mixed layer depth and EKE increase, leading to large increases in diabatic eddy heat transport when the relaxation time scale in the sponge layer is increased. In the 3-day τ_R mixed

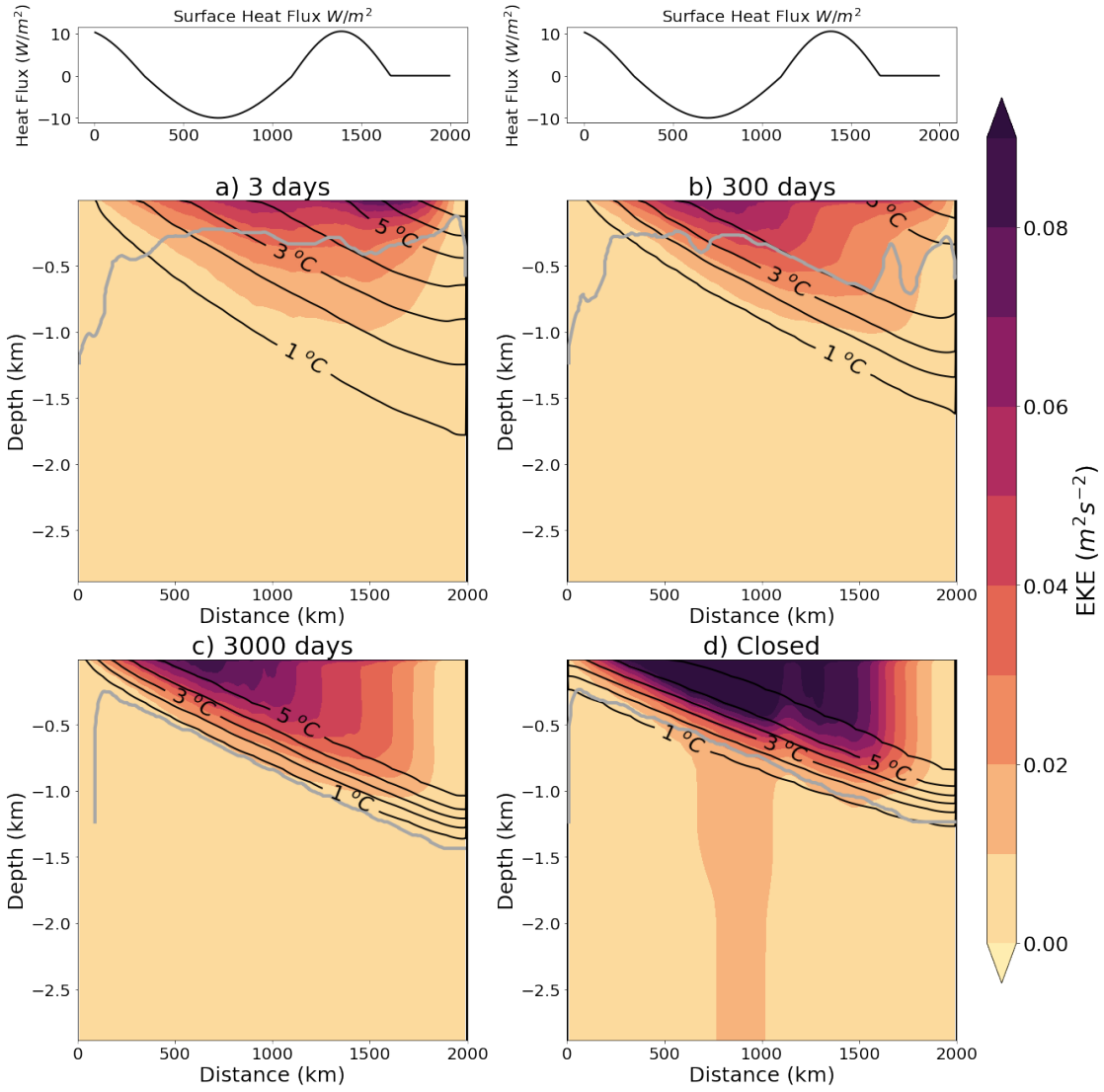

Figure 2.9: EKE $\frac{1}{2}(u^2 + v^2)$ for relaxation time scales of 3, 300, 3000 days and no relaxation. Isotherms in multiples of 1°C are overlaid as solid black contours. The light grey contour indicates the mixed layer depth. Above the surface heat forcing is displayed.

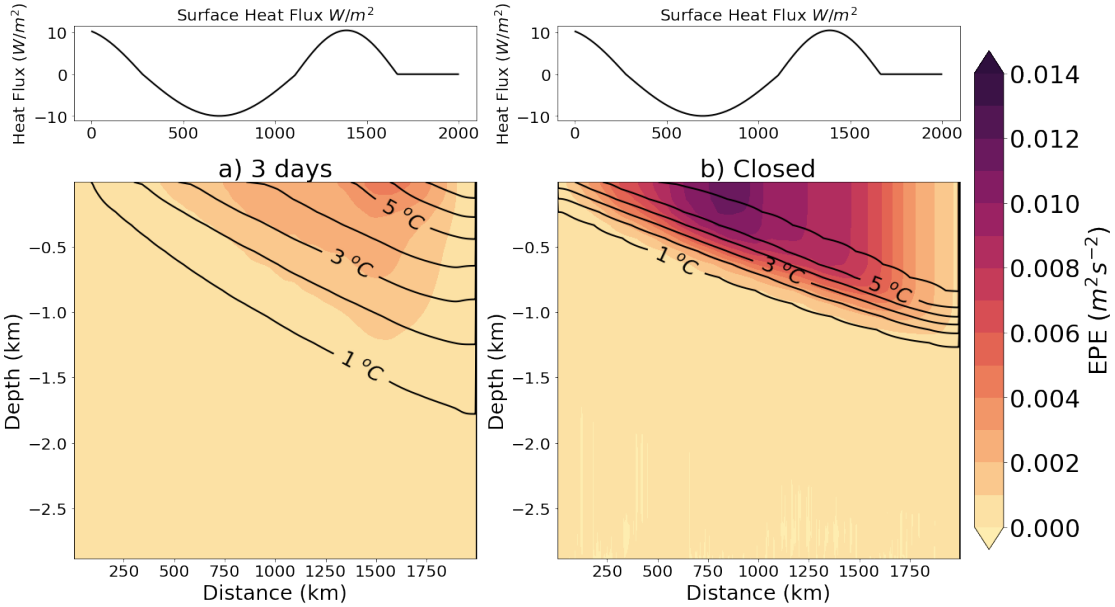

Figure 2.10: EPE $= 0.5gT'^2 dz/dT$ for relaxation time scales of 3 days and no relaxation. Isotherms in multiples of 1°C are overlaid as solid black contours. Above the surface heat forcing is displayed.

layer depth is almost similar to the 300-day relaxation timescale layer depth, but once an internal boundary layer starts forming in the 3000-day and closed-basin runs, the mixed layer deepens and EKE increases. A redistribution in EKE occurs, decreasing in the north of the domain and increasing in the south and at depth, a pattern that we also observe in the diabatic eddy heat flux divergence in Fig. 2.7. As relaxation time scales increase to orders of tens of years and in the closed northern boundary case, a sharp increase in EKE with decreasing stratification occurs, in agreement with *Gill et al.* (1974). The change in mean kinetic energy between the runs is an order of magnitude smaller and the increase in EPE in Fig. 2.10 is qualitatively similar to the change in EKE.

When considering kinetic energy a very clear trend of increasing KE and EKE with increasing relaxation time scale can be seen. A large increase occurs between 300 days and 3000 days. Fig. 2.11 shows a) the average increase in EKE corresponding to b) the increasing domain integrated KE. The increase in kinetic energy is almost entirely confined to the EKE component.

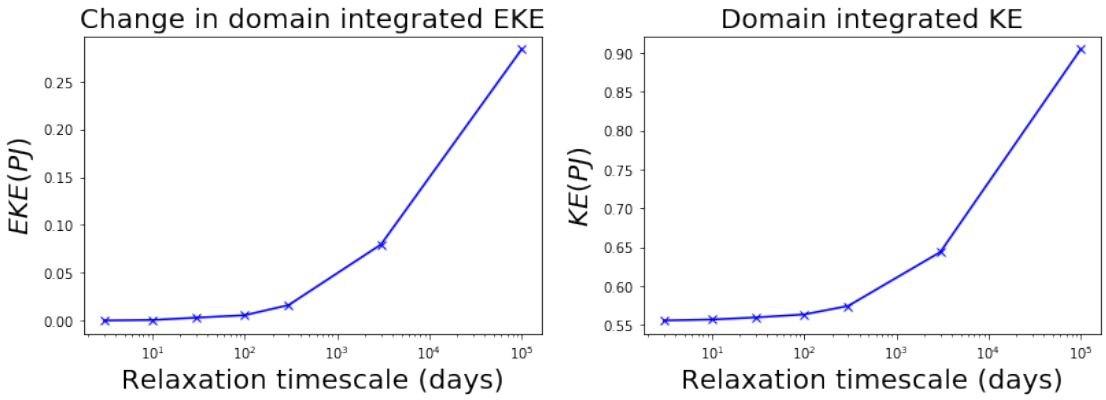

(a) EKE (b) KE

Figure 2.11: Change in kinetic energy

2.8 Conclusions

The diabatic eddy heat flux divergence strongly responds to changes in the northern boundary condition, becoming larger (increasing by 250% in amplitude) when the stratification at the northern boundary is better able to freely evolve and is less constrained by the circulation and diabatic processes in the sponge layer. The resulting changes in diabatic forcing lead to a dramatic increase in surface mixed layer depth, which leads to enhanced baroclinic instability and larger EKE and EPE.

When the northern boundary is closed there can be no interior residual overturning circulation. Although here Ψ_{res} reduces to near zero that is not necessarily a requirement, a surface overturning circulation could in theory be maintained solely through surface diabatic forcing. In the absence of diabatic forcing elsewhere the residual circulation will be confined to the surface mixed layer determined by surface heat fluxes and diabatic fluxes. When diabatic forcing becomes stronger in the sponge layer, the upper cell in the SO gains amplitude and becomes comparable to the observed SO ROC (and AMOC) when scaled up (approximately 25 times larger) to a full sized channel. In this regime the diabatic eddy heat flux divergence

is always of first order importance, counteracting the heat transport by the ROC, leaving the surface forcing as a smaller residual. We did not find any regime where diabatic eddy fluxes can be neglected.

The vertical integral of the diabatic eddy heat flux convergence decreases by an order of magnitude for weaker diabatic forcing in the sponge layer. Using fixed fluxes these changes are reconciled by the establishment of a strong internal boundary layer with a large vertical temperature gradient. As a result, both heat transport divergence by a weak ROC confined to strong northward deepening mixed layer, and the diabatic eddy heat flux divergence appear as dipoles of opposing signs. For the diabatic eddy fluxes heat convergence in the upper half of the internal boundary layer and heat divergence in the lower half occurs, while the heat transport divergence associated with the ROC in the mixed layer shows the opposite. Without diabatic forcing in a northern boundary sponge layer diabatic eddies cancel the effective surface buoyancy forcing, while the heat transport divergence by the ROC integrates to zero in the vertical. As a result, below the surface mixed layer the SO ROC completely collapses, because the connection to an adiabatic pole-to-pole circulation ceases to exist.

The upper cell SO ROC collapses when diabatic forcing in the northern sponge-layer is absent. These results underscore the inter-hemispheric link between the SO ROC and the northern hemisphere AMOC. Such links were previously demonstrated in *Gnanadesikan and Hallberg* (2000) and *Wolfe and Cessi* (2011). Here, by altering the northern boundary condition we showed how the SO ROC adjusts to changes in stratification at the northern end of the SO. Although some gradual changes can be seen with increasing relaxation timescale, this is a more stepped response between turning on or off the sponge layer when using relaxation timescale as the variable.

It should be stressed, however, that the representation of the far-field forcing, i.e. NADW formation, by a sponge layer with a prescribed e-folding stratification is

crude and should be tested against other ways of closing the SO ROC. Nevertheless, the absence of far-field forcing implies a disconnection between the SO ROC and the AMOC, and our results imply that in this case the upper cell of the SO ROC cannot be maintained. The large changes in out diapycnal fluxes indicate that diabatic eddy heat fluxes could play a crucial role in the adjustment process to such changes highlights the need for a carefully designed diabatic eddy representation in the surface mixed layer of the ocean, which should also depend on the atmospheric state and forcing. Our results also imply that although there is a significant step between the reduced diabatic forcing in sponge layers with relaxation time scale of under a year and multiple years there are already changes in the dynamics of a channel model before we see the full destruction of the SO ROC.

Chapter 3

Altering the Surface Boundary Condition

3.1 The Influence of the Surface Forcing Formulation.

Introduction

Thus far we have tested the conjecture that altering diabatic forcing of the Southern Ocean through altering a relaxation time-scale in the sponge layer affects the SO ROC through a change in diabatic eddy fluxes. This is change is motivated by the idea of diabatic forcing changing with changing climate; however, in an altered climate scenario that would lead to such large changes e.g. NADW production ceasing we would anticipate a response in the surface fluxes (*Wunsch and Ferrari*, 2004; *Gnanadesikan*, 1999). The Southern Ocean with its unique dynamics and weather systems may have a complex set of feedbacks and interactions in a changing climate. When considering the effects of changing the effective buoyancy forcing, we must investigate the possible mediators of the response to altered strat-

ification north of the ACC, represented by our northern boundary condition. The SO Sea Surface Temperature (SST) response and feedbacks to changing climate have many uncertainties (*Hausmann et al.*, 2016; *Ferreira et al.*, 2015). Estimating the air-sea flux from the bulk formulas can be subject to changing basic variables (*Cerovečki et al.*, 2011). It is, therefore, useful to consider a number of different surfacing forcing scenarios in order to enable us to consider various possibilities. Buoyancy fluxes arise from contributions of heat and freshwater fluxes (*Gill*, 1982). A positive surface buoyancy flux is associated with either cooling SST or increase in Evaporation minus Precipitation (E-P). As our experiments do not have varying salinity we can consider the approach of *Moore and Renfrew* (2002) which expresses buoyancy and freshwater fluxes as heat-equivalent fluxes:

$$Q_{BF} = Q_{HF} + Q_{FW} = \frac{\rho_0 c_p}{g\alpha} B \tag{3.1}$$

This allows us to consider fixed surface heat fluxes as representing larger contributions from Q_{FW} and surface restoring boundary conditions representing larger contributions from Q_{HF}.

First, we compare our first set of experiments using fixed surface heat fluxes with a similar set up using surface restoring used in *Abernathey and Cessi* (2014). These comparisons should give us some insight on the relevant next line of investigation to further assess the role of the surface boundary condition.

3.1.1 Set Up

To assess the sensitivity to the choice of a fixed flux boundary condition instead of a fixed surface air temperature with a restoring surface condition, a further four experiments were run using the surface forcing similar to *Abernathey and Cessi* (2014) (referred to as AC14 in plot text hereafter), where the surface temperatures

are relaxed to a linear meridional temperature gradient:

$$\theta = \Delta(\theta \frac{y}{Ly}), \tag{3.2}$$

where $\Delta\theta = 8^oC$, with τ_R set to 30 days (*Haney*, 1971). We ran two experiments with this surface restoring condition, one with a 3 day relaxation time-scale in the sponge layer, and one with a closed northern boundary. We then diagnosed the surface heat fluxes arising from the surface restoring condition and ran 2 more experiments with the diagnosed surface heat fluxes fixed. To enable us to compare with *Abernathey and Cessi* (2014) the surface restoring runs were done implementing the KPP scheme rather than using convective adjustment[1].

3.1.2 Influence on Overturning and Diabatic Eddies

Figure 3.1a shows the closed flat bottom run forced with surface restoring, generating a weak overturning cell in the upper 250 m similar to that noted in *Abernathey and Cessi* (2014) due to the diabatic effects in the surface layer. Such a circulation is hypothesised in *Kuo et al.* (2005), where buoyancy loss in the South and buoyancy gain in the North must set up and surface layer balance between residual mean and eddy buoyancy fluxes and surface fluxes when there is vanishing interior circulation. However, if we diagnose the surface heat fluxes from this experiment and apply those as a fixed surface heat flux we obtain an almost vanishing SO ROC with a much deeper mixed layer and a sharp internal boundary as in our initial experiments shown in Fig. 3.1b and c. The diagnosed heat fluxes, however, are very weak in comparison with the 10 Wm^{-2} fluxes used in the first set of experiments at less than 1 Wm^{-2}. This indicates that the surface restoring generates a different and also much weaker diabatic forcing. By including a strong sponge layer we can further test the impact of the surface forcing condition on the diabatic forcing of

[1]In section 1.5 we discussed the reasons for choice of KPP vs convective adjustment, noting for our purposes convective adjustment was most appropriate

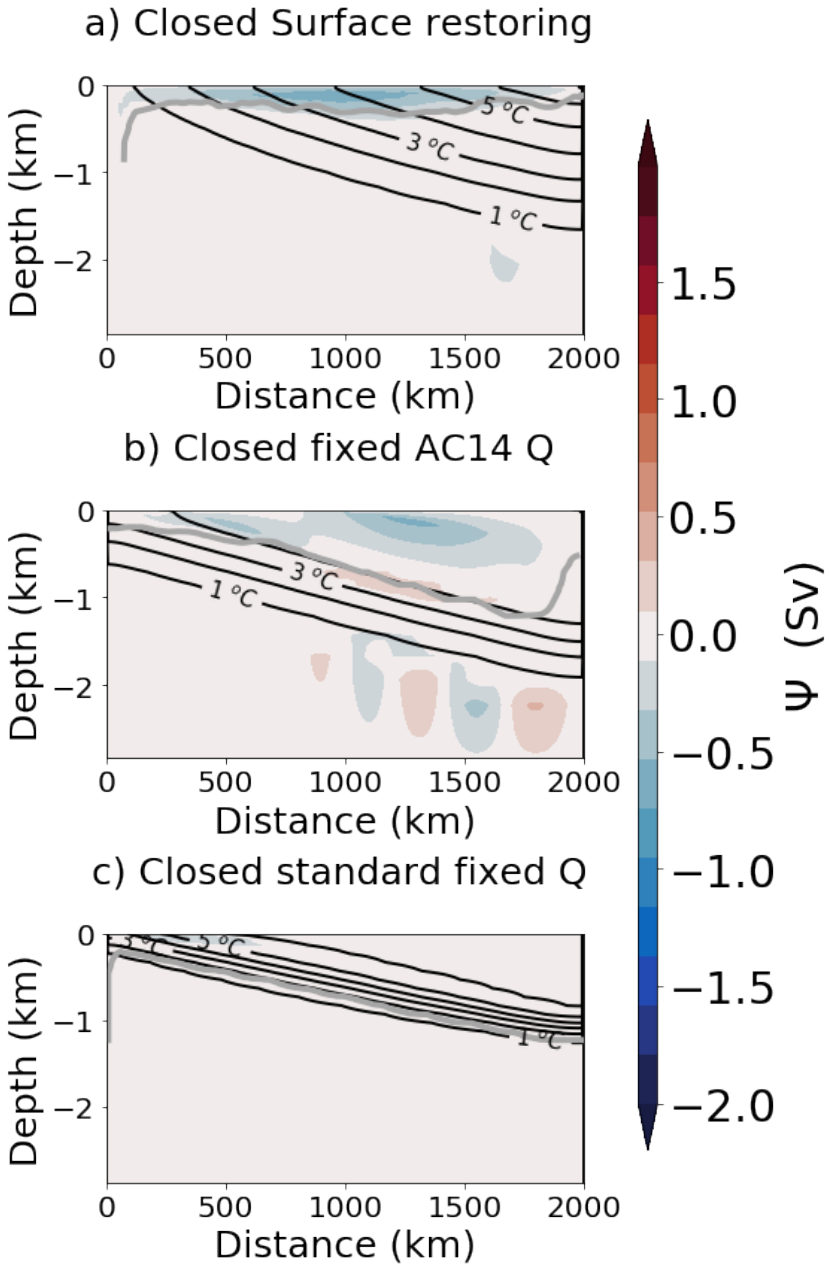

Figure 3.1: The isothermal stream function $\Psi_{res}(y, \theta)$ remapped onto depth coordinates, to give $\Psi_{res}(y, z)$. Isotherms in multiples of 1°C are overlaid as solid black contours.

the SO ROC. Fig. 3.2 shows the SO ROC for the different surface heat forcing conditions when the sponge layer is active. Fig. 3.2a shows a weak 2-3 cell SO ROC when forced with a surface restoring profile. The surface cell is weaker than when using a closed wall (Fig. 3.1a), but below the surface, a SO ROC is present, albeit weaker than in the first set of experiments. When replacing the surface restoring condition with fixed surface heat fluxes the SO ROC remains very similar (Fig. 3.2b). It is much weaker than in our first set of experiments, consistent with the weaker heat fluxes used. Note that the amplitude of the heat flux forcing in the first set was motivated in *Abernathey et al.* (2011) by the observed heat fluxes over the Southern Ocean and that the diagnosed heat fluxes from applying the surface restoring condition appear too weak (around 1 $W/m^{-}2$).

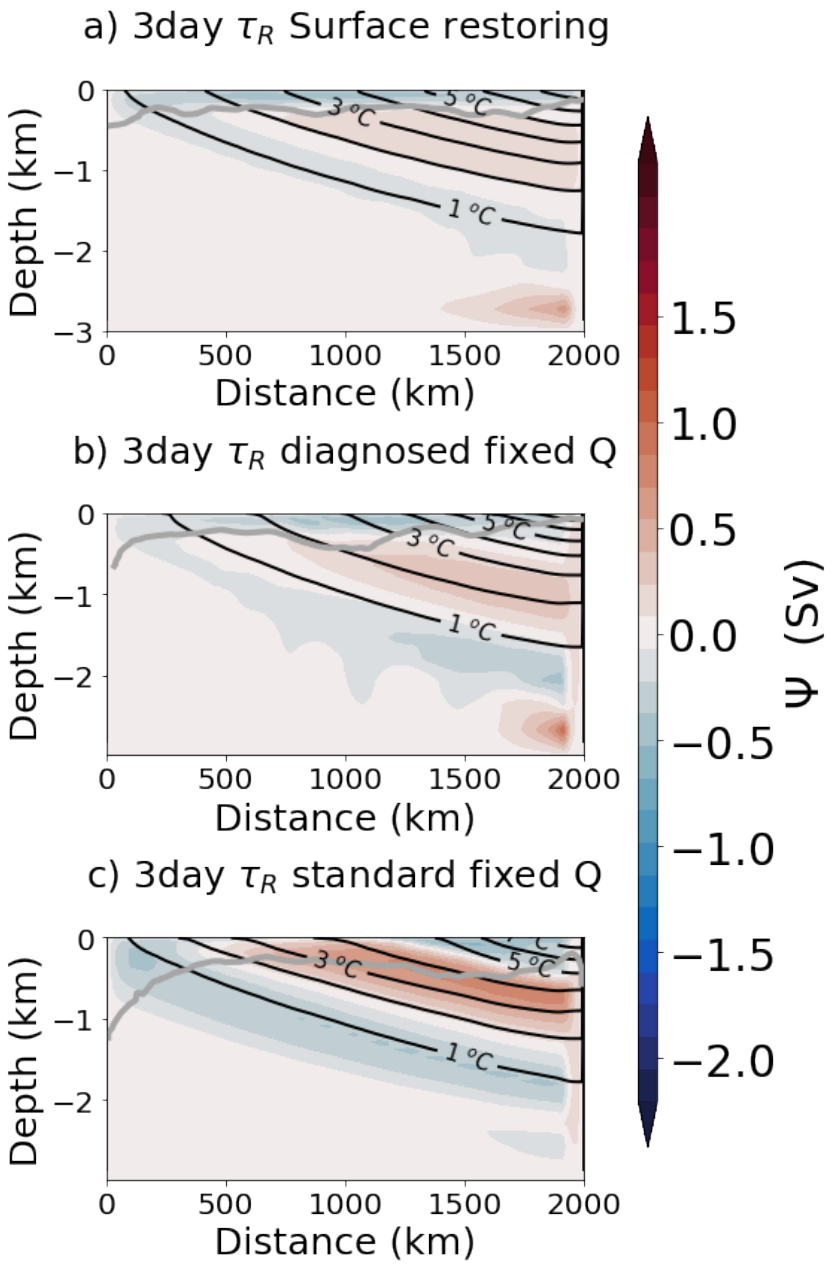

Figure 3.2: The isothermal stream function $\Psi_{res}(y, \theta)$ remapped onto depth coordinates, to give $\Psi_{res}(y, z)$. Isotherms in multiples of 1°C are overlaid as solid black contours.

We can deduce from these figures that the northern boundary is responsible for the sense and existence of the SO ROC, but that the local overturning strength is moderated by the surface heat forcing over the Southern Ocean.

To investigate whether the surface forcing conditions affect the driving mechanisms for changes in diabatic eddy heat flux divergence when the northern wall closes, we performed a heat budget analysis and plotted the diapycnal eddy heat flux divergence in depth space to compare with our fixed flux experiments in chapter 2. When a short relaxation timescale sponge layer is present all runs feature a similarly weak diabatic heat flux divergence, slightly increasing when the surface fluxes become stronger (not shown here). The closed boundary runs display larger differences, but these are mainly quantitative. All runs feature an increased diapycnal eddy heat flux divergence as well as an increase in mixed layer depth over which these fluxes occur. The dipole just above and below the bottom of the mixed layer, however, only develops when fixed fluxes are used, but appears more prominently when these fluxes are larger (Fig. 3.3a-c). We also note that for the surface restoring runs closing matching the AC14 runs the diapycnal eddy heat flux do not tend to zero at the surface partly due to the neglect of KPP heat flux terms and due to fluxes from surface restoring.

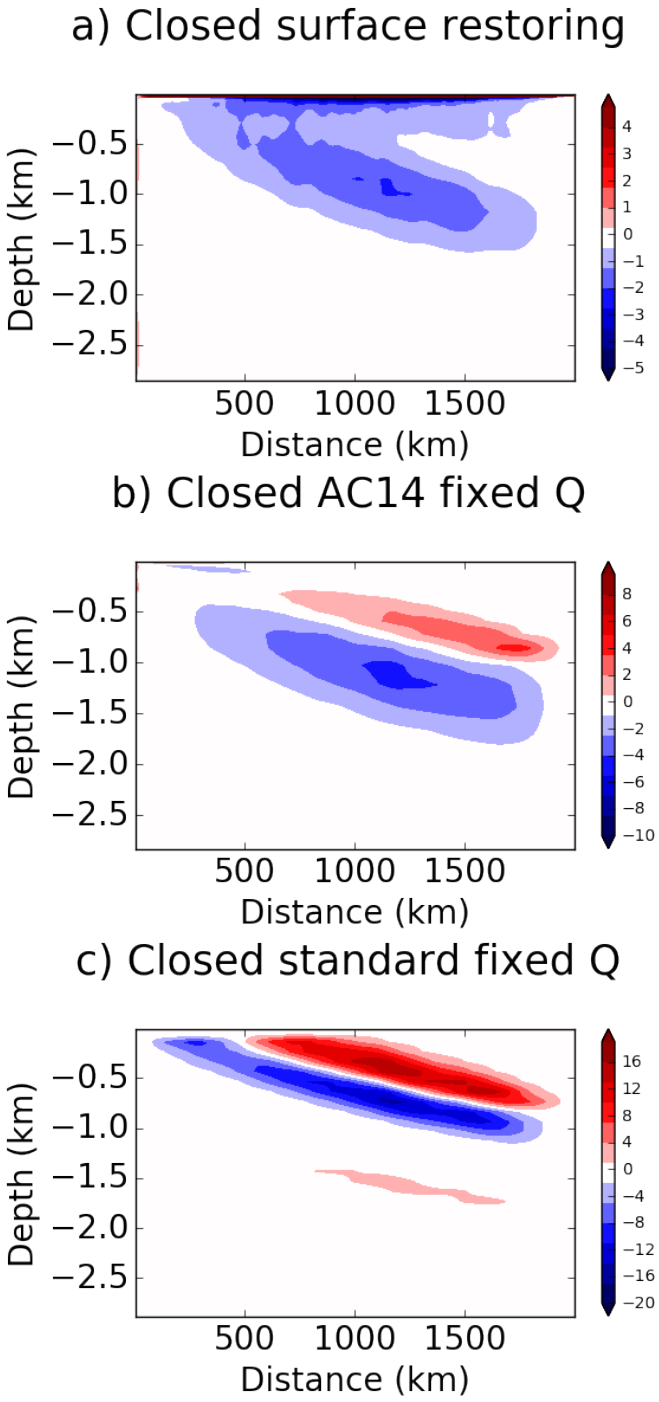

Figure 3.3: Zonal mean diapycnal heat flux divergence (D) for varying surface forcing in flat bottom closed northern boundary runs. a) Surface restoring from AC14, b) Equivalent heat fluxes, c) Original heat fluxes. Note increasing colour scale

These results imply that when surface restoring conditions are used, the increase in diapycnal eddy heat fluxes when the northern boundary is closed is much smaller than when a flux condition is used. The smaller increase is to be expected as for both the short relaxation timescale sponge and the closed wall basin the runs with temperature restoring are weakly forced by heat exchange and feature a diabatic driven overturning cell that is mainly confined to the upper 250 m, cancelling the surface forcing through advective heat divergence, without the need to invoke strong diabatic eddy fluxes. When the diagnosed surface heat fluxes from the restoring conditions are applied, both the SO ROC and stratification in the channel change and they become more sensitive to the northern boundary condition. This adjustment is associated with a larger response in the diabatic eddy heat fluxes, associated with a collapsing SO ROC. This increase, however, is still small in comparison to the increase when stronger, fixed surface heat fluxes are applied, consistent with observational estimates. In a closed basin, the larger surface forcing creates deeper mixed-layers, allowing for stronger baroclinic instabilities and larger diabatic heat fluxes.

3.1.3 Summary

One of the main differences between using restoring conditions and fixed fluxes is that, when the northern boundary is closed, with fixed fluxes a deeper mixed-layer arises in the north, with isothermals at the bottom that surface only in the southern part of the channel, causing the establishment of a sharp thermal front in the south. When restoring to a fixed temperature gradient this response is prohibited, and even in the closed boundary case, an anti-clockwise overturning in the surface layer exists. Which response is the correct one cannot be deduced from these idealised experiments. While the temperature boundary condition is closer to a restoring condition, the surface boundary condition for freshwater forcing should be more like a fixed flux condition. Ultimately, however, the large adjustments

associated with these changes in the SO ROC and diabatic processes north of the Southern Ocean would also affect the atmosphere, that is the temperature profile to which sea surface temperature is restored and associated with this, the meridional profile of the wind forcing. Since it is impossible, without using a global coupled ocean-atmosphere model, to adequately represent all these processes, the results presented here must be interpreted as envelopes, or extreme limits, of the behaviour expected in a fully coupled model. For instance, the strong adjustment in sea surface temperature profile, when using fixed fluxes, to changes in the northern boundary condition might give an indication on how sea surface and atmospheric surface temperature could adjust to such changes further north. In any case, however, we should expect the response of a fully coupled global system to be a mixture of the responses shown in chapters 2 and 3 under different boundary conditions.

3.2 Varying The Surface Forcing

In section 3.1 we compared the impact of changing the surface forcing to a surface restoring taken from the channel model of *Abernathey and Cessi* (2014). Here we wish to further investigate the role that the surface heat boundary condition plays. The behaviour in model runs with surface restoring were quite different to fixed surface heat fluxes. Fig. 3.4 shows the variation in SO ROC produced with the differing surface forcing.

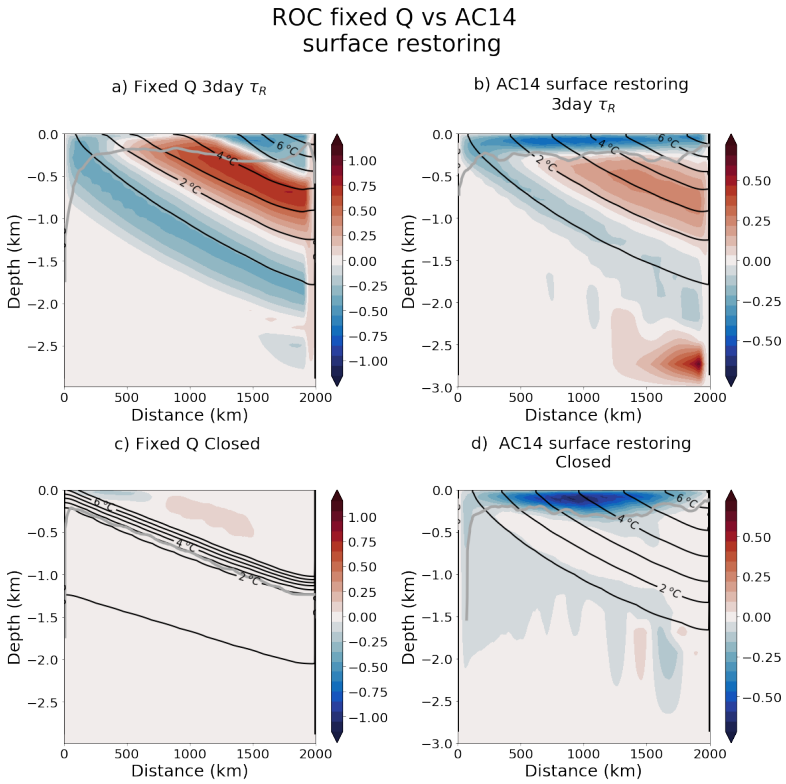

Figure 3.4: The isothermal stream function $\Psi_{res}(y, \theta)$ remapped onto depth coordinates, to give $\Psi_{res}(y, z)$ for a-b) $\tau_R = 3$ day and c-d) no relaxation. Isotherms in multiples of 1°C are overlaid as solid black contours. Note: AC14 runs b and d have rescaled colour bars to account for weaker circulation

It would appear perhaps that the surface restoring in AC14 generates a heat forcing that appears to be too weak. This provides some insight into the role of the surface forcing, but the very weak heat fluxes negate some of our comparisons. When we applied the diagnosed heat fluxes from the surface restoring runs we see a different result (see Fig. 3.1.b and Fig. 3.2.b) suggesting that the mechanics of

surface restoring is playing a role in altering the way diabatic eddies respond to altered northern boundary conditions. The main questions we wish to address are: what causes the surface overturning cell seen in runs with surface restoring? why does the deep surface mixed layer appear with fixed fluxes and not with surface restoring? Can we produce the same strength SO ROC with surface restoring alone and if not why?

3.2.1 Model Set Up

To investigate this we devised a further set of experiments. The model is once again based on the set up described in section 1.5 and we give a brief overview of the exact set up used here. The channel domain is 1000 km by 2000 km and 3000 m deep with an eddy-resolving horizontal resolution of 5 km with 30 geopotential layers, ranging in thickness from 5 m at the surface to 280 m at the bottom. Key model parameters are outlined in Table 5.1 (only values that differ from table 2.1).

Table 3.1: Model Setup parameters for the flat bottom surface restoring experiments

Symbol	**Description**	**Value**
L_x, L_y, H	Domain	1000 km, 2000 km, 3000 m
L_{sponge}	Length scale of sponge layer	100 km
Q_0	Surface heat flux magnitude maximum	0-10 W m^{-2}
dz	Vertical grid spacing	5-280 m
Open τ_R	Sponge relaxation time scale	30-day
Closed τ_R	Sponge relaxation time scale	∞
λ	Surface restoring time scale	30-300 days

The fixed surface model runs are again forced using similar zonal wind stresses and surface heat fluxes as in *Abernathey et al.* (2011) as outlined in section 1.5. For the additional runs with surface restoring we must determine a temperature profile varying with meridional distance. The profile chosen for the surface restoring is drawn from *Zhai and Munday* (2014), where we can take the surface temperature profile from our fixed fluxes runs and moderate that in order to produce the same

heat forcing pattern as our fixed flux experiments using Eq. (3.3):

$$T_s = T_{ref} - \frac{Q(y)}{\rho C_p \lambda \Delta z} \tag{3.3}$$

Where T_s is the surface restoring profile, T_{ref} is the reference profile, Q is the standard heat flux from the original experiments, ρ reference density and Δz the water depth. How the surface temperature profile must vary with varying λ is shown in Fig. 3.5. At short restoring time scales there is a more similar profile to the reference profile (closer to linear and the profile used in AC14). The 30 day time scale is justified in *Haney* (1971) to be appropriate keeping the surface temperatures very close to the surface profile.

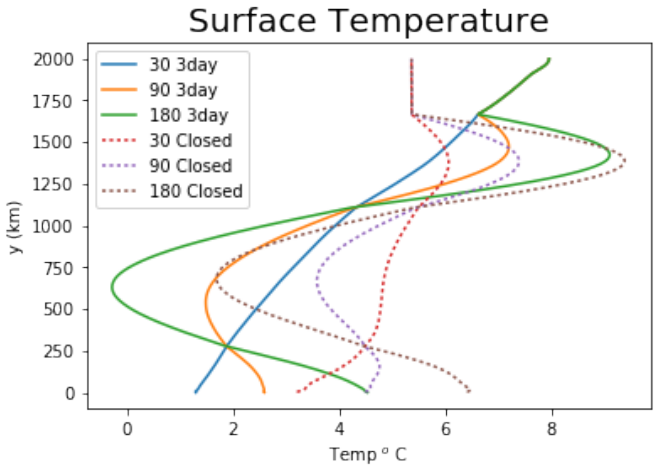

Figure 3.5: The surface temperature restoration profile calculated from eq. 3.3. Varying λ from 1 month to 6 months (30 - 300 days)

To establish the role of surface boundary condition we can adjust 3 parameters: Q, λ and T_{ref}. As mentioned previously the surface temperature is related to the stratification at the northern boundary:

$$T_(y) = T_N(z = yS_p),$$

so that

$$\frac{\partial T}{\partial y} = -S_T \left(\frac{\partial T_N}{\partial z} \right),$$

We would expect to see a difference in results when we alter the T_{ref} to that of the closed boundary simulations as this may better match the closed wall northern boundary stratification to match the diabatic forcing of the Sponge with the surface. We performed some preliminary work to assess what experiments to run, this involved finding λ that produces the closest SO ROC to our runs in chapter 2, as well as including a small fixed surface Q to increase the SO ROC and runs without either fixed fluxes or restoring. After comparing results we have used $\lambda = 90$ for our surface restoring runs. We will compare the strong sponge and closed boundary scenarios varying lambda and the reference profiles as shown in Fig. 3.5 by dashed lines. We also performed mixed surface condition runs including both a weak fixed surface heat flux ($Q_0 = 2W/m^2$) and surface restoring. The runs used are summarised in table 3.2. We also note that we adjusted the value of (M_{rbcs}) in Eq. (1.55) to

Table 3.2: Outline of runs with differing surface forcing.

Run name	**Restoring or fixed fluxes?**	Q_0	λ	**additional info**
Original	fixed	10 W/m^2	n/a	
AC14	restoring	0 W/m^2	90	with KPP
AC14HF	fixed	0 W/m^2	90	
NoQ	none	0 W/m^2	n/a	
L902Q	mixed	2 W/m^2	90	T_{ref} altered for closed
L90	restoring	0 W/m^2	90	T_{ref} altered for closed

allow for differing timescales in the sponge and surface restoring as both the sponge and surface restoring are implemented with the MITgcm RBCS package. In *Zhai and Munday* (2014) and *Abernathey and Cessi* (2014) and in section 3.1 a surface counter cell appears in the surface mixed layer that is not seen with fixed surface heat fluxes. We wish to assess what causes this and would the cell appear with surface restoring that more closely matches the fixed heat flux forcing? In *Zhai and Munday* (2014) this surface cell does disappear at surface restoring time-scales (λ) of greater than half a year and requires spinning up with strong fixed surface heat fluxes.

3.2.2 Overturning

All experiments were run focusing on the closed northern boundary and the strongest sponge scenarios. The Eulerian Mean overturning remains constant for all the runs (at a maximum of ≈2.25 Sv) as the wind forcing remains the same throughout our experiments. In this section, we look at the effects these boundary conditions have on the two extremes of northern boundary conditions. The SO ROC is calculated as before as an isothermal streamfunction (Eq. (2.11)). Fig. 3.6, shows the isothermal streamfunction in temperature space for the two extremes of northern boundary condition for the fixed fluxes for easy reference when comparing the differing surface forcing with our original strong fixed surface heat fluxes used in chapter 2.

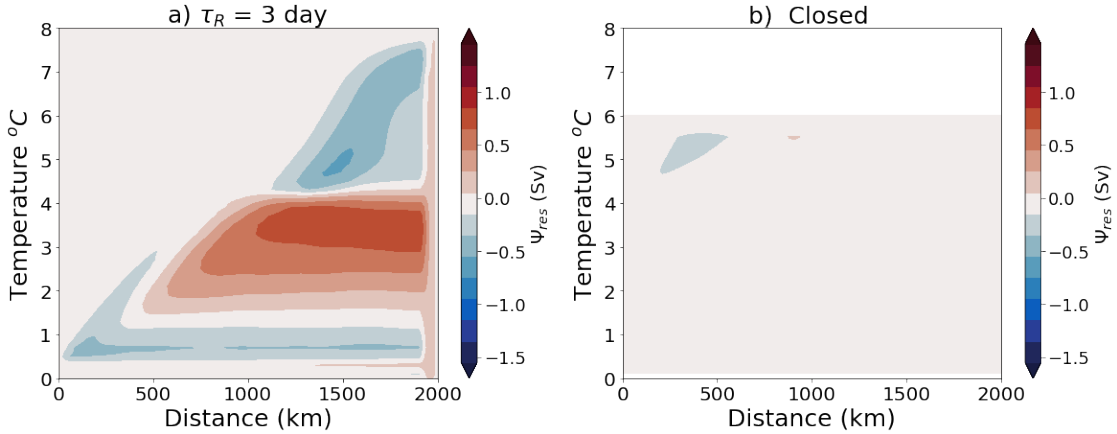

Figure 3.6: The isothermal stream function $\Psi_{res}(y, T)$ for a) $\tau_R = 3$ day and b) no relaxation.

No Surface Heat Forcing

First, we show the effects of having no surface heat forcing. Spinning up the model runs that involve no surface heat forcing requires significantly more spin up time. Kinetic energy plots suggest after 1000 year spin ups the models are yet to achieve equilibrium [2]. This leads to a noisy SO ROC. Fig. 3.7.a shows the 3 day sponge SO ROC is much diminished in the absence of either surface heat fluxes or

[2] At approximately 600 hours computing time, reaching equilibrium was not feasible.

surface restoring, at half the maximum and minimum values achieved in our fixed flux experiments. Despite the noisy nature of the SO ROC generated we can see a different overturning circulation forming; with no cooling in the south of the domain the lowermost cell is unable to form[3]. We also see the surface counter clockwise cell that appeared in our initial surface restoring runs Fig. 3.2 at a minima of -0.4 Sv. The surface diabatic layer is also shallower than the runs with a fixed surface flux never extending deeper than 500 m. When the northern boundary is closed, apart from the noise at depth, a similar response is seen in Fig. 3.7: a deep mixed layer forms with a collapsed SO ROC. It is worth noting, however, in the spin up of the closed scenario a different path to the collapsed state occurs with no surface intensification before the SO ROC disappears.

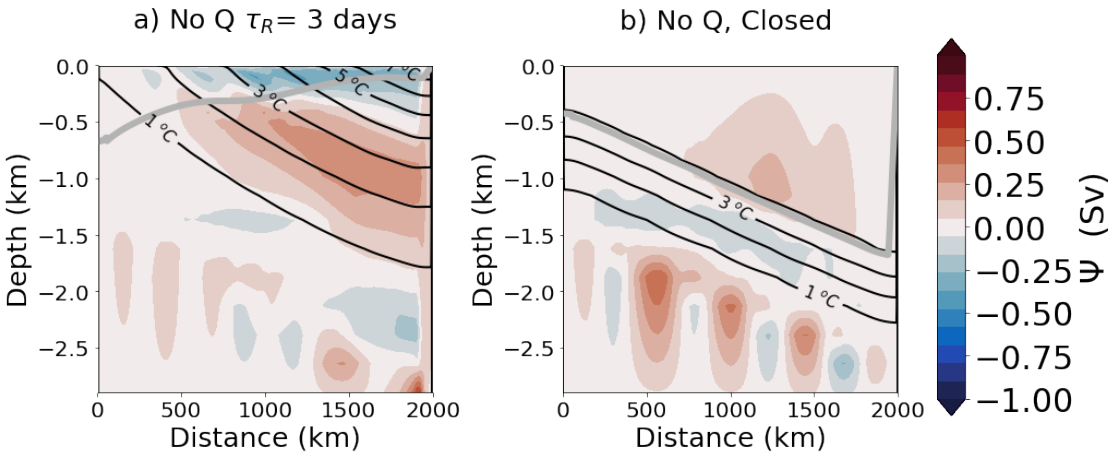

Figure 3.7: The isothermal stream function $\Psi_{res}(y, T)$ for a) $\tau_R = 3$ day and b) no relaxation, remapped into depth space.

In temperature space in Fig. 3.8.a the counter-clockwise cell that appears in the surface extends down to lower temperatures than the fixed surface flux scenario (Fig. 3.6.a but the coldest temperature layers are not able to outcrop. Where isotherms do not outcrop no SO ROC can exist. We also see the source of the noise in Fig. 3.8b), mainly in the coldest waters that expand when remapped into depth space.

[3]In the absence of topography, this may not be true if enhanced eddy diffusion could maintain circulation over topography.

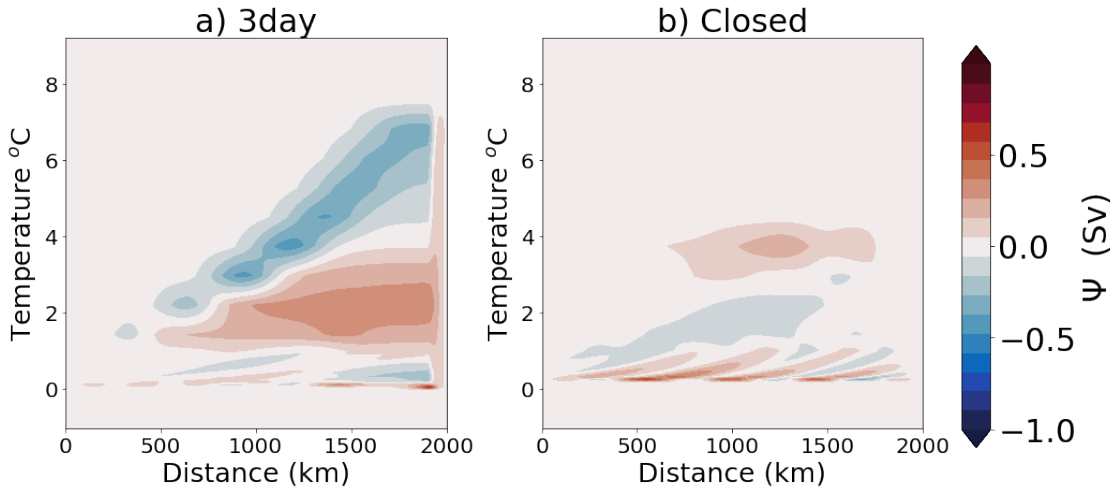

Figure 3.8: The isothermal stream function $\Psi_{res}(y, T)$ for no surface heat forcing runs: a) $\tau_R = 3$ day and b) no relaxation.

Surface Restoring

When we set λ to 90 days a strong clockwise surface overturning develops that is common to all surface restoring runs although, not seen with strong fixed surface heat fluxes. This cell was larger in runs with shorter λ. Fig. 3.9 shows the SO ROC for the extremes of τ_R and T_{ref} profile. The surface mixed layer remains similar for the T_{ref} profiles from the 3 day relaxation time scale runs in Fig. 3.9.a-b. This hints at the surface overturning cell being controlled by meridional temperature gradient we can deduce that the response to closing the northern boundary is moderated by surface conditions preventing the deep mixed layer from forming. In all cases when the northern boundary is closed the clockwise cell is unable to form Fig. 3.9.b-c and whenever surface restoring is employed the SO ROC strength remains around a third of the strength seen in the fixed flux cases.

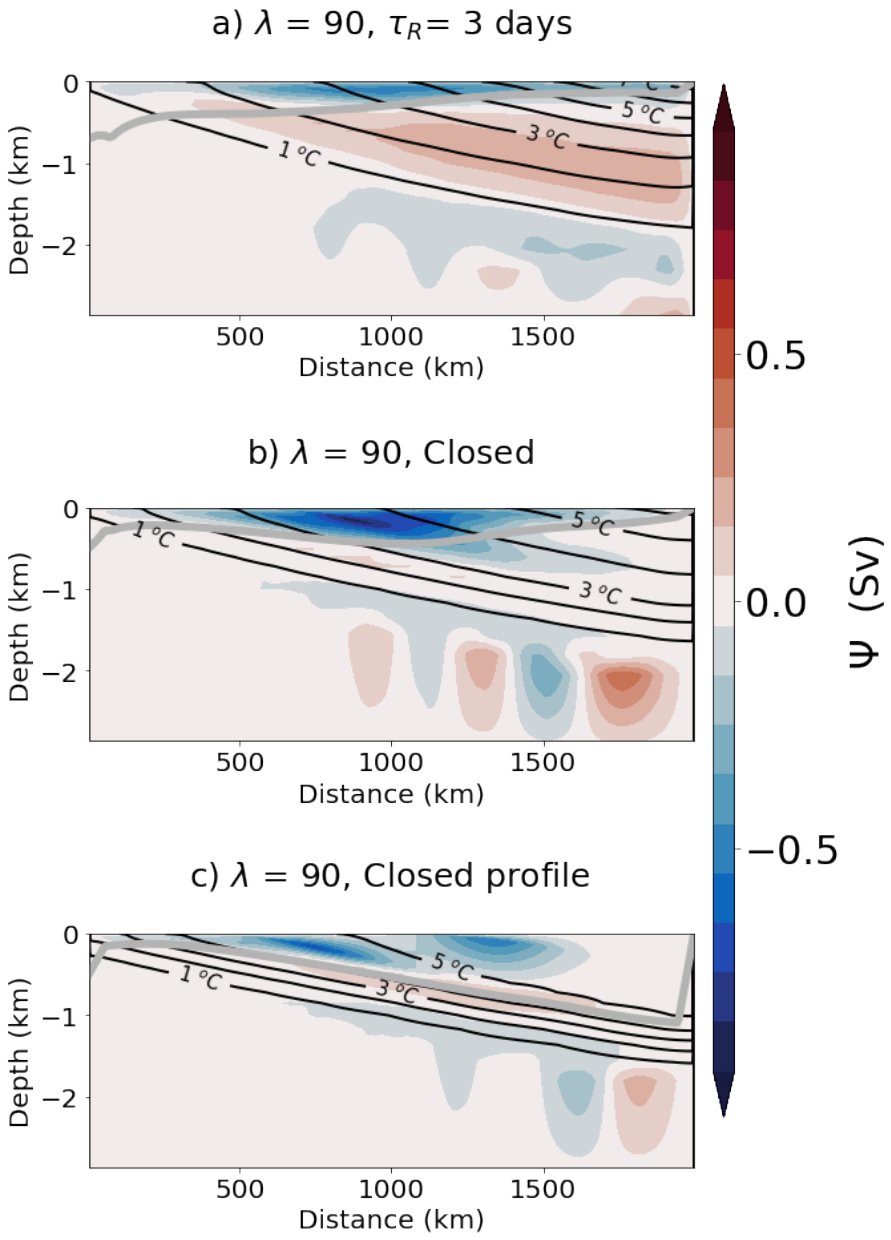

Figure 3.9: The isothermal stream function $\Psi_{res}(y,T)$ for surface restoring runs: a) $\tau_R = 3$ day, b) no sponge layer relaxation and c) no sponge layer relaxation and surface restoration reference profile set by the closed fixed flux runs. Remapped into depth space.

This behaviour is further demonstrated when we compare restoring runs Fig. 3.10 with that of the fixed flux runs Fig. 3.6. The three cell pattern seen in the fixed flux runs (Fig. 3.6.a) is not established in Fig. 3.10.a with the upper anti-clockwise cell elongated over many more latitudes and temperature layers. These long thin cells crossing many temperature layers suggest a diabatic nature to the overturning. When the boundary is closed Fig. 3.10.b keeps a strong intense surface overturning in the surface mixed layer. It is worth noting in the fixed flux run spin up a large diabatic surface cell appeared before disappearing perhaps required to redistribute heat for the new equilibrium state. In the fixed flux runs we saw a drastic shift in the surface temperature profile which is prevented here by restoring to the standard surface temperature profile. Fig. 3.9.c and Fig. 3.10.c show that when the surface temperature profile is altered the deep surface mixed layer is able to form and the SO ROC is much more similar to the closed scenario when using strong fixed surface heat fluxes.

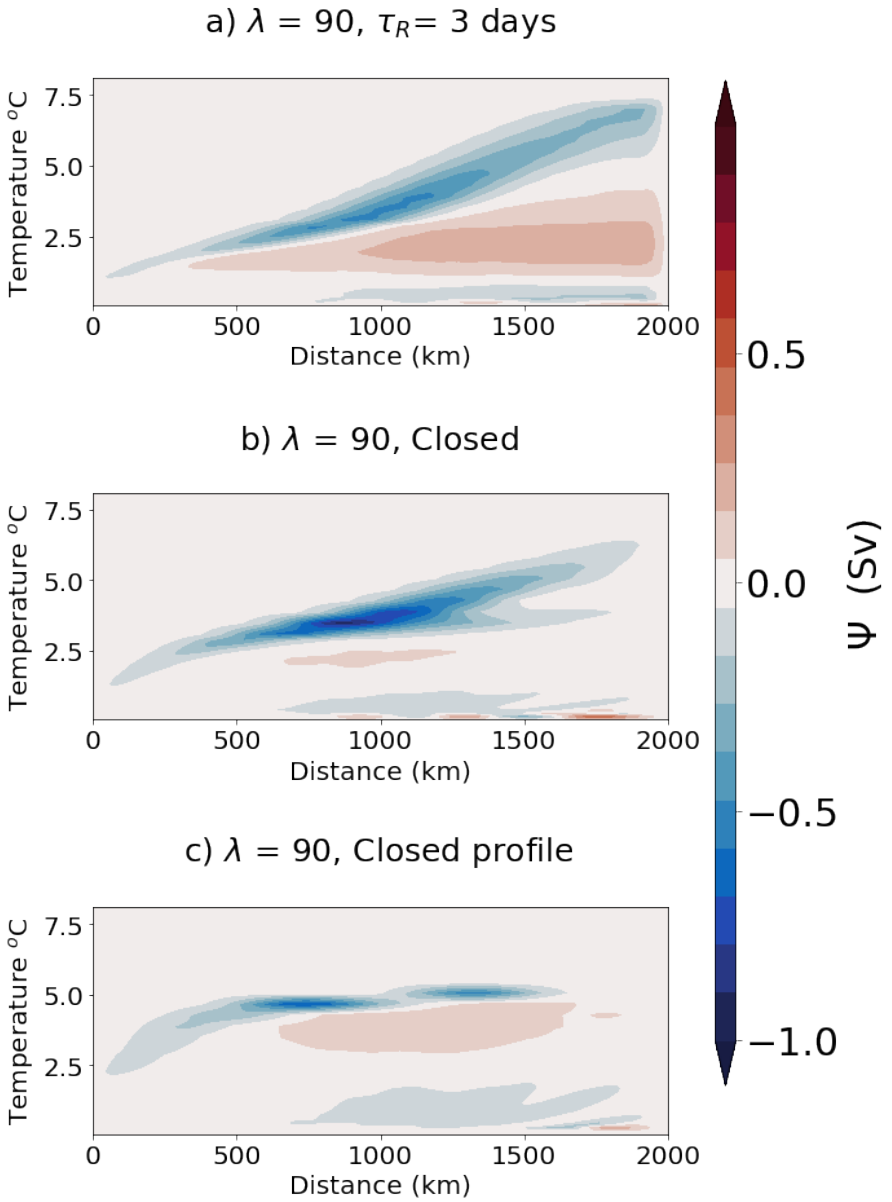

Figure 3.10: The isothermal stream function $\Psi_{res}(y, T)$ for surface restoring runs: a) $\tau_R = 3$ day, b) no sponge layer relaxation and c) no sponge layer relaxation and surface restoration reference profile set by the closed fixed flux runs.

Surface Restoring With a Small Flux

We have shown the SO ROC with strong fixed surface fluxes vanishes when the northern boundary is closed (Fig. 3.6). Compared with no surface forcing when a very weak 2 cell SO ROC consists of a surface overturning cell and clock wise adiabatic cell vanished when the northern boundary is closed (Fig. 3.8) and surface restoring runs which generates a similar structure SO ROC that does not completely vanish when the northern boundary is closed but remains as an intense surface overturning cell (Fig. 3.10). This leads us to consider the scenario of mixed surface restoring and fixed fluxes if we include a small surface heat flux, does this allow the water mass transformations required. Fig. 3.11a. shows with an surface heat flux of an additional $2W/m^2$ a much stronger SO ROC forms (around half that of the strong fixed fluxes), the additional cooling in the South of the domain also allows for the lowermost cell to form. When the northern boundary is closed the SO ROC remains the same as the surface restoring run without any additional surface fluxes added (Fig. 3.11.b.

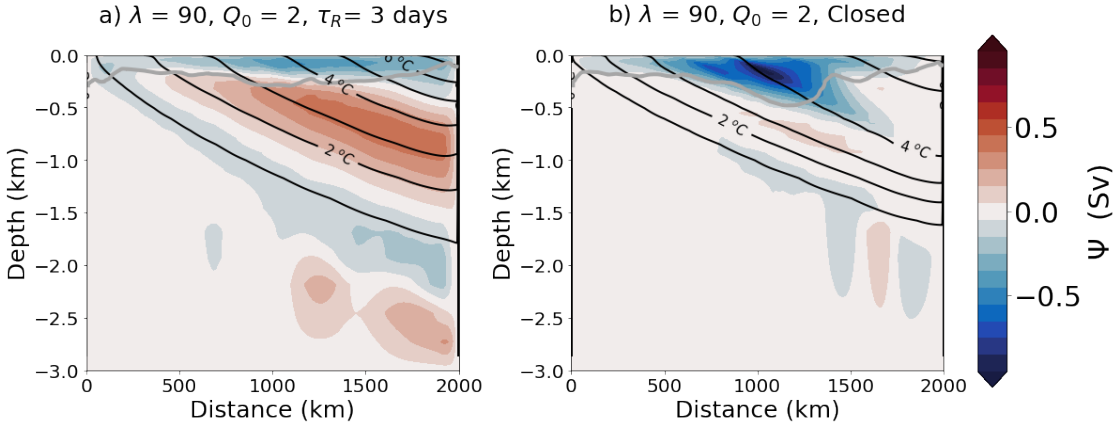

Figure 3.11: The isothermal stream function $\Psi_{res}(y, T)$ for mixed surface restoring and fixed-flux runs: a) $\tau_R = 3$ day and b) no relaxation, remapped into depth space.

This is further shown when plotted in depth space with Fig. 3.11.a now more closely matching the fixed flux scenario Fig. 3.6.a, but still with an enhanced surface cell and Fig. 3.11.b matching Fig. 3.10.b showing little effect from the addition of heat

fluxes in a closed scenario.

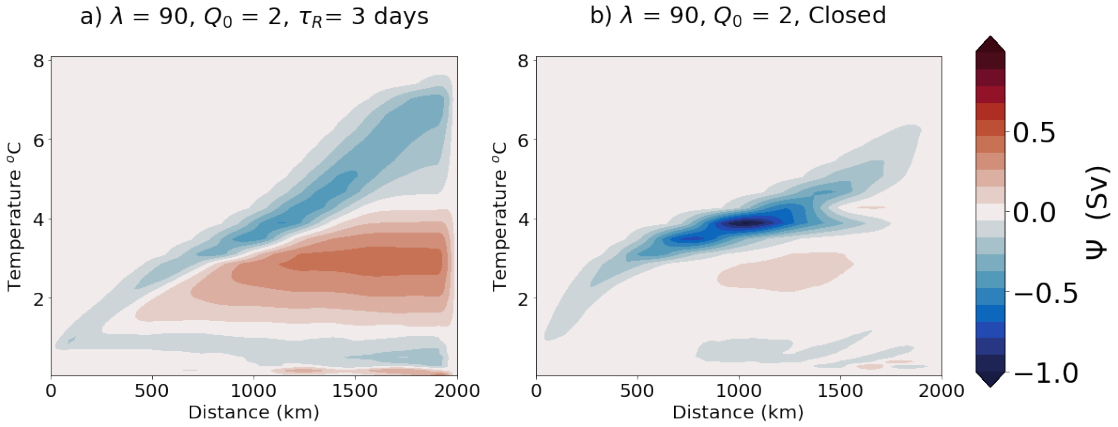

Figure 3.12: The isothermal stream function $\Psi_{res}(y, T)$ for mixed surface restoring and fixed-flux runs: a) $\tau_R = 3$ day and b) no relaxation.

These runs demonstrate the surface cell and surface mixed layer appear to be dependent on the surface meridional temperature gradient and the deep cell is dependent on cooling over the south of the domain in the absence of topography. The mixed layer depth increases with decreasing meridional temperature gradient perhaps controlling the southwards eddy-induced transport at the surface requiring further analysis.

3.2.3 Heat Budget

No Surface Heat Forcing

In the absence of any surface heat forcing when we evaluate the terms in Eq. (2.5) , with no surface heat flux terms to force heat redistribution there is little latitudinal variation in vertically integrated terms from Eq. (2.5) in Fig. 3.13. There is a peak coinciding with the maximum overturning of the SO ROC in Fig. 3.13.a which is absence in Fig. 3.13.b when there is no SO ROC present. Overall the magnitude of the heat flux divergence terms falls 10 fold when the northern boundary is closed.

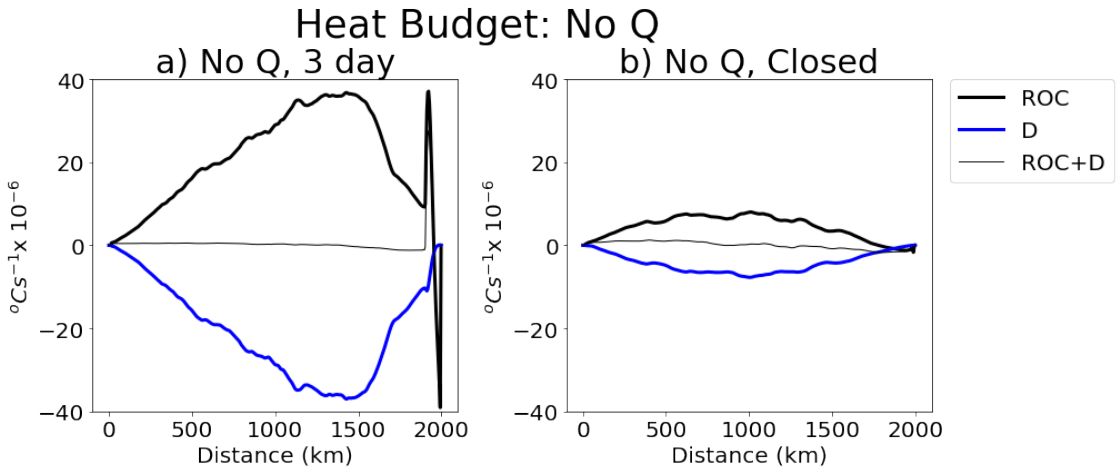

Figure 3.13: The components of the full depth heat budget of the no surface heat forcing runs evaluated in as in Eq. 2.5.

When we plot the diabatic eddy heat flux term in depth space (Fig. 3.14) we once again see the near perfect dipole pattern emerge when the northern boundary is closed contributing to the small vertically integrated values. One thing to note is the diabatic eddy heat flux divergence is separated from the surface and with out heat forcing shows no asymmetry in the divergence and convergent cells that appear in the closed scenario. The values for both are significantly smaller in the absence of surface heat forcing suggesting the surface heat fluxes must play a role in setting the strength of the diabatic eddy heat flux divergence as well as the spatial distribution (to a lesser extent).

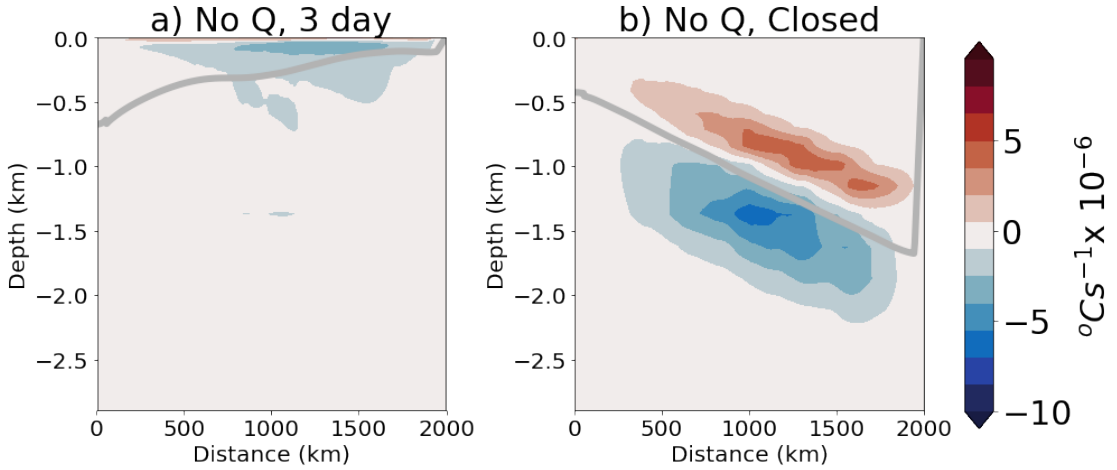

Figure 3.14: Zonal mean diapycnal eddy heat flux divergence (D) for runs with no surface heat forcing for a) Strong sponge b) Closed northern Boundary.

This is useful to see the diabatic eddy heat flux dipole and deep mixed layer appear not to require fixed surface heat fluxes Fig. 3.14.b. The dipole once again forms around the deep mixed layer.

Surface Restoring

As the runs with a small heat flux added produced very similar results to those with surface restoring alone we discuss only the surface restoring runs here for brevity. Overall the largest vertically integrated heat flux divergences are in Fig. 3.15.a when we have strong sponge layer. Turning off the sponge layer in Fig. 3.15.b reduces this by 25%, but when the closed surface temperature profile is applied alongside the closed northern boundary we get a 50% reduction Fig. 3.15.c. This is much like our original fixed flux runs when we compare the diabatic eddy heat flux divergence in depth space. A small surface convergence in Fig. 3.16.a leads to a large vertical integrated term with nothing to counteract it at depth. Unlike the surface restoring experiments we used in section 3.1 a dipole forms in the diabatic eddy heat flux divergence when the northern boundary is closed Fig. 3.16.b-c that does not arise with the restoring of *Abernathey and Cessi* (2014). When the surface is restored to the surface profile set by a strong sponge there is coherent diabatic eddy heat flux divergence Fig. 3.16.a-b, this is also seen in every run that generates the surface overturning cell (Fig. 3.14 and Fig. 3.2) and can be associated with diabatic layer clockwise overturning. This suggests the surface overturning cell is linked to the surface meridional temperature gradient. Indeed a slight decrease in surface temperature gradient occurs over the ACC in our fixed flux runs from chapter 2. When we switch to the surface temperature profile of the closed runs we get a strong diabatic eddy heat flux divergence dipole arising much like we saw in chapter 2. This also aligns with a deep mixed layer. Suggesting that a weak meridional temperature gradient allows for the set up of opposing diabatic eddy heat flux divergence cooling the upper layers and warming bottom to generate a sharp internal boundary layer.

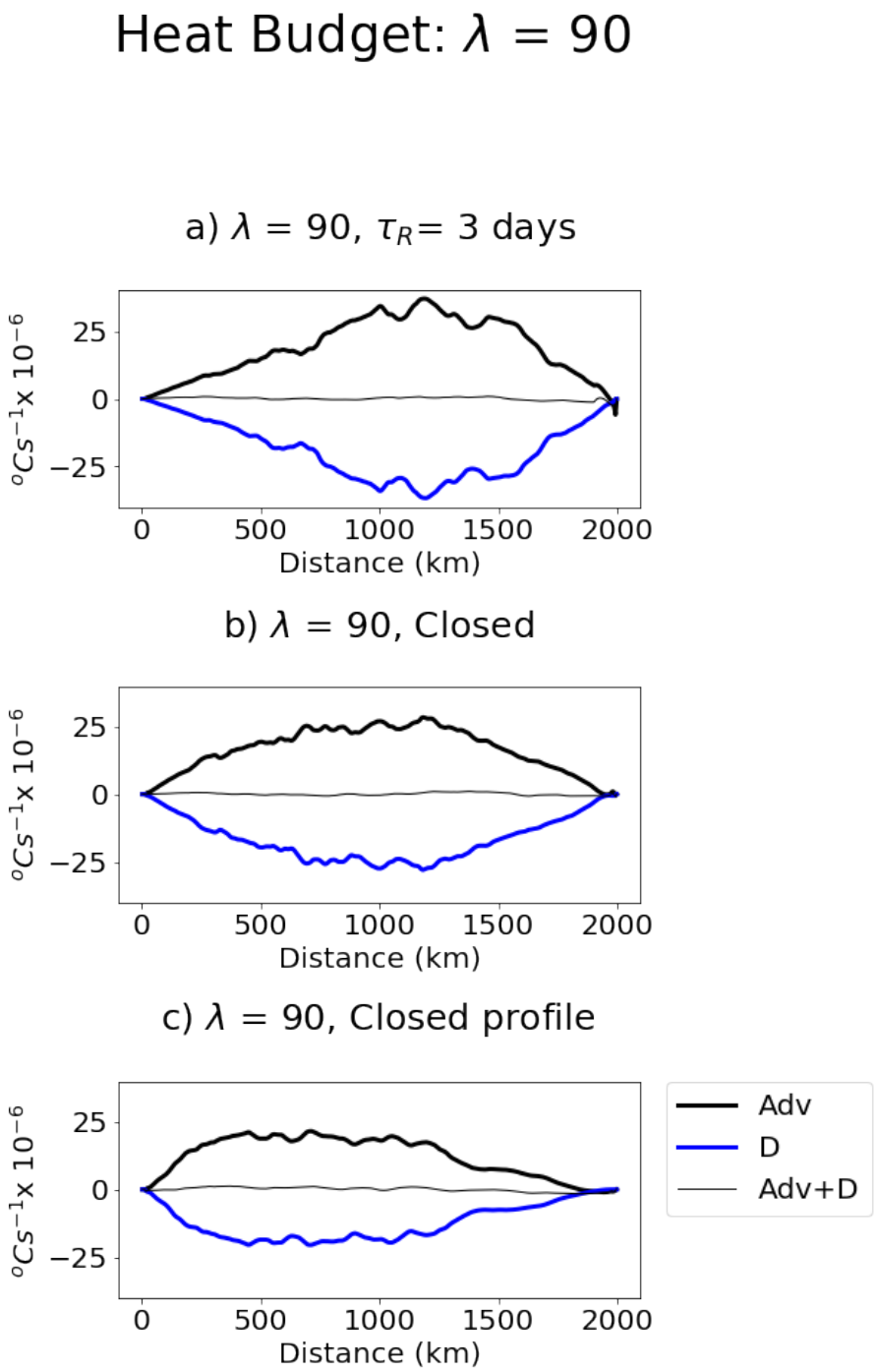

Figure 3.15: The components of the full depth buoyancy budget for mixed surface forcing runs evaluated in as in Eq. 2.5.

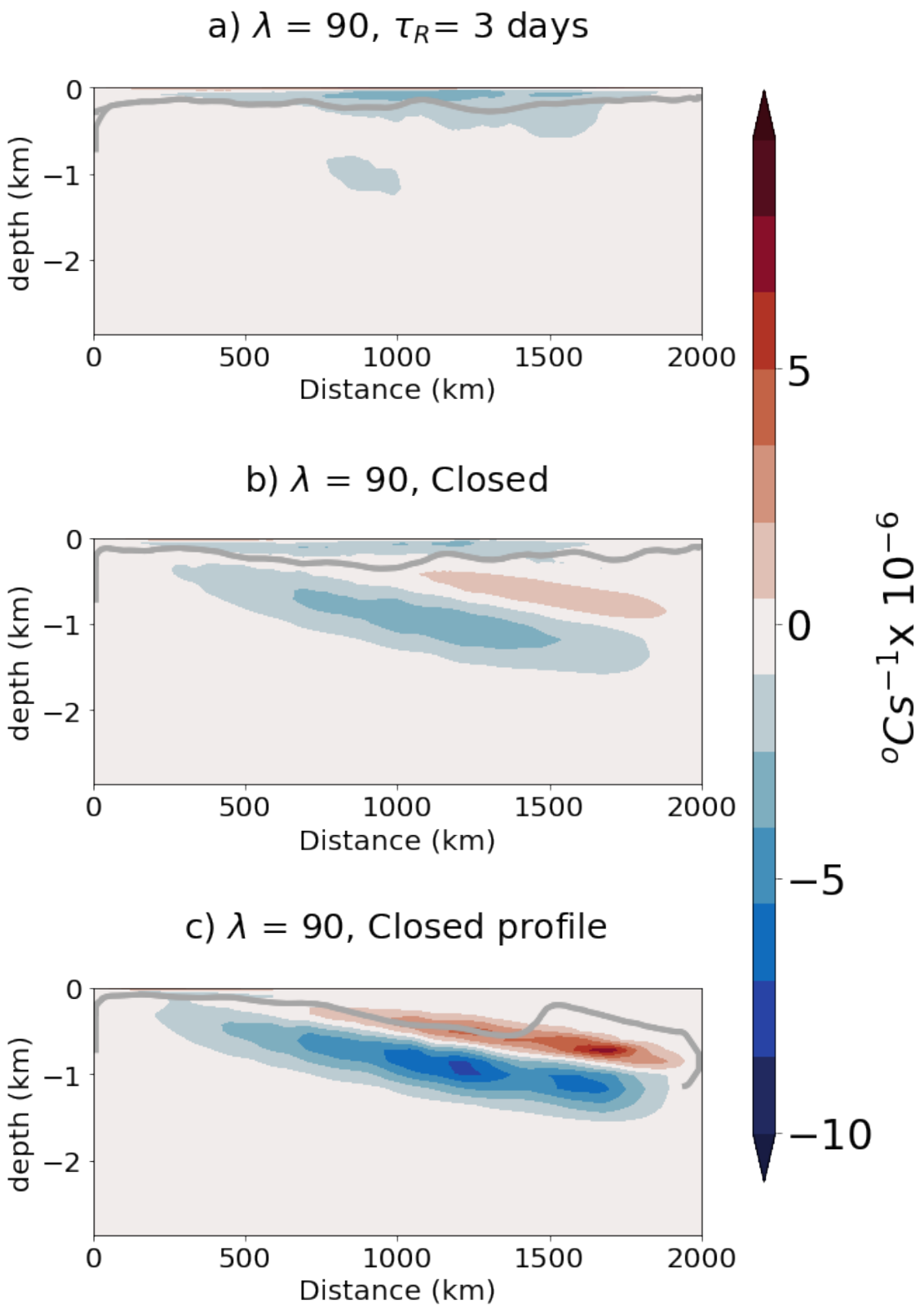

Figure 3.16: Zonal mean diapycnal eddy heat flux divergence (D) in surface restoring runs with closed northern boundary.

Energetics

No Surface Heat Forcing

With out any surface heat forcing there is a stark difference in EKE response to closing the northern boundary. Fig. 3.17 shows a decrease in EKE maxima as well as a decrease in the area over which there is enhanced eddy kinetic energy. This is not perhaps what we would expect as the same large decrease in stratification occurs in a deep mixed layer. Once again there is little increase in the Mean kinetic energy.

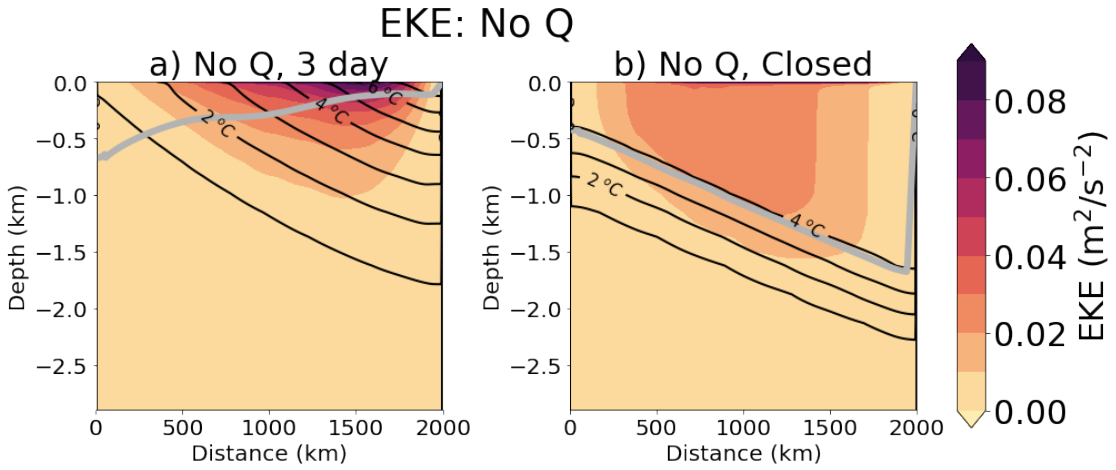

Figure 3.17: Zonal mean EKE for no surface forcing runs. a) Strong sponge, b) Closed northern boundary.

Surface Restoring

EKE remains fairly consistent across all the runs with fixed Q or surface restoring. We do not see a large increase in EKE when the northern boundary is closed but the surface restoring profile remains the same Fig. 3.18.b, but when the reference profile is set to that of the closed fixed flux runs the increase in EKE shown in Fig. 3.18.c nearly replicates what is seen in the fixed flux runs.

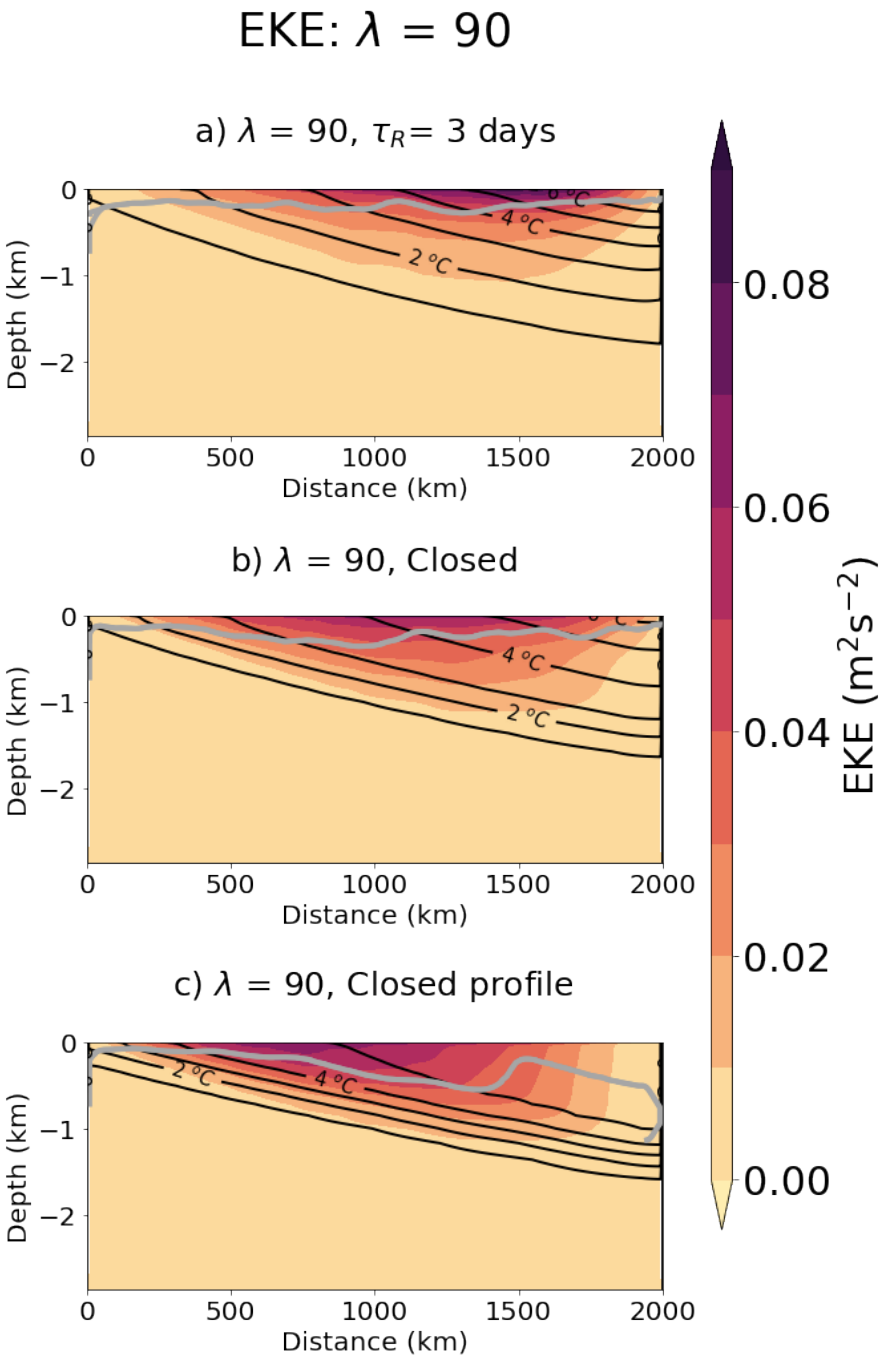

Figure 3.18: Zonal mean EKE for surface restoring runs. a) Strong sponge, b) Closed northern boundary c) Closed northern boundary and closed restoring profile.

However, EPE is generally increased with surface restoring and reduces with the addition of a fixed surface Q. EPE is plotted for our surface restoring experiments in Fig. 3.19. The surface restoring forces short time scale temperature perturbations by relaxing surface temperature to a prescribed profile which increases EPE. This is greatly increased by setting the restoration profile to closed fixed flux scenario

profile Fig. 3.19.c where large temperature perturbations are combined with sharp temperature gradients at the internal boundary layer.

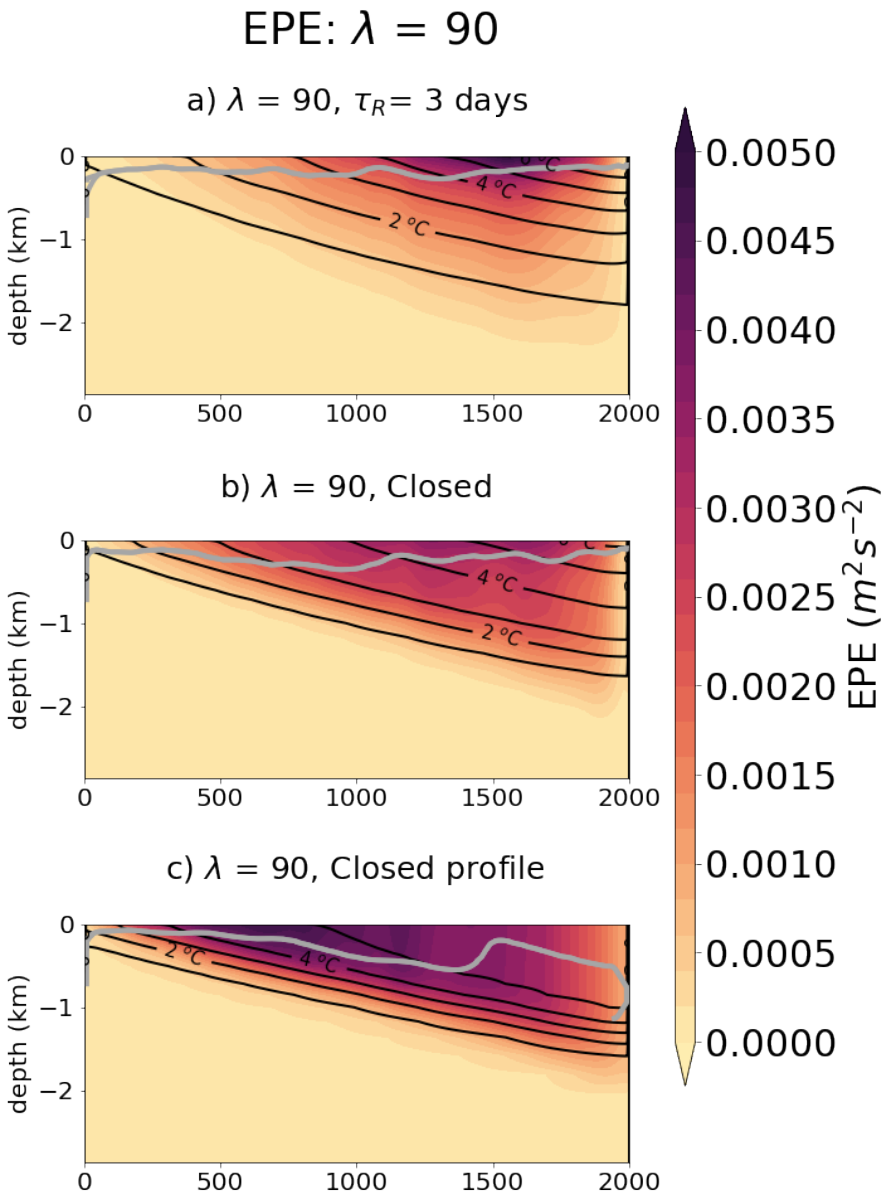

Figure 3.19: Zonal EPE for surface restoring runs. a) Strong sponge, b) Closed northern boundary c) Closed northern boundary and closed restoring profile.

3.2.4 Conclusions on Varying the Surface Boundary Condition

We did not find any regime where diabatic eddy fluxes can be neglected. Even when using restoring conditions there are diabatic circulations playing a role in setting

the overall residual circulation. The vertical integral of the diabatic eddy heat flux convergence decreases by an order of magnitude for weaker diabatic forcing in the sponge layer; however, the eddy fluxes themselves increase by a factor of 2 to 3 between a closed basin and a configuration with strong restoring to a prescribed temperature stratification in the northern sponge layer.

When using a restoring boundary condition the main balance in the vertically integrated heat budget is somewhat different because no internal boundary layer develops and the northward deepening of the mixed layer is absent except for when the surface is restored using the closed fixed flux scenario as the reference temperature. In the runs with surface restoring to a strong meridional temperature gradient the SO ROC is even more confined to the surface layer, and also in the case of a closed basin diabatic eddies and heat transport convergence by the SO ROC dominate the surface forcing. To illustrate our conclusions on the impact of surface restoring on the diabatic eddy and SO ROC response to closing the northern boundary, we include here additional plots for various surface restoring scenarios compared with the fixed surface flux scenario for the closed northern boundary runs. In the AC14 surface restoring runs, there is a much larger advective heat flux divergence in the surface Fig. 3.20.c generating a large surface overturning. This pattern is reduced with a weaker surface restoring Fig. 3.20.a, where we saw a weaker surface overturning cell, both the SO ROC heat divergence and the diabatic eddy heat divergence show less intensification surface intensification. Fig. 3.20.a is very similar to Fig. 3.20.c with a near linear reference temperature profile, but weaker restoring, the surface meridional temperature gradient is weaker, than when restoring to a reference profile from the closed scenario fixed fluxes Fig. 3.20.b begins to match Fig. 3.20.d more closely with the alternating patterns of divergence and convergence emerging.

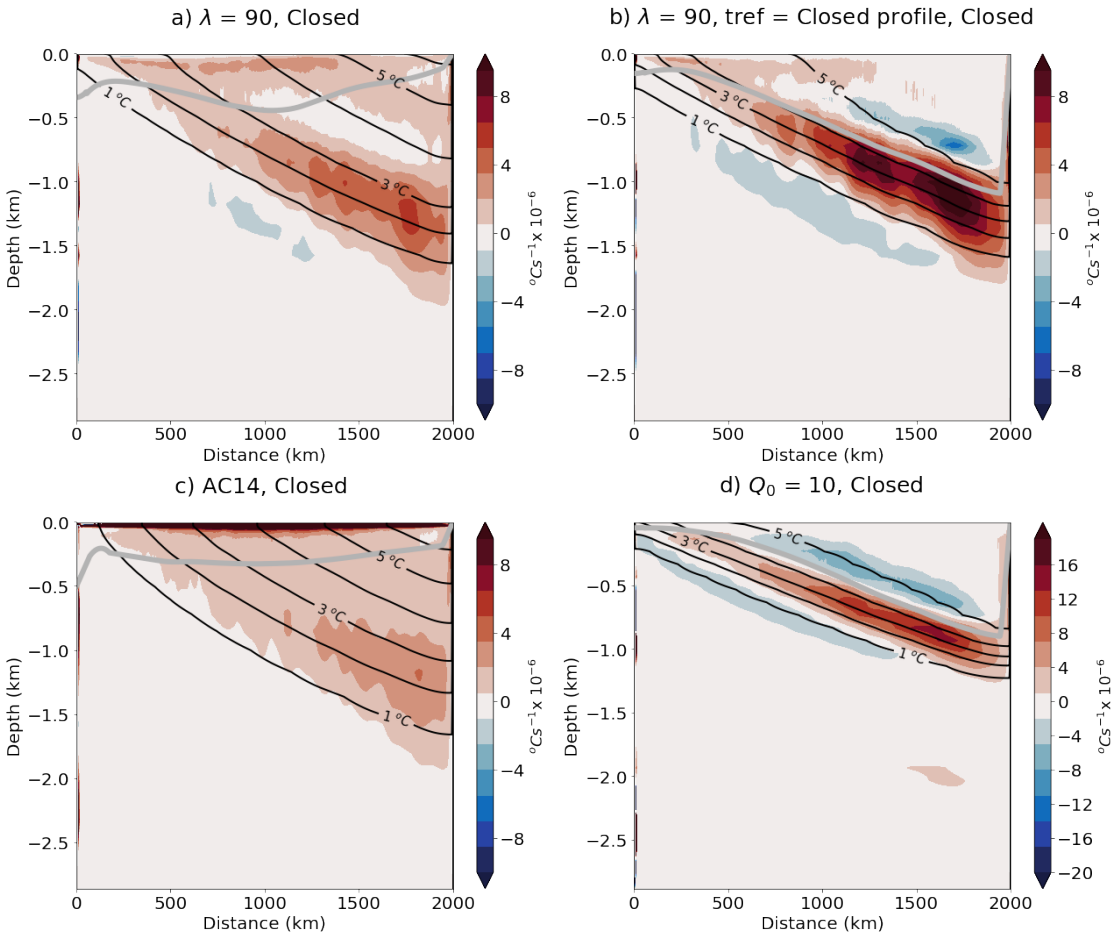

Figure 3.20: Zonal mean advective heat flux divergence for various surface heat forcing scenarios with closed northern boundary. a) Surface restoring, b) Surface restoring with closed restoration profile c) AC14 surface restoring and d) fixed surface fluxes.

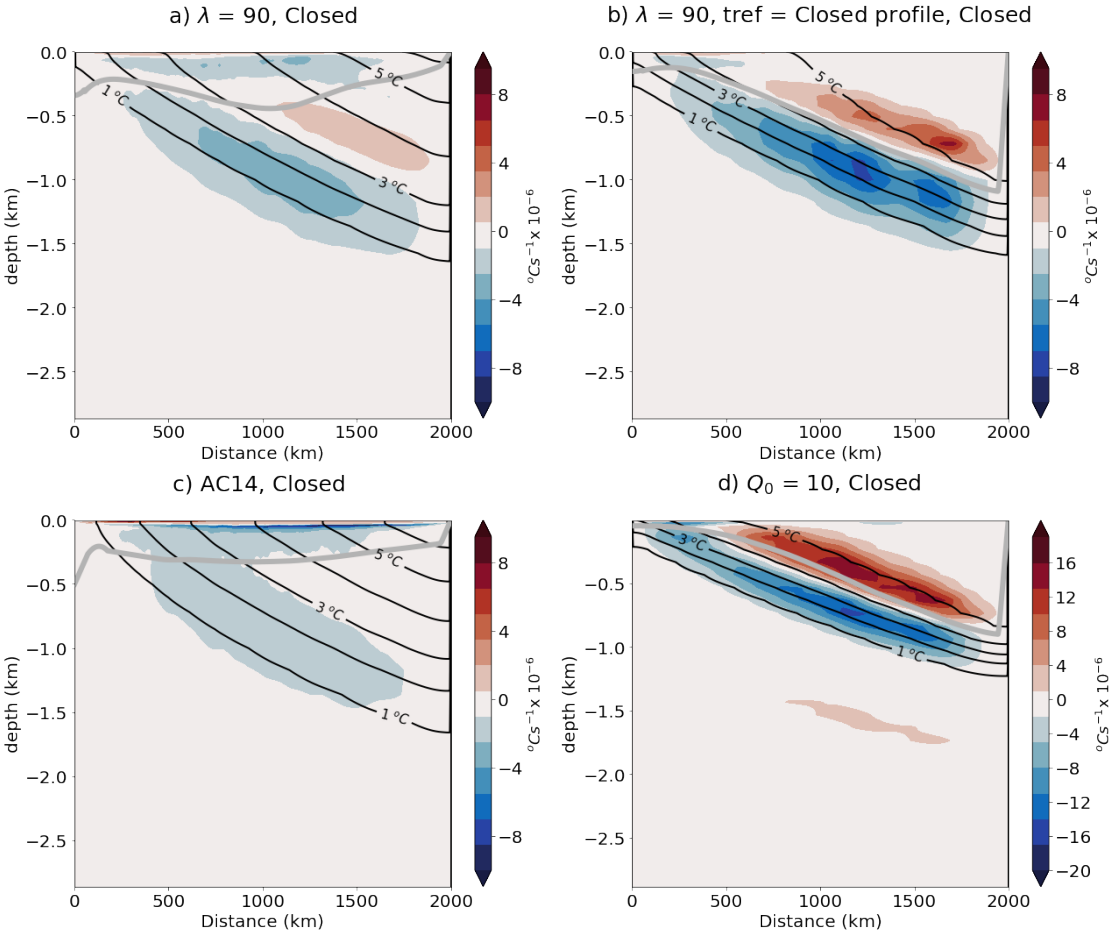

Figure 3.21: Zonal mean diapycnal eddy heat flux divergence (D) for various surface heat forcing scenarios with closed northern boundary. a) Surface restoring, b) Surface restoring with closed restoration profile c) AC14 surface restoring and d) fixed surface fluxes.

This pattern is further illustrated when examining the diabatic eddy heat flux divergence in Fig. 3.21. A clear transition from Fig. 3.21.c to Fig. 3.21.a to Fig. 3.21.b to the fixed flux scenario Fig. 3.21.d can be seen. With the emergence of a strengthening convergence/ divergence dipole with weakening meridional temperature gradient and a deepening of the surface mixed layer.

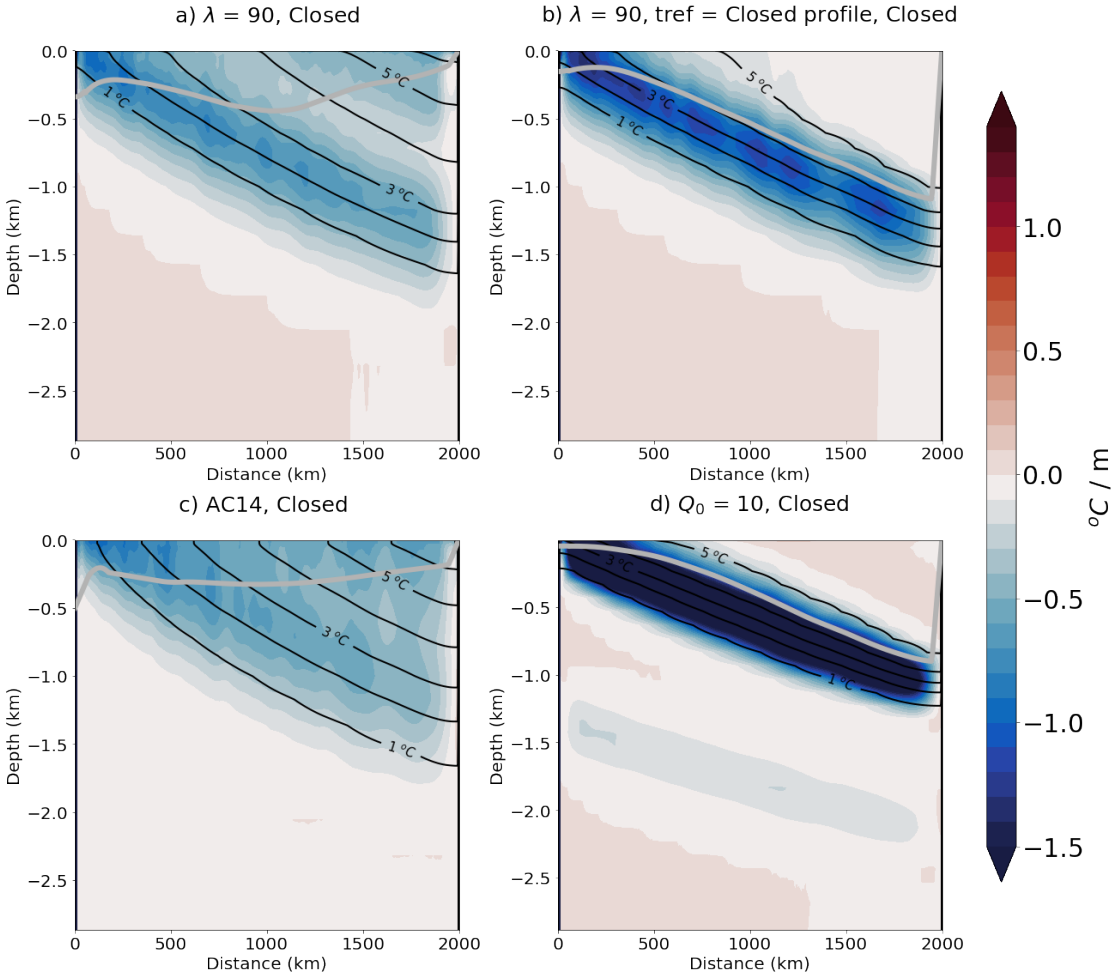

Figure 3.22: Meridional temperature gradient for various surface heat forcing scenarios with closed northern boundary. a) Surface restoring, b) Surface restoring with closed restoration profile c) AC14 surface restoring and d) fixed surface fluxes.

For reference we plot the zonal mean meridional temperature gradient in Fig. 3.22. As shown by the temperature contours where we get an intense surface overturning we have consistent strong meridional temperature gradient Fig. 3.22.c where strong southward eddy heat fluxes dominate. The gradient is much less constant Fig. 3.22.a allowing for a reduction in that intense surface cell. When the SO ROC collapses with a closed northern boundary there is weak surface meridional temperature gradients in the north of the domain Fig. 3.22.b and Fig. 3.22.d. These results demonstrate the complex nature we would expect from a coupled system. The perfect dipole in the diabatic eddy heat could arise from either fixed fluxes or surface restoring but only with certain caveats. We can see that in all cases the

SO ROC is altered dramatically when the northern boundary is closed.

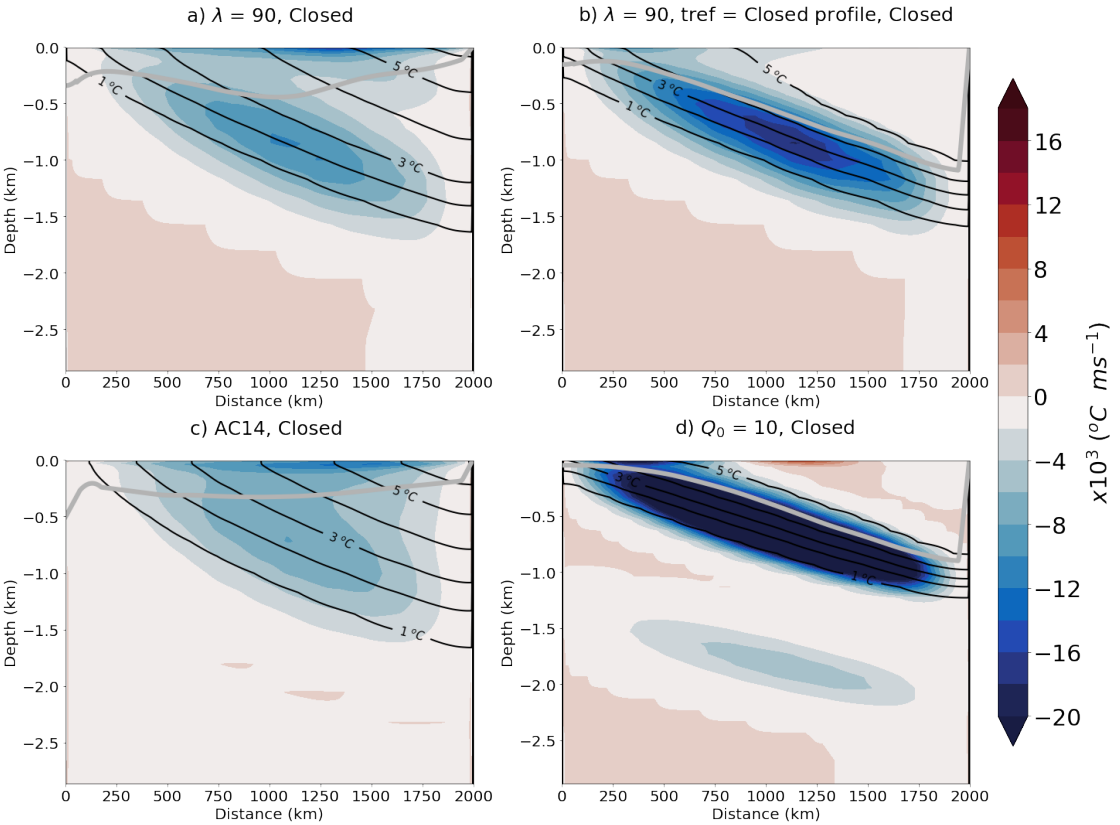

Figure 3.23: Meridional eddy heat fluxes for various surface heat forcing scenarios with closed northern boundary. a) Surface restoring, b) Surface restoring with closed restoration profile c) AC14 surface restoring and d) fixed surface fluxes.

Chapter 4

Varying the Northern Boundary Stratification

The previous chapters have shown the role of diabatic eddies in responding to closing the northern boundary. In our initial experiments altering τ_r, the relaxation time scale, the domain stratification was dramatically altered. A natural extension to this is to alter the stratification profile of the sponge layer by altering the e-folding depth scale N in Eq. (1.54). Although some gradual changes can be seen with increasing relaxation timescale, the collapse of the SO ROC is more of a stepped response between turning on or off the sponge layer when using relaxation timescale as the variable, to assess if this would truly be a stepped response, we now directly altering the stratification to see how the SO ROC responds. This may also assist to investigate if there is any form of proportionality in that response relating to T_N (the sponge layer stratification). It should be stressed that as an idealised modelling study these will just be approximate proportionality merely forming a guide for consideration of consequences for altering boundary conditions. This study could act as a guide to further studies to narrow down a parameterisation once more complex factors are included in model runs, such as a coupled atmosphere and variations in salinity. Chapter 2 showed us that changing stratification

at the northern boundary can lead to increased diabatic eddy heat fluxes from increase diabatic layer depth, EKE and EPE. Those experiments used changing diabatic sponge layer forcing to alter the effective buoyancy forcing through surface diapycnal eddies. Although this allowed us to gain insight into what factors might control diabatic eddies and their role in setting the SO ROC in idealised models these experiments did not allow us to establish a direct relationship between stratification and diabatic eddy heat fluxes. These findings prompted us to investigate further the link between northern boundary stratification and diabatic eddy heat flux modulation of the effective buoyancy forcing. Establishing how diabatic eddies will respond to altered northern boundary conditions may be important for setting up a channel or southern hemispheric models; where the effective buoyancy forcing may be partly determined by the northern boundary condition before the surface parameters are altered. Understanding the response of diabatic eddies to changing background ocean stratification could also be useful for parametrisations in climate models and understanding the Southern Ocean response in high-resolution climate models.

4.1 Set Up

Once again we base the model set up on the set up described in section 1.5 (Fig. 2.1), but we now directly alter the northern boundary stratification to establish a relationship with stratification. The channel domain is 1000 km by 2000 km and 3000 m deep with an eddy-resolving horizontal resolution of 5 km with 30 geopotential layers, ranging in thickness from 5 m at the surface to 260 m at the bottom. Surface forcing remains the same as outline in section 1.5.

For the standard run the northernmost 100 km of the domain is a full depth sponge layer to relax the northern boundary temperature (T^*) profile to a prescribed tem-

perature profile (Eq. (1.54)):

$$T^*(z) = \Delta T \frac{(e^{z/N_d} - e^{-H/N_d})}{1 - e^{-H/N_d}},$$

assuming a natural stratification depth of $N_d = 1000$m and a temperature difference (ΔT) of 8 °C.

We then directly alter the northern boundary stratification by altering N_d in Eq. 1.54 from $N_d = 50$ m to $N_d = 10000$ m.

Another way to directly alter the northern boundary stratification is by altering ΔT, the top to bottom temperature difference.

4.2 Preliminary Experiments

We ran a series of experiments varying N from 50 m to 10000 m, which generates the temperature profiles shown in Fig. 4.1.

Fig. 4.2 shows the SO ROC when these new stratifications are applied. The natural stratification of 1000m used in previous experiments Fig. 4.2.e shows the 3 cell SO ROC we are familiar with and increasing N_d depth weakens the SO ROC as isotherms appear to flatten slightly Fig. 4.2. When the e-folding length $N_d$is reduced we see a steepening of the isotherms in the south of the domain and a shallowing of the isotherms in the upper north of the domain. This leads to a large increase in the lowermost baroclinic instability driven overturning cell Fig. 4.2.a-c. However, the steep isotherms and 'bumpy' nature of this overturning appears somewhat unstable as the isotherms become almost vertical in the south of Fig. 4.2. Fig. 4.2. A full depth diabatic layer [1] in the south of the domain. Fig. 4.2.f-h have unventilated isotherms alongside oscillating domain EKE which leads to some behaviour that suggests the model has not reached equilibrium.

[1]For speed in the calculation the mixed layer depth plotted for these figures only is simply the MITgcm output mixed layer depth, which gives an approximation.

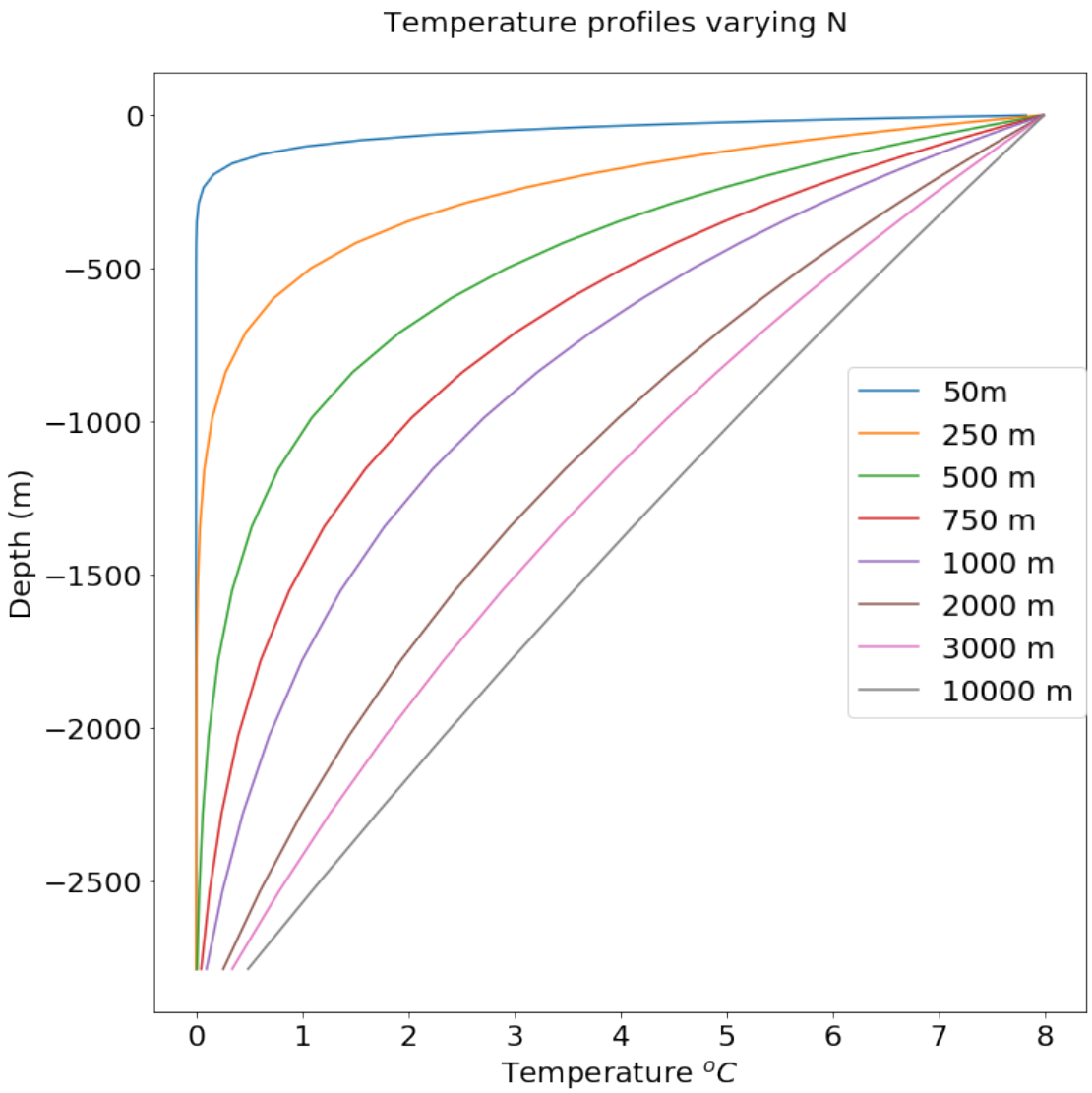

Figure 4.1: Sponge layer temperature profiles altering N_d in Eq. (1.54).

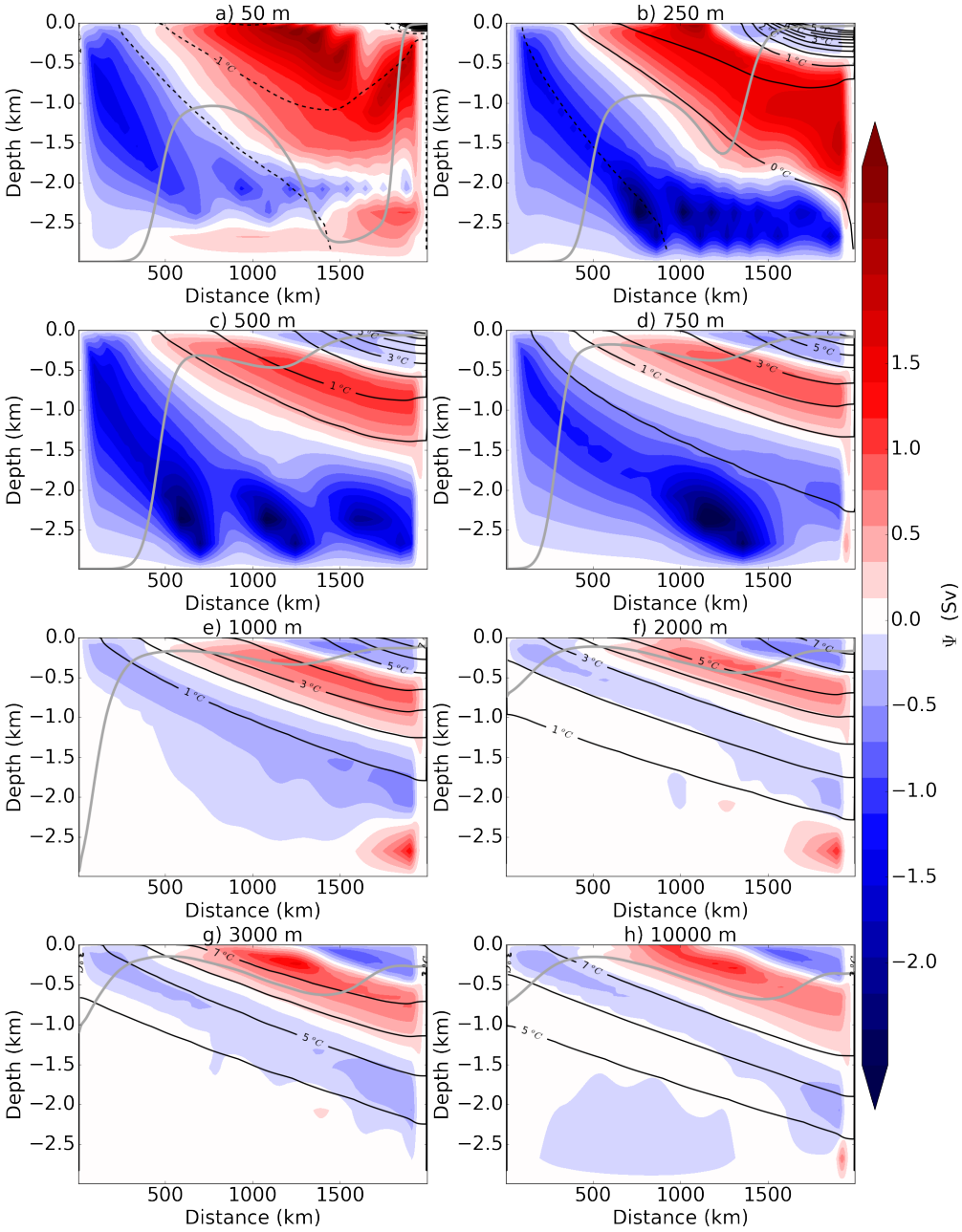

Figure 4.2: The isothermal stream function $\Psi_{res}(y, \theta)$ remapped onto depth coordinates, to give $\Psi_{res}(y, z)$ for various values of N_d in the sponge layer relaxation profile. Isotherms in multiples of 1°C are overlaid as solid black contours. (Preliminary experiment.)

4.3 Direct Alteration of Northern Boundary Stratification

As with Fig. 2.5 the preliminary experiments show that mismatching diabatic forcing between the sponge layer and the surface can lead to unstable solutions. Both unventilated isotherms and surface isotherms that did not exist in the sponge layer were created. This meant we had to alter Eq. (1.54) to give a more compatible profile.

$$T^*(z) = \Delta T \frac{(e^{z/N_d} - e^{-H/N_d})}{1 - e^{-H/N_d}} + 2\left(\frac{N_d - N_{d0}}{N_{d0}}\right), \tag{4.1}$$

with $N_0 = 1000$m and setting N_d max as H for the adjustment term, after which temperature profile is linear. ΔT is given by:

$$\Delta T = \Delta T_0 - \left(\frac{N_d - N_{d0}}{N_{d0}}\right). \tag{4.2}$$

Where $\Delta T_0 = 8°$C. This gives us the new temperature profiles in Fig. 4.3. The maximums and minimums of these profiles are now a match with the southern surface minimums and surface maximums seen in the preliminary experiments. The most extreme cases $N_d = 50$ m and $N_d \geq 3000$ m required a further degree of adjustment in order to remove unventilated isotherms and or cold water that is never seen at the northern boundary; we do not show these runs here as they proved to be impracticable stratifications profiles.

The focus on stratification leads us to run an additional two experiments halving and doubling the temperature range (ΔT) in eq. Eq. (4.3) with an adjustment to prevent unstable circulation:

$$T^*(z) = \Delta T \frac{(e^{z/N_d} - e^{-H/N_d})}{1 - e^{-H/N_d}} + 2\left(\frac{\Delta T - \Delta T_0}{\Delta T_0}\right), \tag{4.3}$$

where ΔT_0 is again 8 ^{o}C. Again the maximums and minimums of these profiles are a match with the southern surface minimums and surface maximums seen in the preliminary experiments. The profiles are shown in Fig. 4.3b). All experiments were relaxed with a 3-day relaxation timescale.

To ascertain the direct link between stratification at the northern boundary and the SO ROC we ran a series of experiments altering $T^*(z)$ by varying N_d (50m, 250m, 500m, 750m, 1000m, 2000m and 3000m). Here for clarity we focus on 4 runs varying N_d and 3 runs varying ΔT with the altered temperature profiles shown in figure Fig. 4.3.a, which vary from a shallow sharp thermocline to a linear stratification profile.

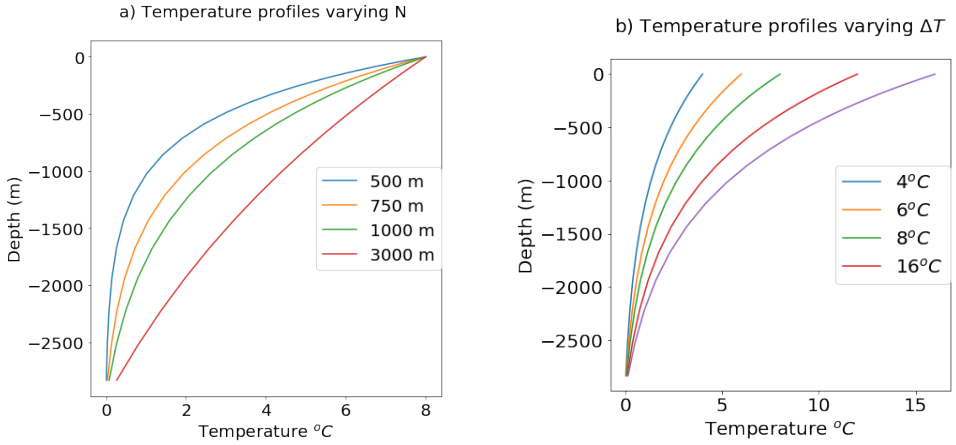

Figure 4.3: New temperature profiles for Sponge layer relaxation for update equations a)Varying N_d (Eq. (4.1)) and b) Varying ΔT (Eq. (4.3)).

4.4 Overturning Response

Varying N

Again the Eulerian mean overturning remains constant at around 2.25 Sv (not shown here). We calculate the isothermal streamfunction following Eq. (2.11) for

N_d = 500, 750, 1000, 3000 m to demonstrate the effect of directly altering the northern boundary stratification.

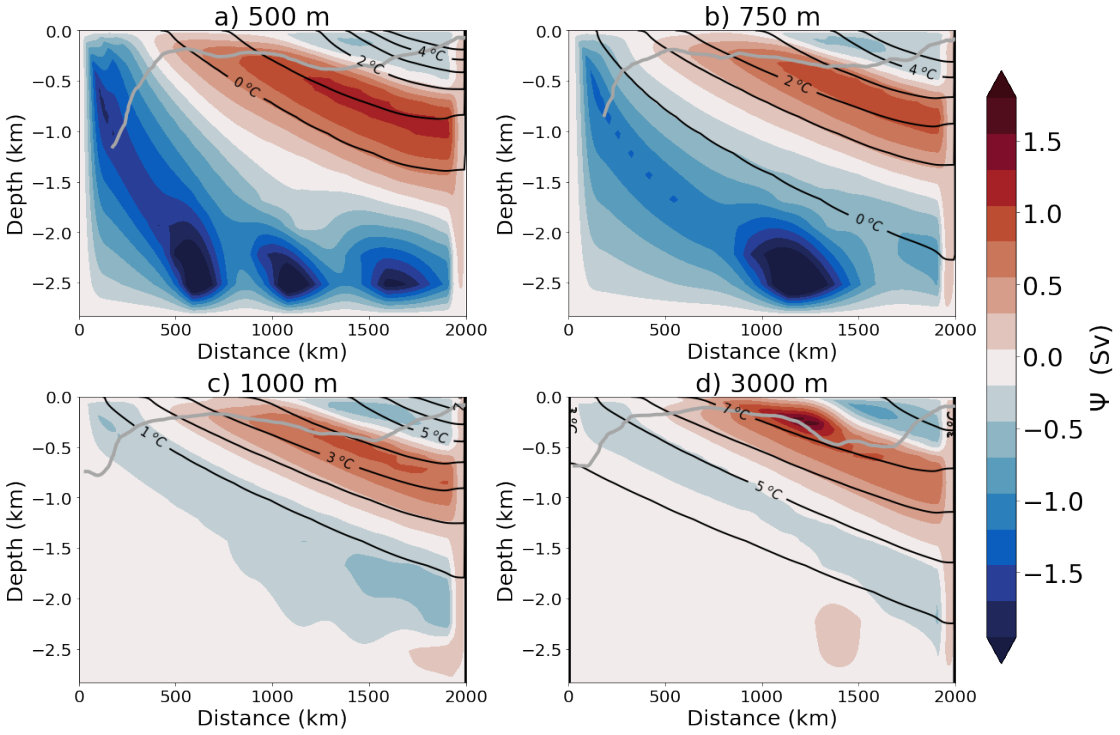

Figure 4.4: The isothermal stream function $\Psi_{res}(y, \theta)$ remapped onto depth coordinates, to give $\Psi_{res}(y, z)$ for a) $N_d = 500$ m b) $N_d = 750$ m, c) $N_d = 1000$m and d)$N_d = 3000$m. Isotherms in multiples of 1°C are overlaid as solid black contours.

Fig. 4.4 shows the SO ROC when these new stratifications are applied. The natural stratification of 1000m used in previous experiments Fig. 4.4.c shows the 3 cell SO ROC we are familiar with. Increasing N_d depth weakens the SO ROC as isotherms appear to flatten slightly Fig. 4.4.d . When N is reduced isotherms steepen, particularly in the South of the domain. This leads to a large increase in the lower-most baroclinic instability driven overturning cell Fig. 4.4.a-b. The clockwise mid-depth cell also intensifies as N is reduced in Fig. 4.4. In general, we note decreasing N strengthens the SO ROC, however, in the absence of any abyssal stratification the lowermost cell appears to strengthen disproportionally. It is worth briefly speculating here that the role of topography would likely alter the response of the lowermost cell (*Abernathey and Cessi*, 2014) (discussed in next chapter). There is little effect on the surface mixed layer depth, varying only weakly in areas

of much reduced stratification.

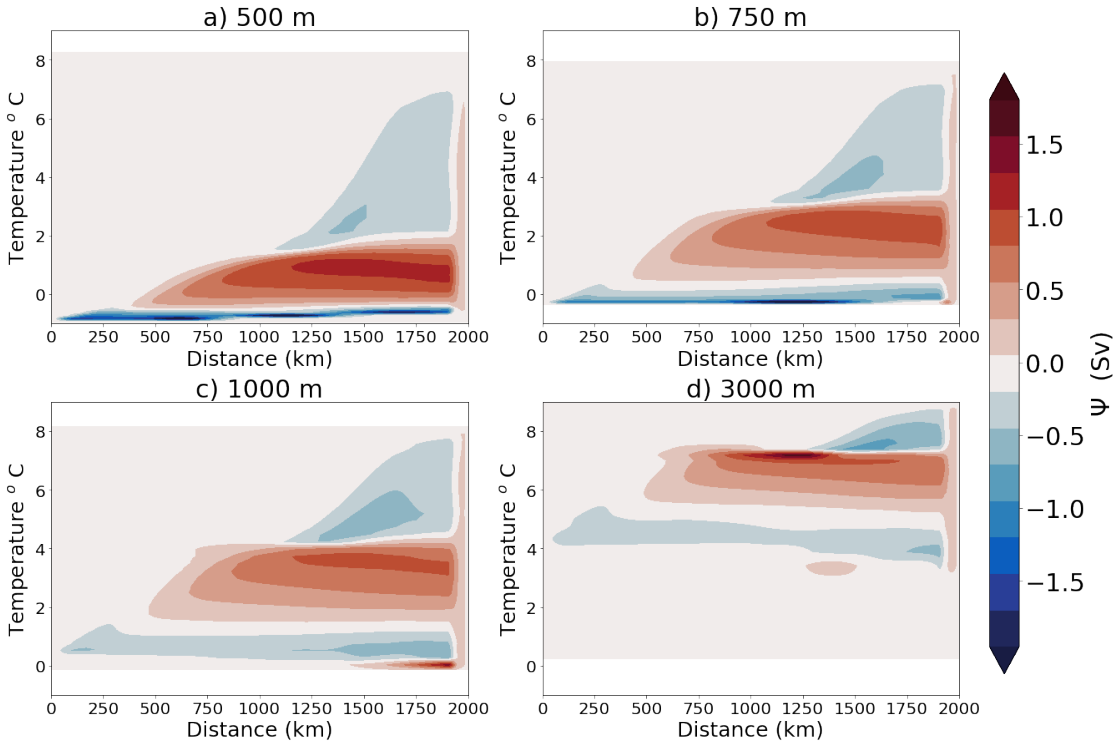

Figure 4.5: The isothermal stream function $\Psi_{res}(y, \theta)$ for a) $N_d = 500$ m b) $N_d = 750$ m, c) $N_d = 1000$m and d)$N_d = 3000$m.

The changes to the SO ROC are highlighted in temperature space in Fig. 4.5, where the clock wise cell distinctly weakens with Fig. 4.5.d approaching the circulation seen at higher sponge relaxation time scales ($\tau_R = 1000+$ days) seen in chapter 2. The SO ROC in temperature space also gives a much clearer picture of the diminishing lowermost cell and the increasing uppermost cell with increasing N_d. This suggests a large shift in baroclinic stability with changing stratification altering the eddy compensation in the channel.

Varying ΔT

The Eulerian mean overturning remains nearly unchanged, but we note a slight deviation when the top bottom temperature difference is doubled. Fig. 4.6 shows that the maxima of overturning remains at ≈ 2.25 Sv but, the pattern of strongest forcing in the centre is disrupted slightly, most likely due to Reynolds stress. Unlike,

many of our experiments we also see and increase in mean kinetic energy for this run as well. This might arise from the dramatic flattening in isotherms and increase in stratification seen in this run.

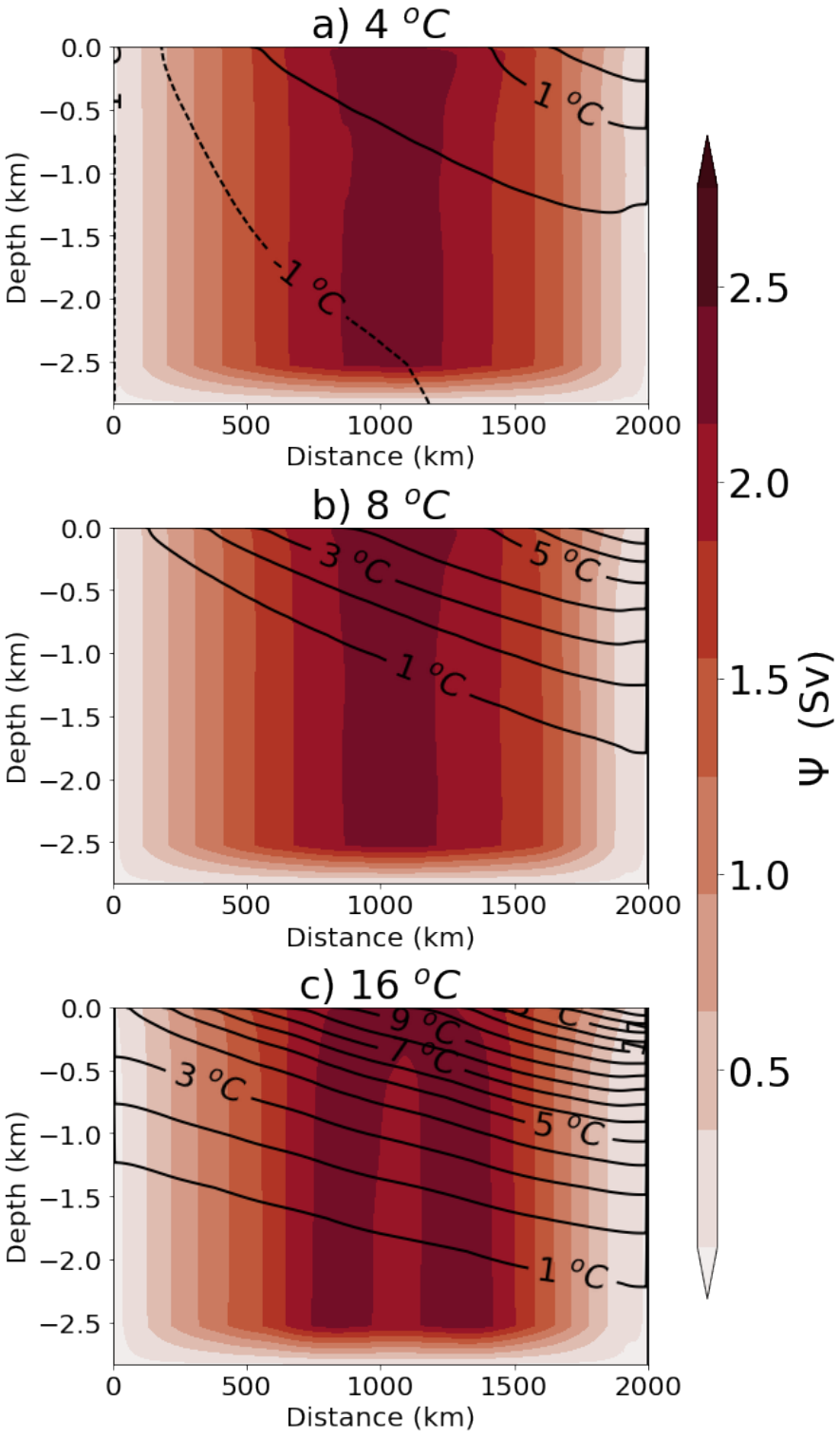

Figure 4.6: Eulerian overturning ($\overline{\Psi}$) for various values of ΔT. Isotherms in multiples of 1°C are overlaid as solid black contours.

We also see large changes to the SO ROC in response to altering the top to bottom stratification. This is best shown in temperature space in Fig. 4.7, a more condensed top to bottom temperature range (4^oC) gives rise to a stronger SO ROC and increasing the top to bottom temperature range (16^oC gives the opposite effect weakening the SO ROC. Fig. 4.7.c forces flatter isopycnals and stratification at depth preventing the lowermost cell from forming (in the absence of topography). As the varying N_d in Fig. 4.5 increasing ΔT leads to shallower isopycnals and weaker SO ROC.

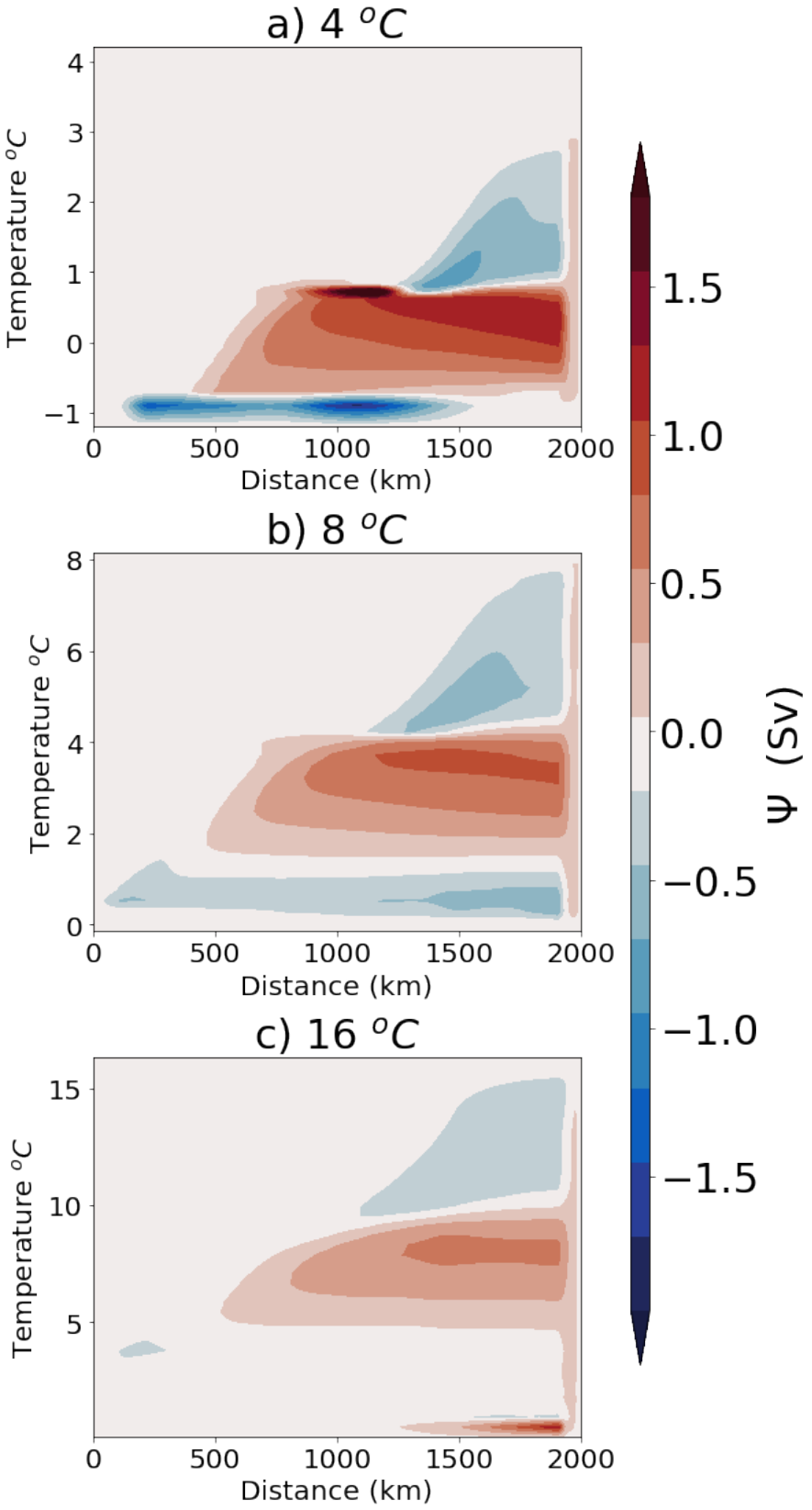

Figure 4.7: The isothermal stream function $\Psi_{res}(y, \theta)$. For various values of ΔT.

Heat Budget

Once again we evaluate the heat budget using equation Eq. (2.5):

$$\underbrace{\frac{\partial \overline{v}\overline{T}}{\partial y} + \frac{\partial \overline{w}\overline{T}}{\partial z} + \frac{\partial \overline{v'T'}S_T}{\partial z} + \frac{\partial \overline{v'T'}}{\partial y}}_{\text{advective } (\nabla \cdot \overline{\mathbf{u_A}T})} = \underbrace{\frac{\partial Q}{\partial z}}_{\text{air-sea fluxes}} - \underbrace{\frac{\partial \left(\overline{w'T'} - \overline{v'T'}S_T\right)}{\partial z}}_{\text{Diapycnal eddies}} = \frac{\partial (Q - D)}{\partial z},$$

Plotting the L.H.S terms in black as the advective heat divergence and the R.H.S in blue and red for the diapycnal eddy heat flux divergence terms and the surface heat fluxes respectively. Fig. 4.8 shows a simple scenario of the heat flux divergences reducing with increasing N_d, with Fig. 4.8.d ($N_d = 3000$m) having half the maxima of Fig. 4.8.a ($N_d = 500$m). Increasing N_d leads to smaller temperature gradients and shallower isopycnals giving smaller heat flux divergence/convergence terms.

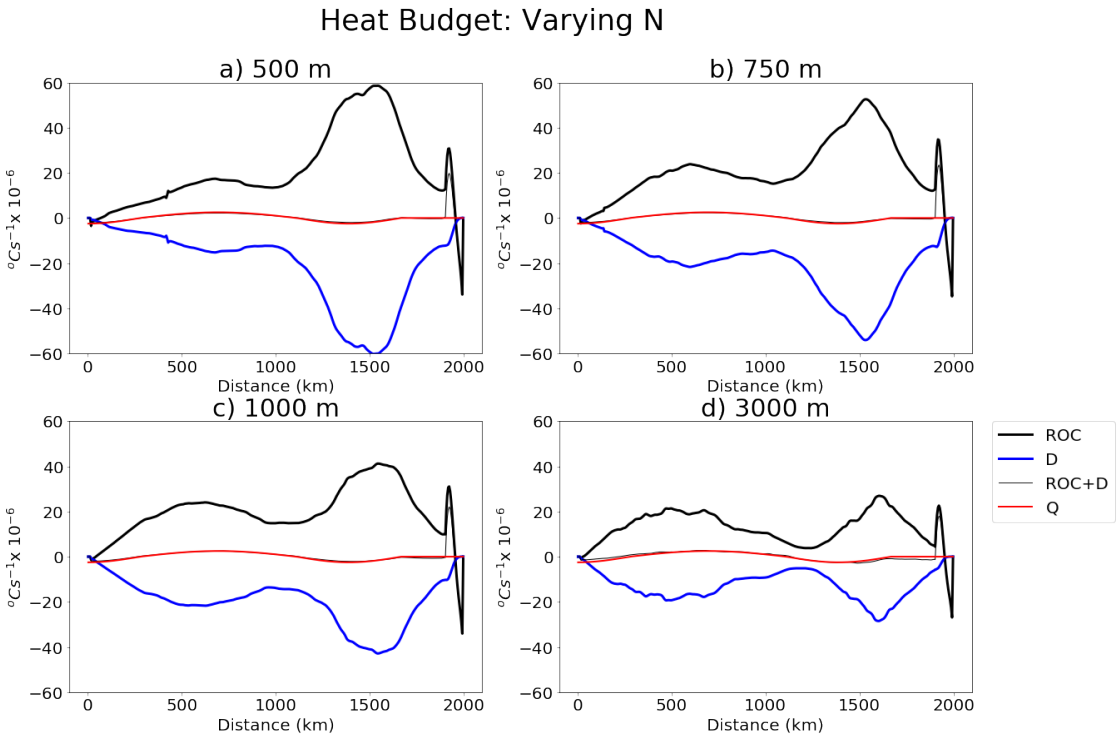

Figure 4.8: The components of the full depth buoyancy budget evaluated in as in Eq. 2.5 for altered sponge layer stratification varying with N_d. The advective transport component is show in black and diapycnal transport in blue, surface heat forcing in red and the total in thin black line.

This simple story is backed up by plotting the diabatic eddy heat flux divergence term in depth space. Fig. 4.9 shows the diabatic eddy heat flux divergence terms

reducing in magnitude with increasing N_d. Showing the SO ROC can diminish not only through a spatial distribution change in the diabatic eddy heat flux divergence but in a reduction of the fluxes in response to altered northern boundary stratification. With the SO ROC weakening we do not see an increased mixed layer forming or any sign of a diapycnal eddy heat flux dipole emerging, this is also the case in our surface restoring experiments where the SO ROC collapses with out a deep mixed layer or diapycnal heat flux dipole.

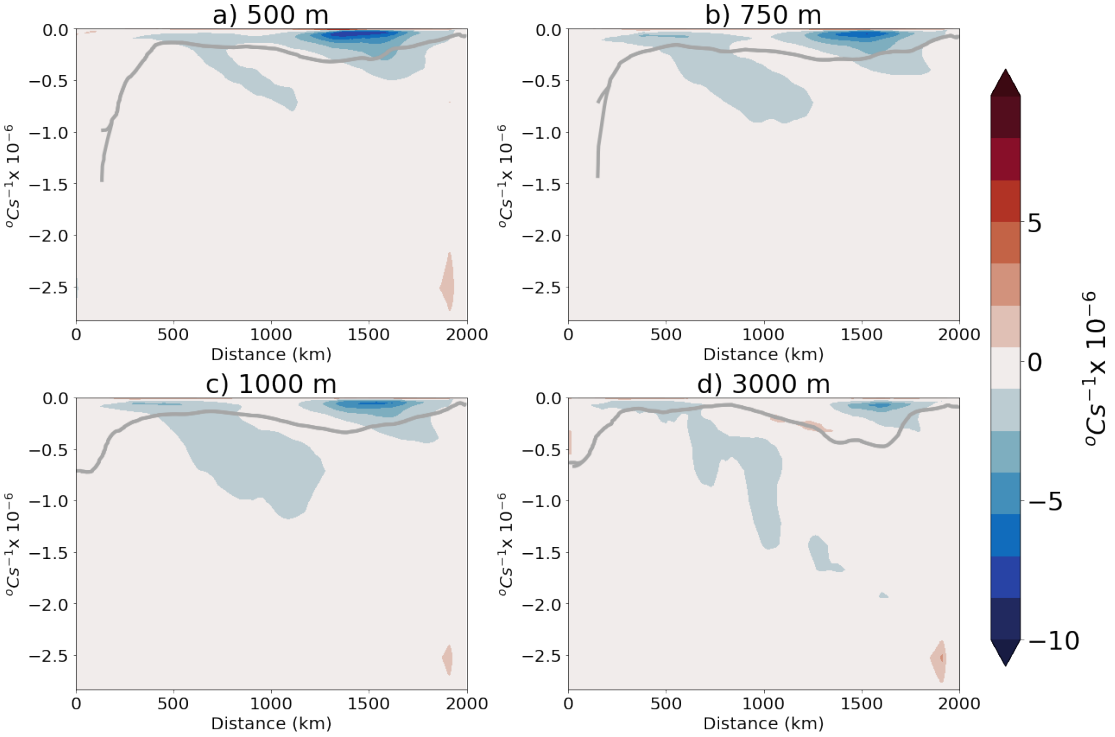

Figure 4.9: Zonal mean diapycnal eddy heat flux divergence (D) for altered sponge layer stratification varying with N_d.

Varying ΔT

As with varying N_d, altering the top to bottom temperature difference shows a simple scenario of the heat flux divergences increasing with increasing temperature difference, with Fig. 4.10.a having a third of the maxima of Fig. 4.10.c. However, when N_d is increased the heat flux divergence magnitude is reduced leading to a reduction in SO ROC strength, which is the opposite to Fig. 4.10 but more like our fixed flux experiments.

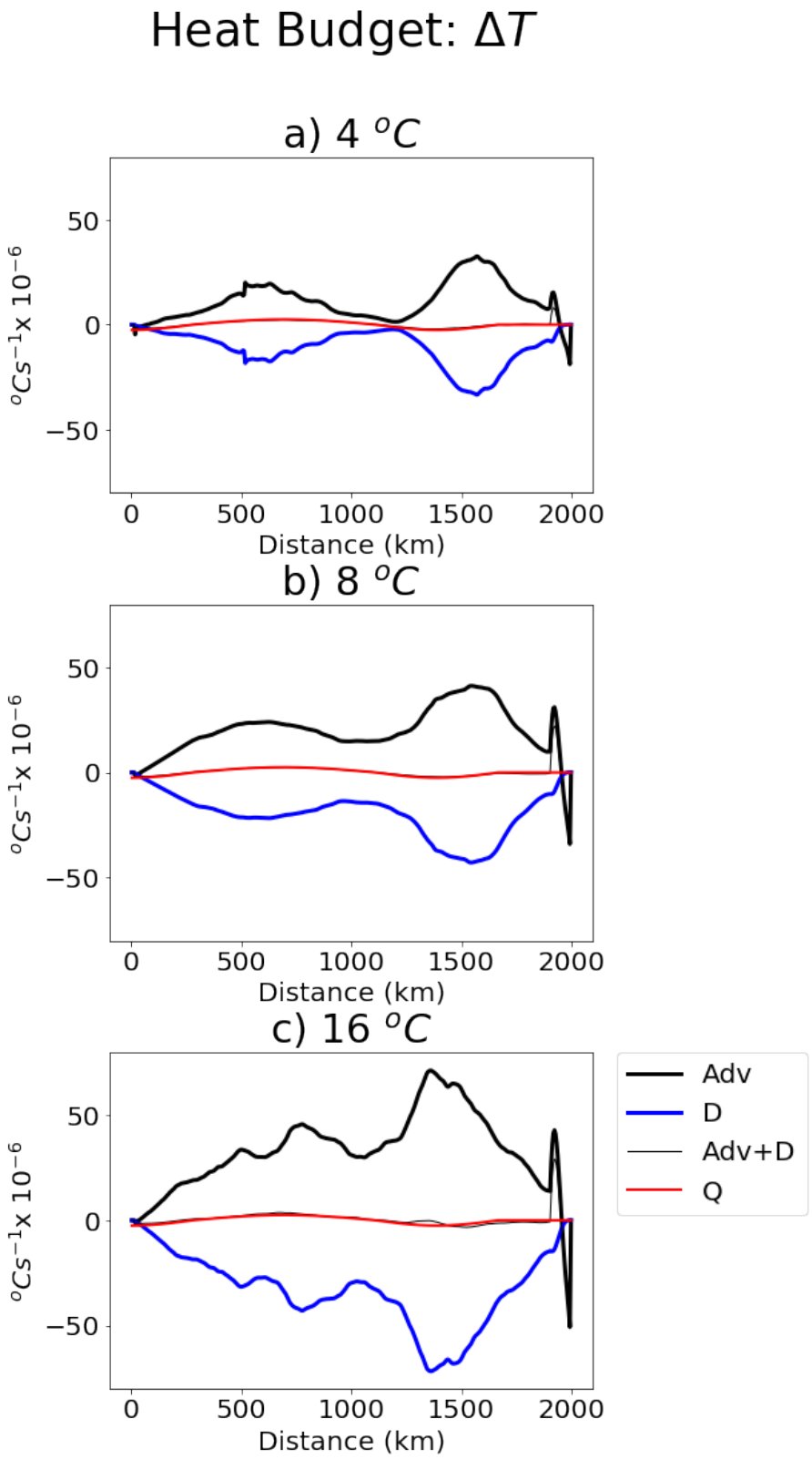

Figure 4.10: The components of the full depth buoyancy budget evaluated in as in Eq. 2.5 for altered sponge layer top-to-bottom temperature difference (ΔT). The advective transport component is show in black and diapycnal transport in blue, surface heat forcing in red and the total in thin black line.

There is a uniform increase in strength of diabatic eddy heat flux divergence when plotted in depth space in Fig. 4.11. Not only the maxima of heat flux divergence increase with increasing ΔT but we also see a much larger area of influence in Fig. 4.11.c. Indicating a deeper influence of diabatic eddies in redistributing heat, this suggests that not only are the magnitude of the diabatic eddy heat fluxes important but their extent of area over which they act.

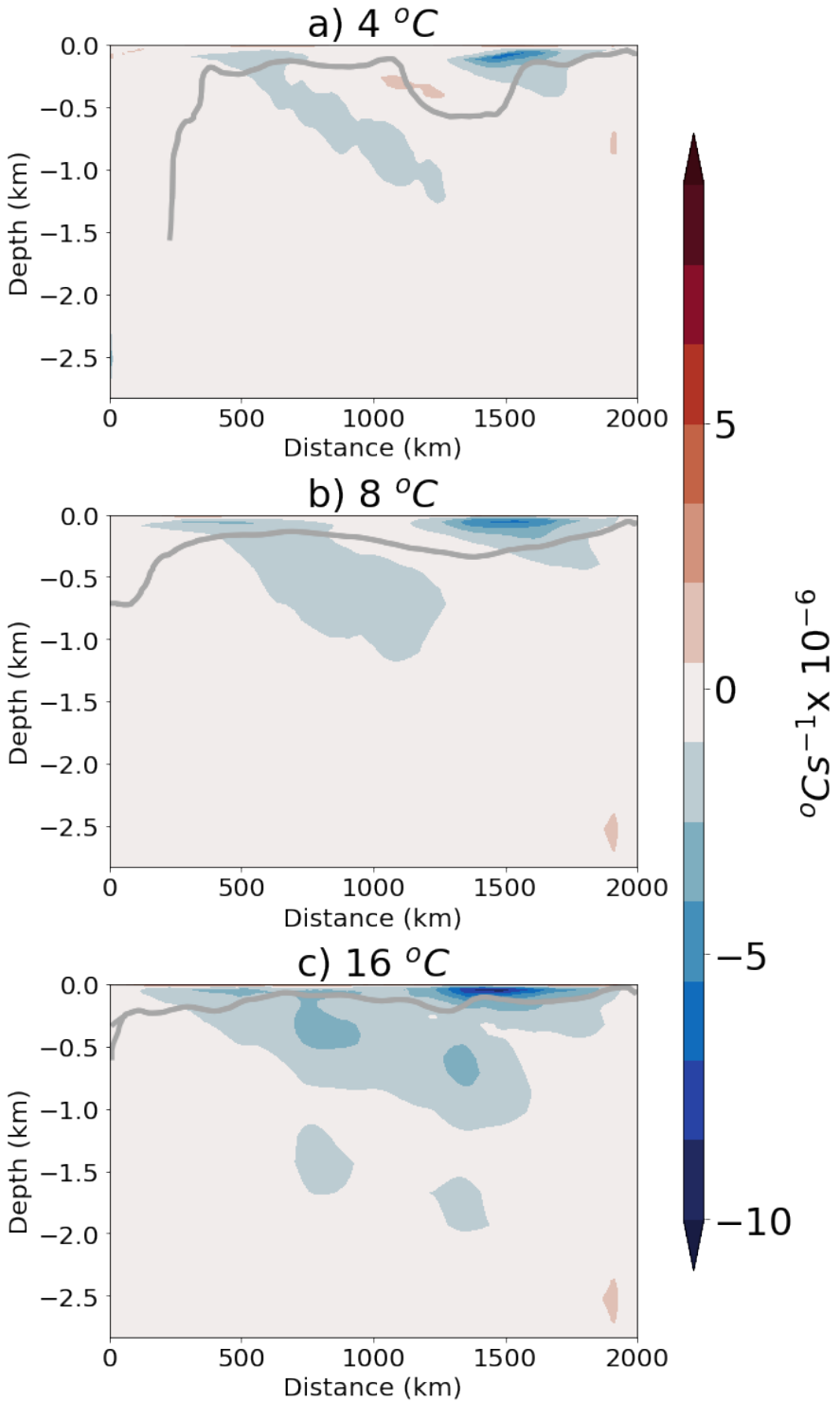

Figure 4.11: Zonal mean diabatic eddy heat flux divergence (D) for altered sponge layer top-to-bottom temperature differences (ΔT).

4.4.1 Energetics

Varying N_d

As we might suspect due to the change in isopycnal slope and decreasing stratification with increasing N_d. EKE maxima steadily decreases with increasing N_d in Fig. 4.12, however when considering the domain integrated EKE we see a steady increase as EKE is enhanced over a larger area with increasing N_d

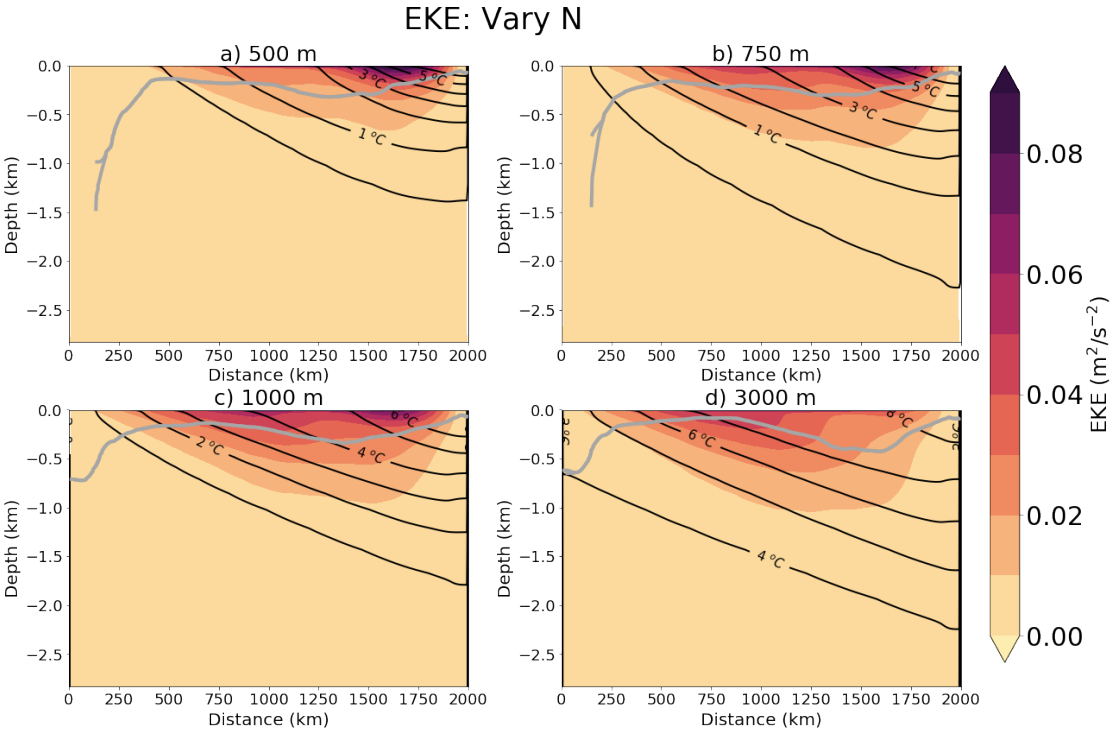

Figure 4.12: Zonal mean EKE, for altered sponge layer stratification varying with N_d.

This contributes to the decreasing diabatic eddy heat flux divergence and the decreasing SO ROC strength when increasing N_d. Although we note a very small increase in Mean Kinetic Energy (not shown here) leading to a smaller decrease in domain total Kinetic Energy.

Varying ΔT

The increasing diabatic eddy heat flux divergence also corresponds to a 5 fold increase in EKE between 4^oC and 16^oC. We note here there is a doubling in the maximum Mean Kinetic Energy (not shown here) leading to a slightly larger increase in domain total Kinetic Energy than the increase from EKE alone.

4.5 Conclusions for Altered Northern Stratification

Varying the northern boundary appears to have clear consequences for eddy energetics and the SO ROC, which could promise an interesting direction for further research. What stratification with short relaxation time scales could lead to a full collapse of the SO ROC, i.e. is it possible to cancel the effective buoyancy forcing though choice of sponge layer and surface heat forcing. We saw in chapter 2 that you can not simply use the profile from the closed scenario with the same forcing. The systematic weakening of the SO ROC with increasing N_d suggests that there is a possible northern boundary stratification that could be combined with differing surface forcing to collapse the SO ROC without turning off the sponge layer, the diabatic heat fluxes seen in this chapter also suggest that perhaps the strong dipole and deep mixed layer seen in chapter 2 are not required to weaken the SO ROC. The choice of boundary conditions affects the dynamics even when the same ultimate result is achieved, e.g. we see that increasing EKE does not always mean decreasing SO ROC strength. This would mean differing combinations of surface heat and freshwater fluxes could moderate the SO ROC response to altered northern boundary conditions through altering the response in the diabatic eddy heat fluxes. The idea that stratification plays a role in setting the overturning in the Southern Ocean is not a new one, this has been discussed at great length in numerous studies such as *Ferreira et al.* (2005), where it is pointed out there

must be a dependence on N^2 for eddy diffusivity as rationalised in in *McWilliams and Danabasoglu* (2002) using the mixing length hypothesis (*Visbeck et al.*, 1997). *Abernathey et al.* (2011) finds that eddy diffusivity is proportional to EKE so we would expect to see an increase in EKE with increasing N^2. Here we see large changes in altering stratification, i.e. increasing northern boundary stratification leading to increased EKE and increase diapycnal eddy heat flux divergence. For example examining our ΔT = 16 ^{o}C and our N_d = 500 m experiments, for N_d = 500 m where there is a large increase in N^2 in the upper northern part of the domain we see the SO ROC diminish (Fig. 4.4.a) but deeper and further south N^2 decreases as do EKE and diapycnal eddy heat flux divergence terms, here there is a stronger SO ROC, whereas in our ΔT = 16 ^{o}C, N^2 remains high throughout the domain and we see that reflected in higher domain-wide EKE, and a wholly diminished SO ROC. The domain N^2 is set by the northern boundary stratification and shows the impact of this choice of boundary condition in setting influencing domain-wide dynamics before considering altering any other model parameters.

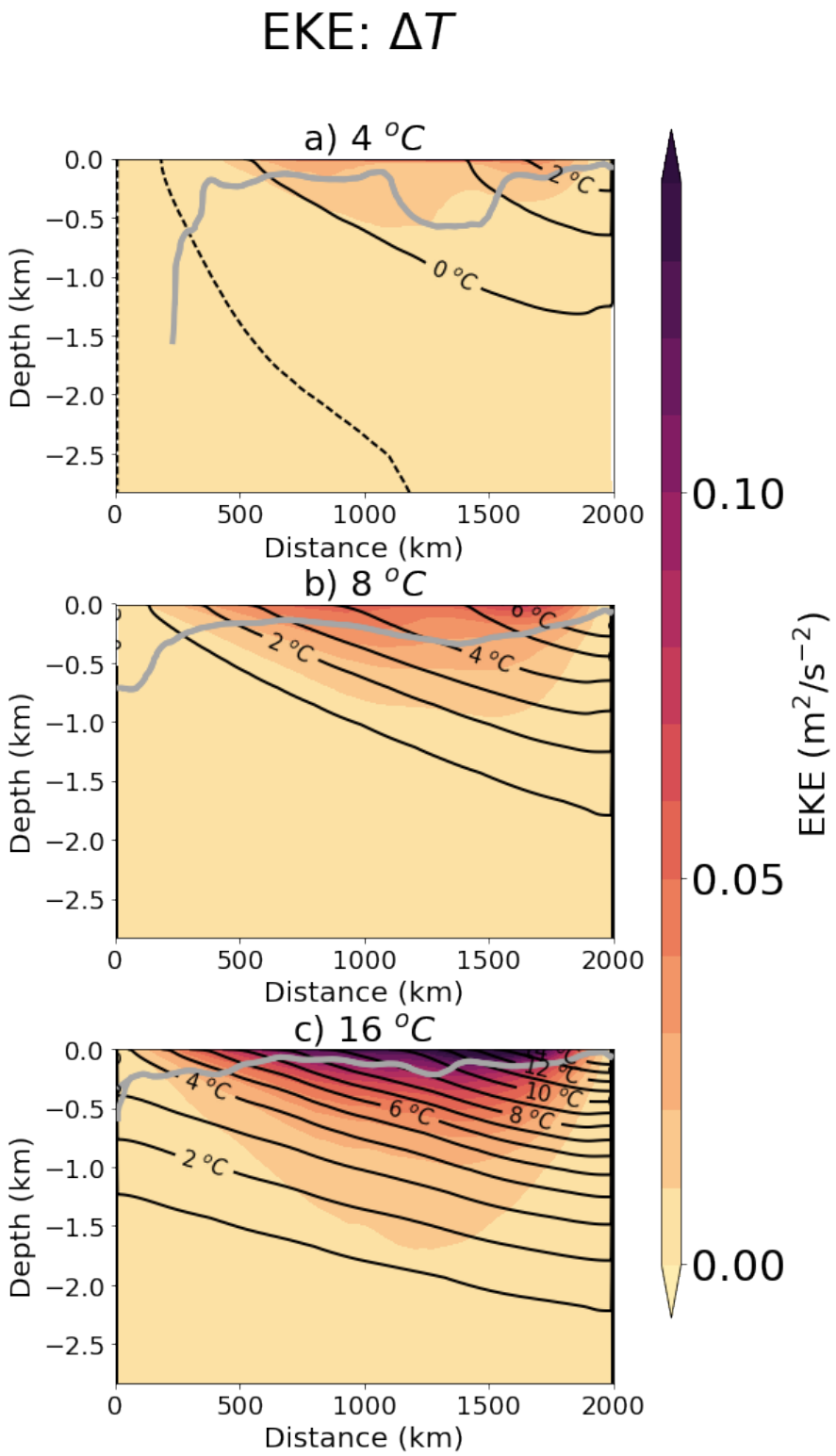

Figure 4.13: Zonal mean EKE altered sponge layer top-to-bottom temperature difference (ΔT).

Chapter 5

Other Considerations

One of the major considerations we have neglected thus far is the influence of topography on the response of the ACC. Although beyond the scope of this thesis to fully address the role of topography in moderating the SO ROC response to altered boundary conditions in a channel model, we can include additional runs to validate and question our conclusions drawn thus far. In this short chapter, we show the results of experiments including topography and discuss how this differs from flat bottom runs in the previous chapters. We will also discuss eddy saturation in our experiments.

5.1 Including Topography

In the real ocean, the wind stress applied to the surface of the ocean is balanced by bottom stresses and topography plays a leading order role in setting the spatial variability of the eddy field (*Thompson*, 2008) as well as the efficiency of eddy dynamics *Abernathey and Cessi* (2014). The Southern Ocean has areas of rough topography, notably the Kerguelen Plateau and the Macquarie Ridge play large roles in setting the steering of the ACC, enhancing EKE and eddy mixing. As topography plays an important role in Southern Ocean dynamics it is important to

consider what qualitative impacts it may have in our idealised setup and results.

5.1.1 Set Up

To investigate the effect of topography on our experiments we devised a further set of model runs. The model is once again based on the set up described in section 1.5 and we give a brief overview of the exact set up used here. Topography generates meanders in the ACC and to this end, the domain size was increased to 4000 km by 2000 km allowing for standing eddies. The depth was also increased to 4000 m, increasing the number of vertical grid boxes to 40. We then included a continental slope and 2 complex ridges as shown in Fig. 5.1, similar to that used in previous studies (*Hogg*, 2010). We use partial cells in the MITgcm to account for the topography (*Adcroft et al.*, 1997).

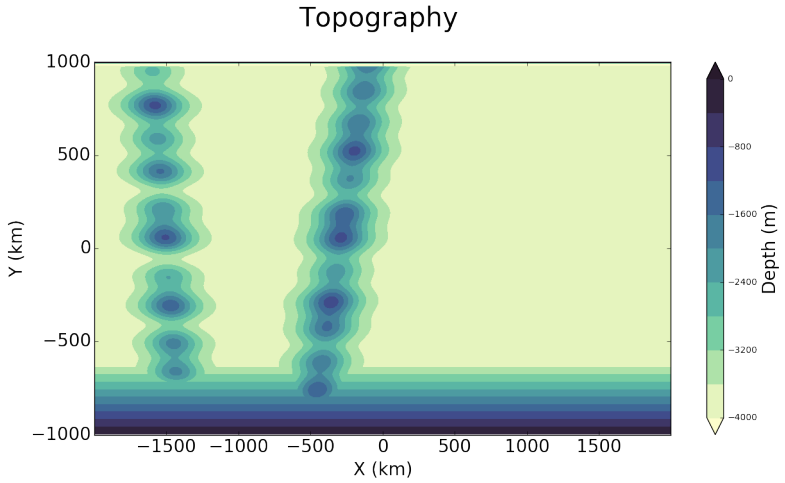

Figure 5.1: Topography included in non-flat bottom runs.

A Tubulent Kinetic Energy (TKE) scheme (*Gaspar et al.*, 1990; *Madec and Delecluse*, 1998) was employed to parametrise sub grid mixing. Key model parameters are outlined in Table 5.1. The surface heat and wind forcing remain unchanged from the fixed flux runs. To test the effect of topography we ran 2 experiments for the 2 extreme relaxation timescales: 3 days and infinite (closed northern boundary). These simulations were run for 400 and 1000 years respectively.

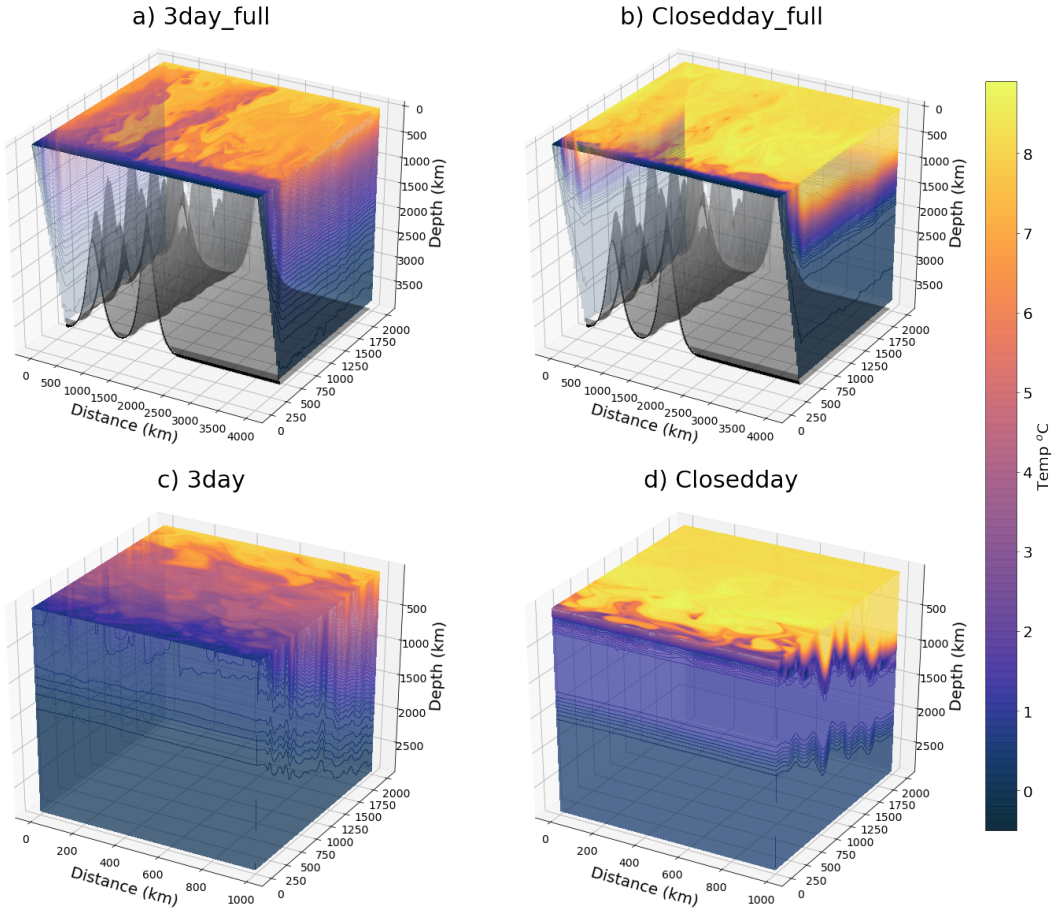

Figure 5.2: Instantaneous temperature field for a) and b) Topography runs. c) and d) flat bottom runs.

Table 5.1: Model Setup for fixed-flux runs with topography.

Symbol	**Description**	**Value**
L_x, L_y, H	Domain	4000 km, 2000 km, 4000 m
L_{sponge}	Length scale of sponge layer	100 km
Q_0	Surface heat flux magnitude maximum	0-10 W m^{-2}
τ_0	Max surface wind stress	0.2 N m^{-2}
dx, dy	Horizontal grid spacing	5 km
dz	Vertical grid spacing	5-266 m
Adv Scheme	7$^{\text{th}}$ order centred	7
τ_R	Sponge relaxation time scale	3-day and ∞

5.1.2 Overturning

First, we plot at the 3D instantaneous temperature field for both the flat bottomed runs and runs with topography (shown in grey) to highlight the main differences,

showing increased variability in the topography runs Fig. 5.2.a-b and flatter isotherms. We still see an internal boundary layer form in the closed run, but less sharp than in the flat bottomed runs. As with all runs, we check the Eulerian mean overturning looks sensible and consistent with all other runs. Fig. 5.3 shows the Eulerian MOC with topography is around 6 times larger (15 Sv) than the flat bottom runs (2.25 Sv).

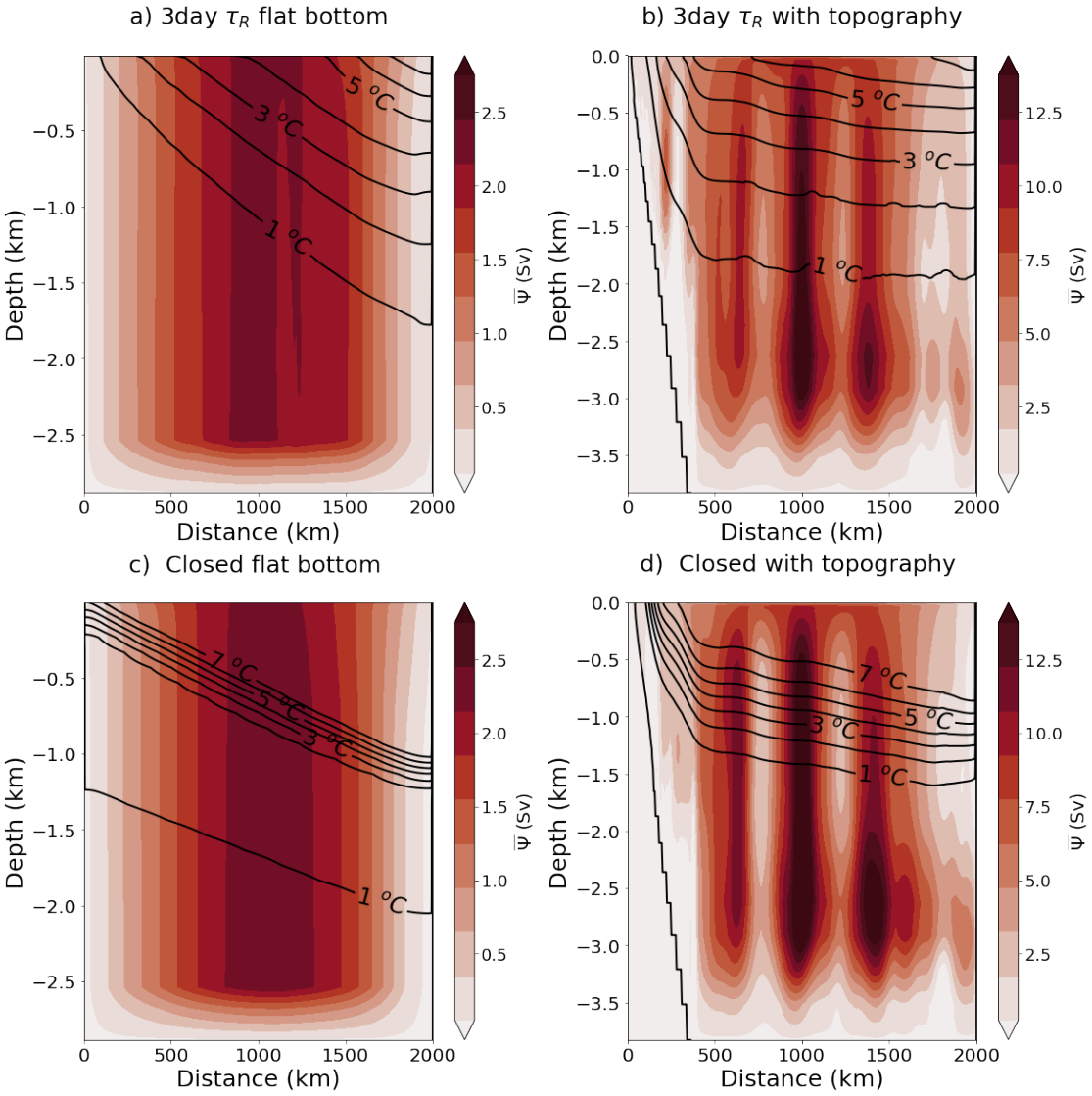

Figure 5.3: The Eulerian mean streamfunction ($\overline{\Psi}$) for Flat bottom runs a) and c) and for Topography runs b) and d).

We also see a different structure in the runs with topography Fig. 5.3, which is seen as a lobed structure in Fig. 5.3.b and d. This pattern is seen to be unchanged between averaging periods of 20 years to 100 years. Our ridges have some shallow

peaks extending into the upper 1000m (as does the real Southern Ocean topography (*Smith and Sandwell*, 1997)) of the ocean and the lobes may be due to the locations of the peaks as the overturning circulation must be above the topography (*Viebahn and Eden*, 2012). We also note the similarity to the increased top to bottom temperature difference run in chapter 4 where ΔT was set to 16 ^{o}C, similarly shallow isotherm and Eulerian overturning was generated. This lobed overturning structure is likely to be attributed to Reynold's stresses. This explains the strength of the MOC in the topography runs as the channel is 4 times longer and the the reynold's stresses sharpen the overturning areas leading to a 6 times larger overturning strength. However, as the "Deacon cell" (*Döös and Webb*, 1994) is a fictitious cell we will not focus on the structure of the Eulerian mean overturning.

As with the previous chapters, we calculate an isothermal stream function (Eq. (2.11)) to show the Residual Overturning Circulation (ROC). However, for the topography runs, we calculated the stream function over 82 discrete potential temperature layers, in order to account for areas with little temperature variation at depth. The isothermal stream function is shown in Fig. 5.4, showing a similar 3 cell SO ROC pattern aligned with isotherms. Fig. 5.5.b shows that the SO ROC remapped into depth in these runs closely matches the 3 cell circulation in the flat bottom runs which collapses [1]. The overturning strength is a factor of 5 stronger as would be expected with the longer channel and Reynolds stresses. We discuss here the qualitative differences between the equivalent runs with flat bottoms. In Fig. 5.5.b demonstrating that the fundamental ideas of how the SO ROC responds to stratification changes in the north of the domain still hold in models including topography. It should be noted that the lowermost cell of the SO ROC is still unrealistic in this idealised set up, as it is driven by diabatic processes not included in the idealised model. Its disappearance in these runs even in the presence of topography is not further discussed.

[1]The full spin up of the closed boundary run would take 3000 years, which is computationally too expensive. However, we know from the flat bottom experiments that the intense surface wind driven cell will disappear after 1000 years.

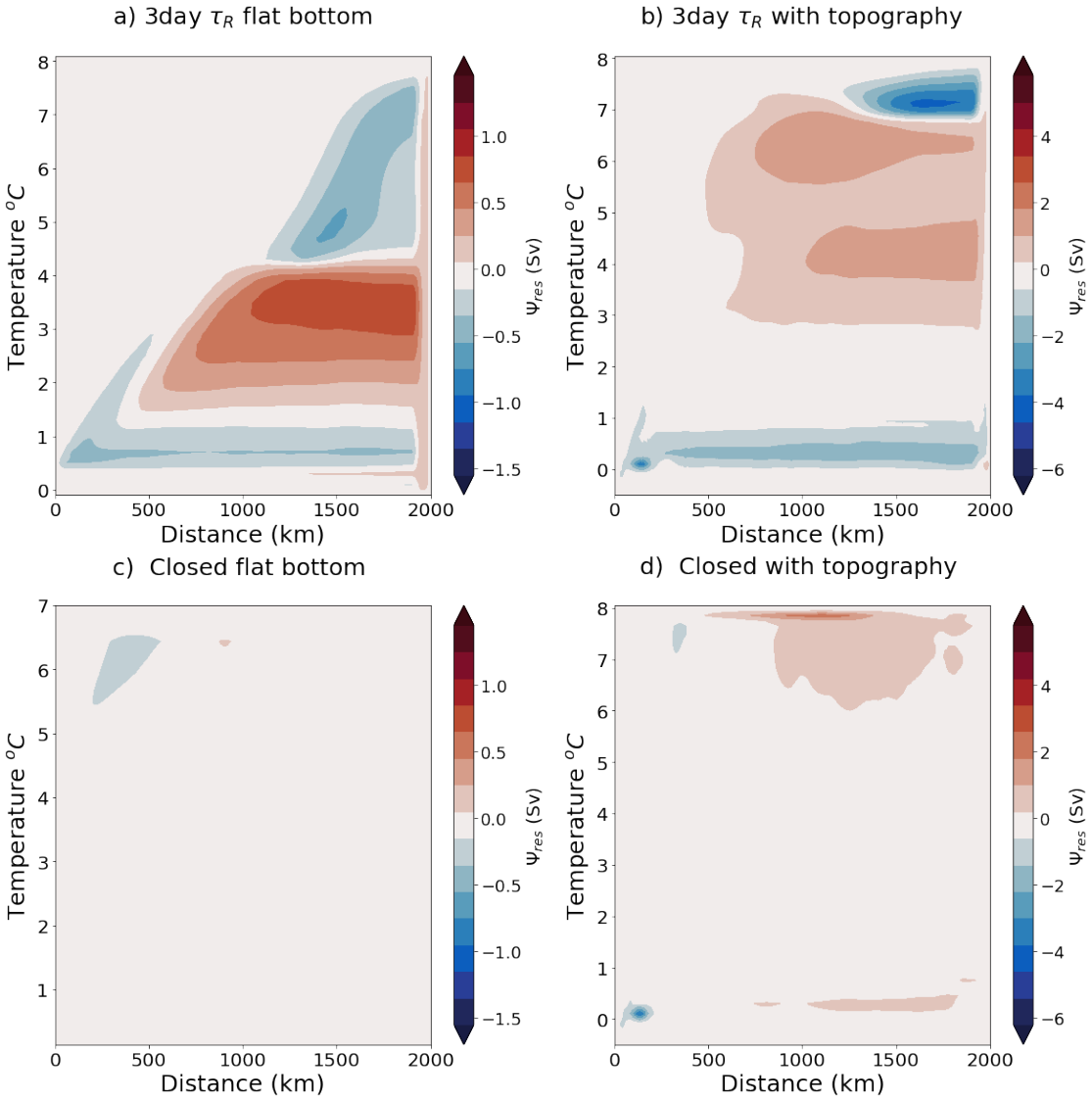

Figure 5.4: The isothermal stream function $\Psi_{res}(y, \theta)$ for relaxation time scales of 3 and infinite days for flat bottom a) and c) runs and topography runs b) and d).

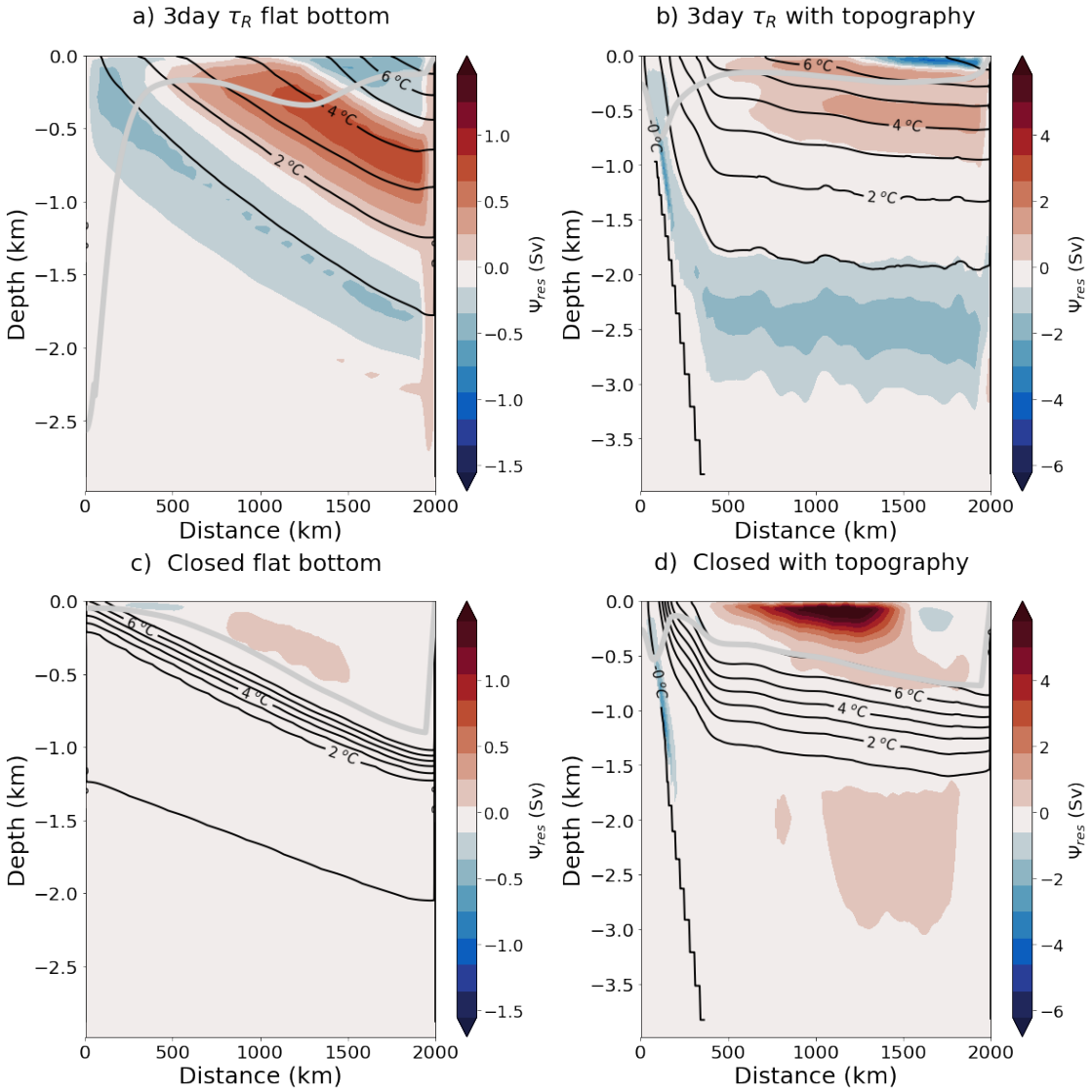

Figure 5.5: The isothermal stream function $\Psi_{res}(y, \theta)$ remapped onto depth coordinates, to give $\Psi_{res}(y, z)$ for relaxation time scales of 3 and infinite days for flat bottom a) and c) runs and topography runs b) and d). Isotherms in intervals of 1°C are overlaid as solid black contours. Above the surface heat forcing is displayed. Note change in colour scale between flat runs and topography runs

As well as the 3 cell SO ROC and its subsequent collapse the same pattern of stratification change between the open and closed northern boundary case occurs in the presence of topography. The sharp internal boundary layer that forms in the closed scenario appears much less sharp in the runs with the topography runs. We also see a shallowing of the mixed layer depth in the presence of topography for both the open and closed scenarios. Shoaling from 1200 m at the northern boundary in Fig. 5.5.c to 500 m in Fig. 5.5.d. This is also seen in *Abernathey and Cessi* (2014) suggesting that eddy efficiency is higher in the presence of topography with shallower slope isotherms and increased APE. Increased isopycnal tilt leads to an increase in available potential energy (APE) which would increase cross isothermal fluxes. Available Potential Energy (APE) is calculated by taking a volume integral of density perturbations following *Winters and Young* (2009), *Kang and Fringer* (2010) and *Abernathey and Cessi* (2014) :

$$APE = \int_z g(\rho^* - \rho_0) z \, \mathrm{d}z, \tag{5.1}$$

where ρ^* is the perturbed density and ρ_0 is the reference density. In these runs domain integrated APE when rescaled to take into account the domain size was similar (1.4 PJ (flat) and 6.5 PJ (with topography)). However plotting the depth integrated APE in Fig. 5.6, over topography, APE is much reduced in Fig. 5.6.b and d, but enhanced over the continental slop which is also where we find steep isothermal slopes, explaining some of the variation we see between flat bottom experiments and topography experiments.

5.1.3 Dynamics

Topography has a large influence on eddy dynamics with standing eddies playing a large role in eddy heat fluxes. However, if we look at the depth profile of the eddy heat fluxes in Fig. 5.7 there is a reduction in magnitude between no topography and

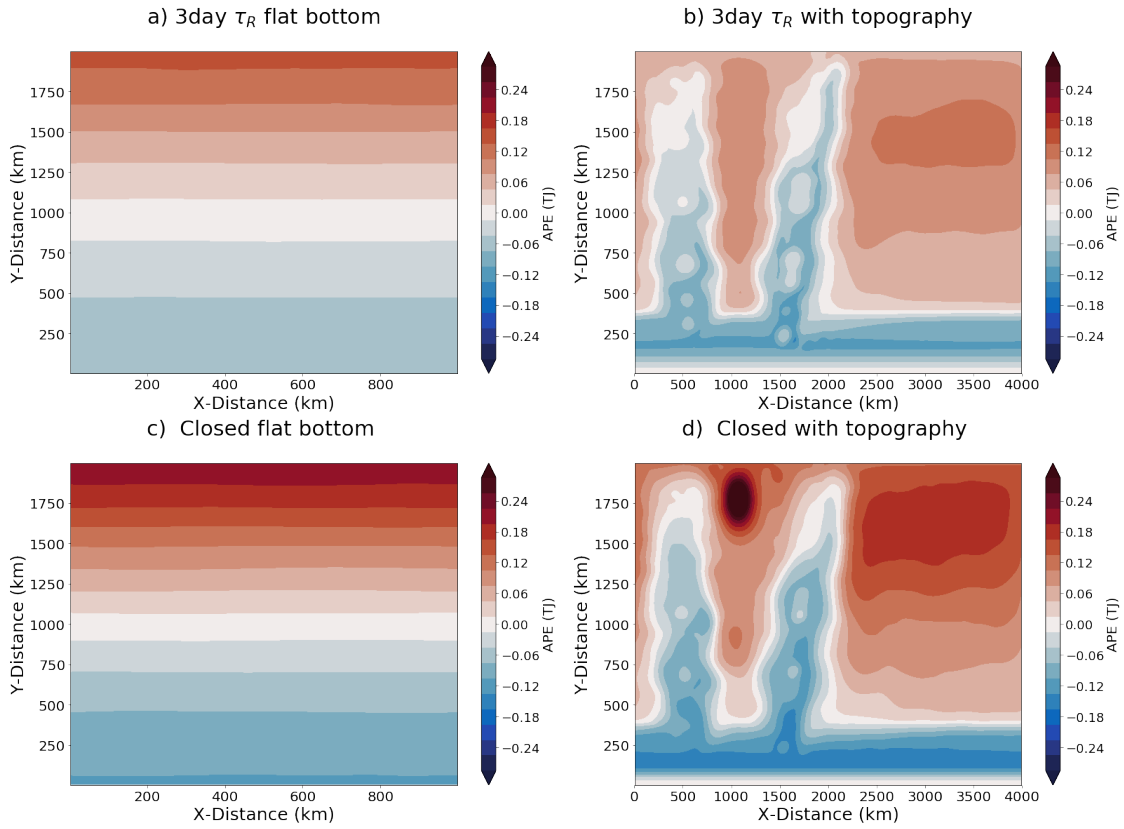

Figure 5.6: Depth integrated available potential energy. Calculated from Eq. (5.1)

topography runs, but the same general pattern between open and closed northern boundaries. Notably, a large deviation in the total heat flux arises between flat and topography runs with topography having larger downwards heat fluxes Fig. 5.7.b and d. Although the zonally averaged eddy fluxes are weaker when the depth integrated fluxes are plotted we see once again large increases around the ridges. Eddy heat fluxes are nearly 10 times larger in Fig. 5.8.b and d that the flat bottom runs a and c. Which like in *Abernathey and Cessi* (2014) suggest much more efficient eddies acting over a smaller area in our runs with topography. We can see much sharper surface temperature gradients in our topography forcing isotherms into narrow bands over which there is locally high heat fluxes.

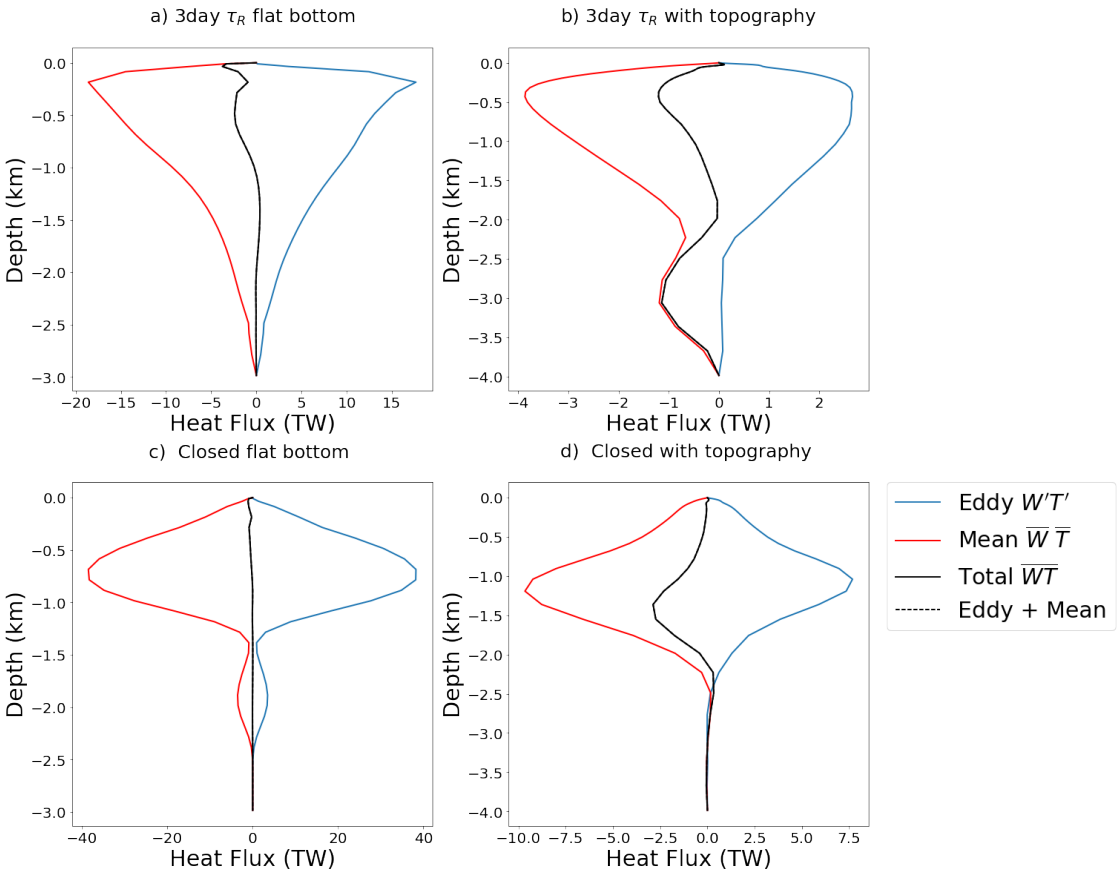

Figure 5.7: Vertical eddy heat flux (TW/m^2) for flat bottom runs a) and c) and topography runs b) and d). Mean vertical heat flux ($\rho_0 C_p \overline{w}\,\overline{T}$) is show in red, Eddy($\rho_0 C_p \overline{w'T'}$) in blue and Total ($\rho_0 C_p \overline{wT}$).

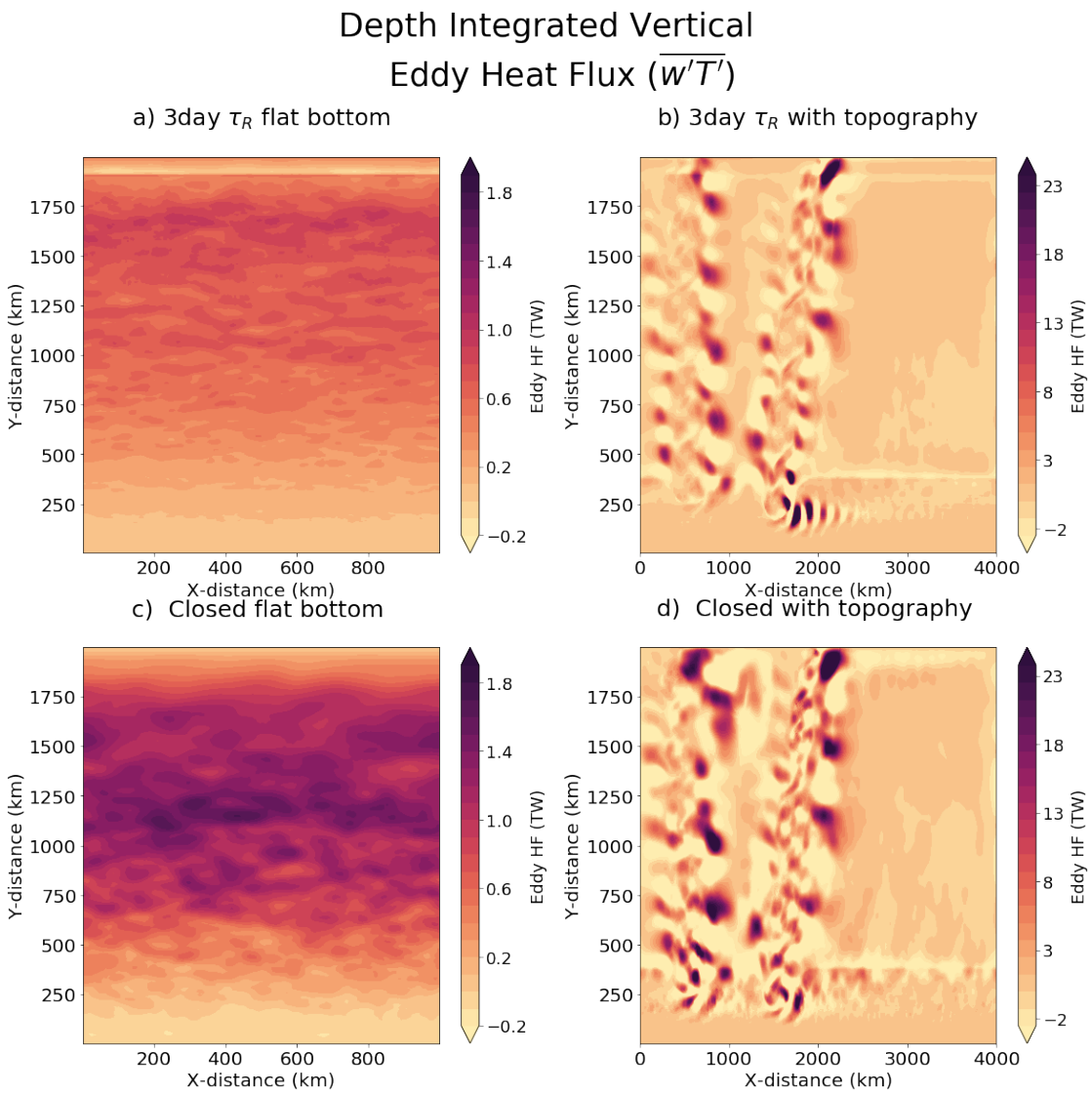

Figure 5.8: Vertically integrated eddy heat flux (TW/m^2) for flat bottom runs a) and c) and topography runs b) and d).

We can see this in the diabatic eddy heat flux divergence terms. The vertically integrated values shown in Fig. 5.9 show the convergence in uniform bands in the Fig. 5.9.a and c however locally very enhanced divergence and convergence around topography Fig. 5.9.b and d at over 100 times larger magnitude but confined to very short zonal areas except for over the continental shelf showing that although the net effect cancelling out the SO ROC still holds this is achieved around topography in strong dipole patterns. As with the experiments performed in *Abernathey and Cessi* (2014) we see the eddy heat flux divergence suppressed away from the topography in an inhomogeneous system generated by topography.

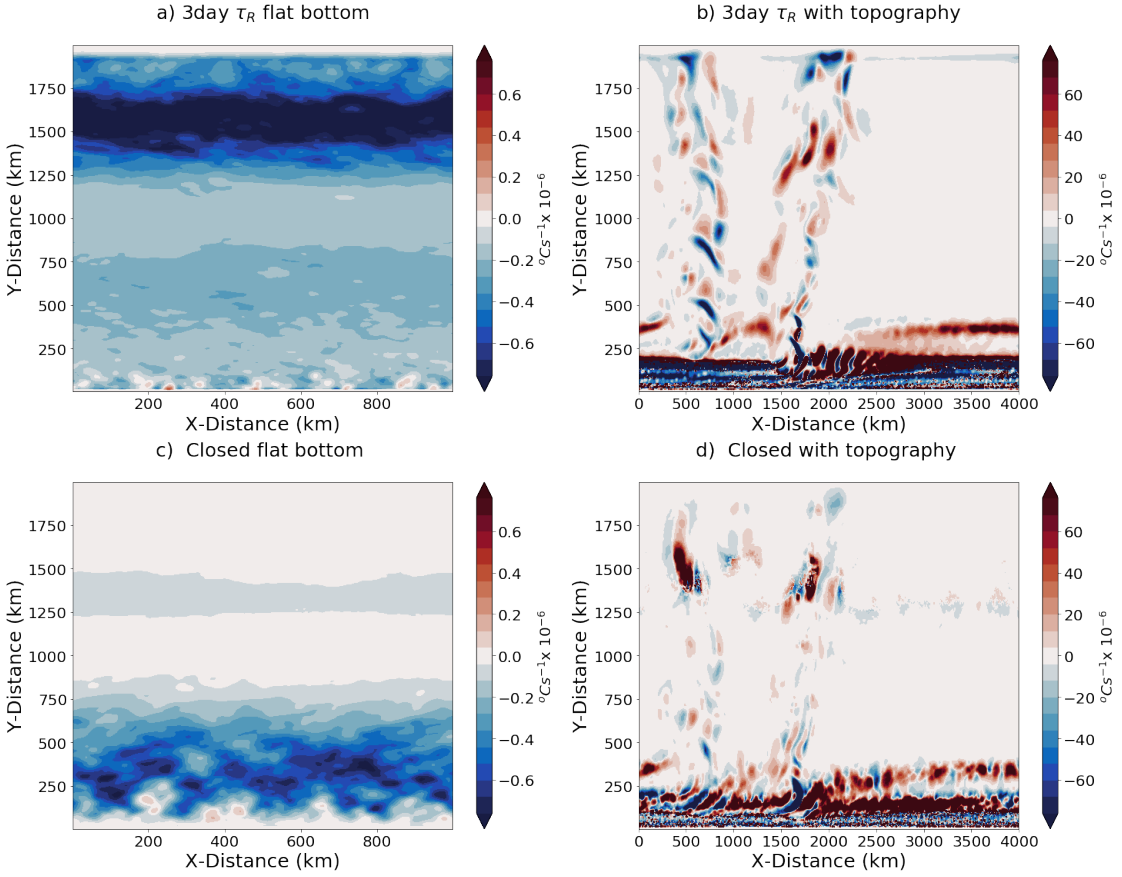

Figure 5.9: Vertically integrated diapycnal eddy heat flux divergence (D), for flat bottom runs a) and c) and topography runs b) and d).

Energetics

In presence of topography there are similar magnitudes of EKE maxima (within 10%) to the flat bottom scenario but a much higher domain average (greater than twice flat bottom domain average). As zonal means are not very appropriate in the presence of topography it is best to look at the vertically integrated EKE. EKE in the Southern Ocean is patchy with large enhancement downstream of topography as expected from satellite altimeter data (*Thompson*, 2008). This is very similar to the pattern seen in Fig. 5.8 the vertical eddy heat flux, $\overline{w'T'}$ is often taken as the eddy source term for EKE (*Cessi et al.*, 2006).

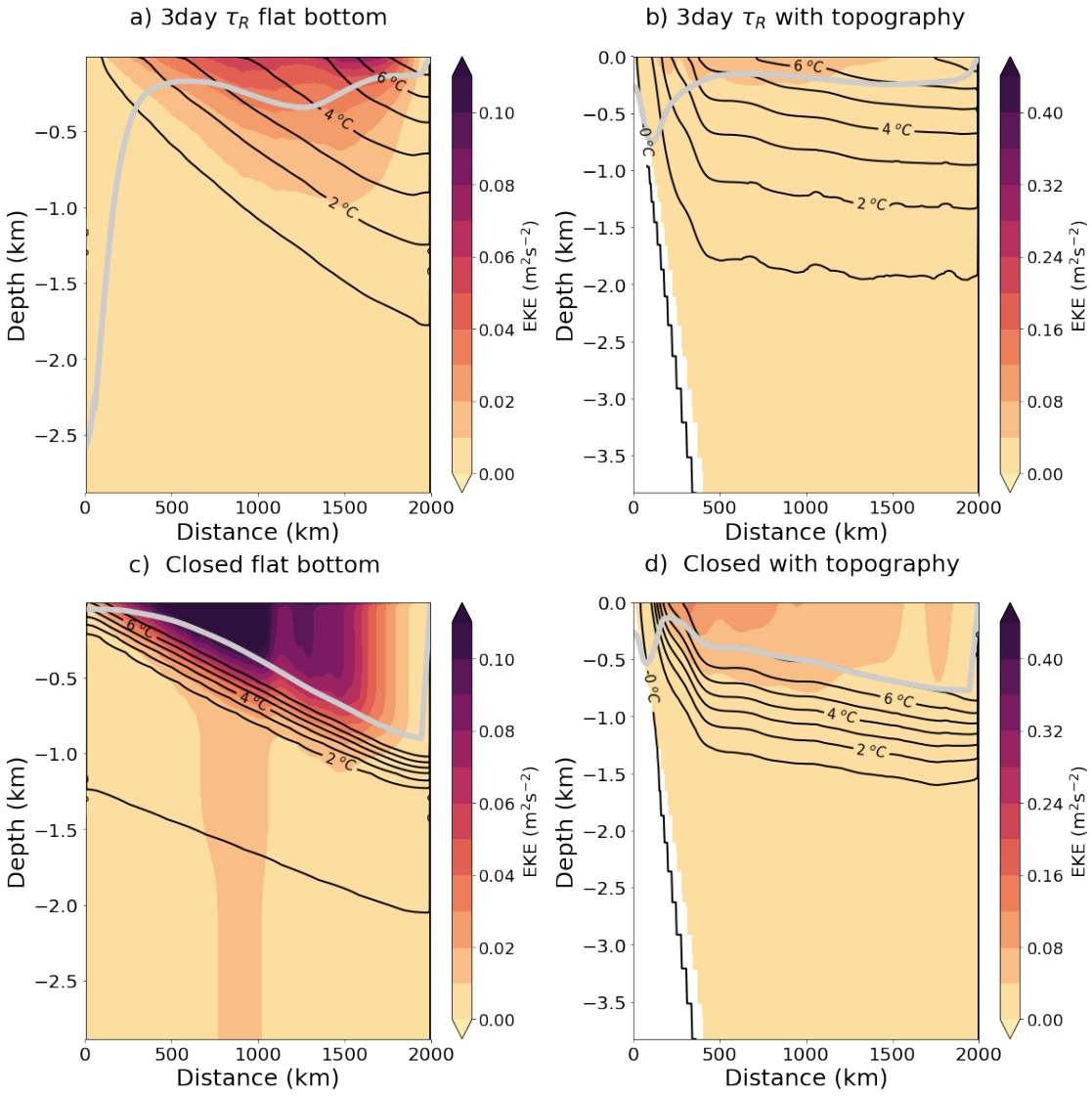

Figure 5.10: EKE $\frac{1}{2}(u^2 + v^2)$ sections for relaxation time scales of 3 and infinite days for flat bottom a) and c) runs and topography runs b) and d). Isotherms in intervals of 1°C are overlaid as solid black contours.

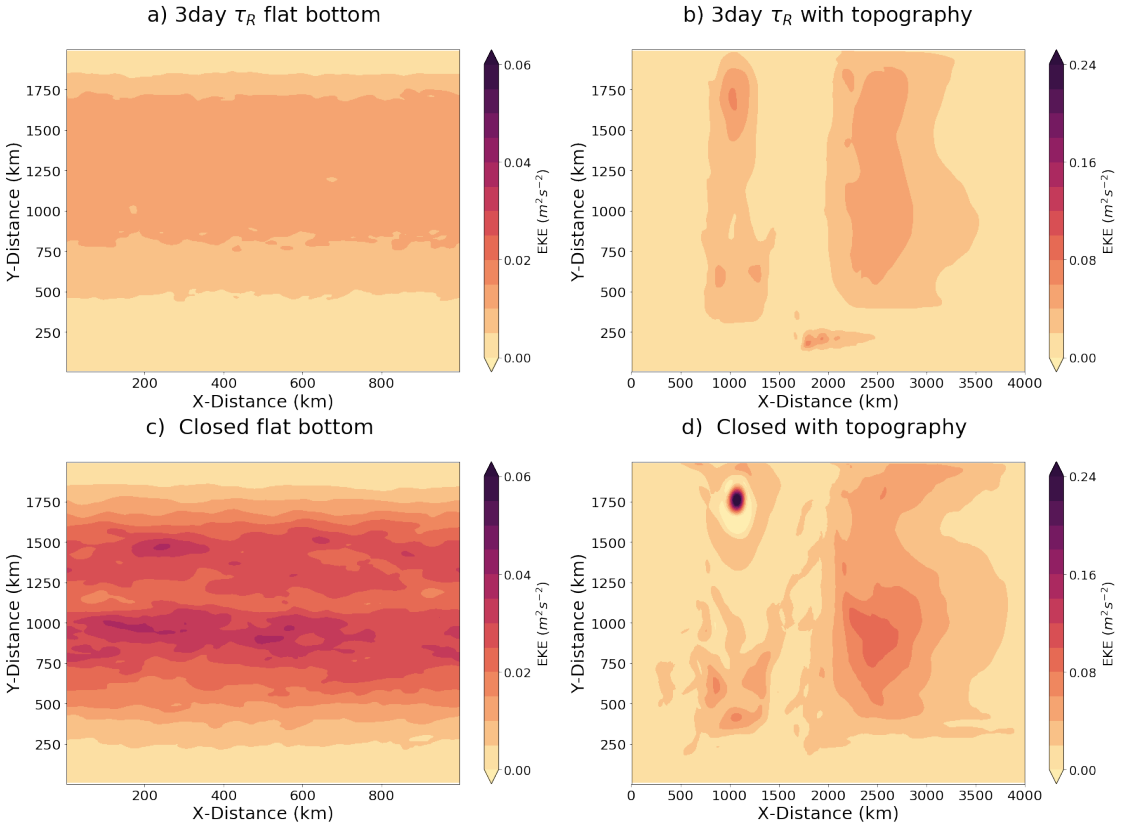

Figure 5.11: Vertically integrated EKE $\frac{1}{2}(u^2 + v^2)$ for relaxation time scales of 3 and infinite days for flat bottom a) and c) runs and topography runs b) and d).

5.2 ACC

The ACC, like the SO ROC the ACC is driven by wind and buoyancy forcing. In our channel runs we have seen large changes in EKE and stratification and, although wind forcing is kept constant, we are likely to see a response in the ACC. The ACC is set by a number of factors: wind stress (τ), surface buoyancy forcing and remote forcing altering stratification. The most basic way of calculating transport ($\mathcal{T}$) is:

$$\mathcal{T} = \iint_{-H}^{0} u \mathrm{d}z \mathrm{d}y \tag{5.2}$$

Where z = -H is the sea floor and $z = 0$ is the surface. If you substitute thermal wind into Eq. (5.2), where thermal wind is given as:

$$u_z = \frac{g}{f\rho_0}\rho_y \tag{5.3}$$

Transport can be written:

$$\mathcal{T} = \frac{g}{f\rho_0} \iint \rho_N - \rho_S \, \mathrm{d}^2 z \tag{5.4}$$

Showing the role of stratification in setting ACC strength as suggesting that interactions between diabatic eddies and stratification could modulate the ACC (*Hogg*, 2010). With the assumption that $u = 0$ m/s at $z =$ -H. Or more neatly put as:

$$\mathcal{T} = \frac{g}{|f_{ACC}|\rho_0} \int_{-H}^{0} z(\rho_N - \rho_S) \, \mathrm{d}z \tag{5.5}$$

(*Munday et al.*, 2011).

5.2.1 The ACC Response to Altered Northern Boundary Conditions

We examine here what happens to the ACC when the northern boundary condition is altered. To illustrate this we have looked at the fixed surface heat flux and surface restoring runs to see how the closing of the northern boundary affects the ACC as well as the surface boundary condition.

When closing the northern boundary the zonal flow noticeably increases. Fig. 5.12 shows how little surface boundary conditions affect the zonal velocities. A slight increase in velocity is noted with the marginally steeper isotherms in the fixed surface flux runs Fig. 5.12.b-d. For both surface heat forcing conditions, closing the northern boundary has a large effect on the zonal flow. When the northern boundary is closed a large temperature (density) difference is achieved across the ACC, with the sharp boundary layer leading the same difference across the ACC as the entire top to bottom temperature difference.

Breaking down into barotropic (depth averaged Fig. 5.13) and baroclinic (devi-

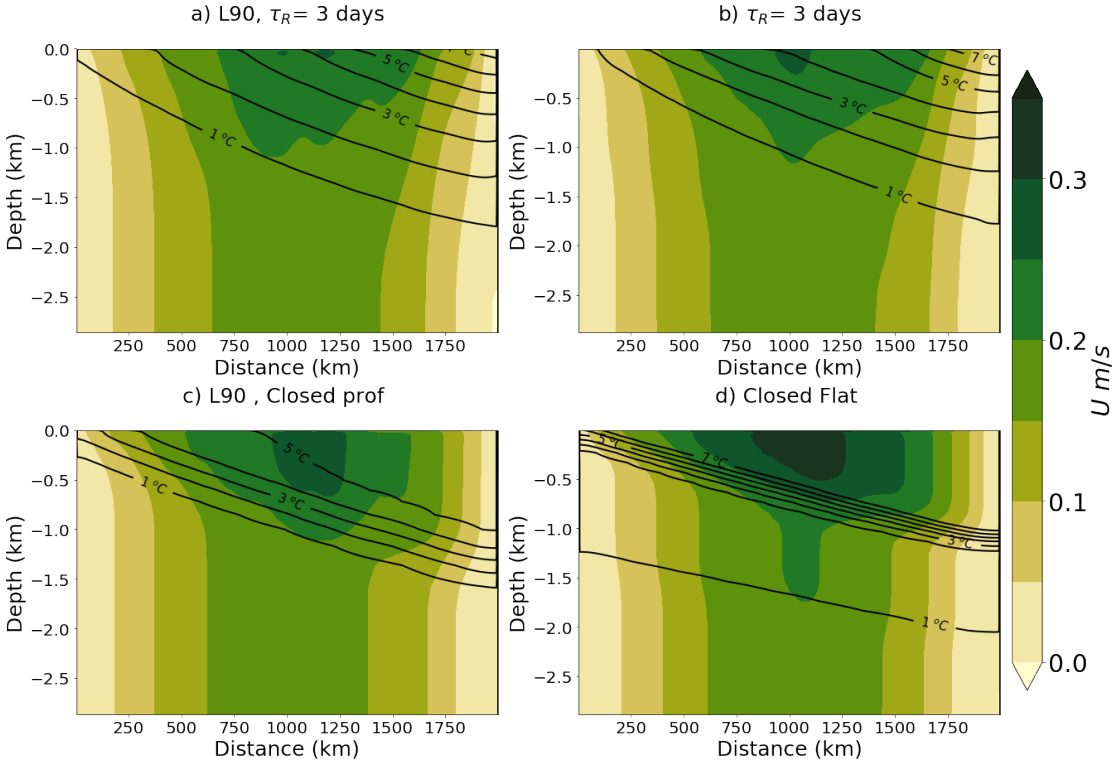

Figure 5.12: Zonal mean zonal velocity $\overline{u}$ m/s for a) Surface restoring with strong sponge layer, b) fixed heat fluxes and strong sponge layer, c) Surface restoring with Closed northern boundary and d) fixed heat fluxes with a closed northern boundary.

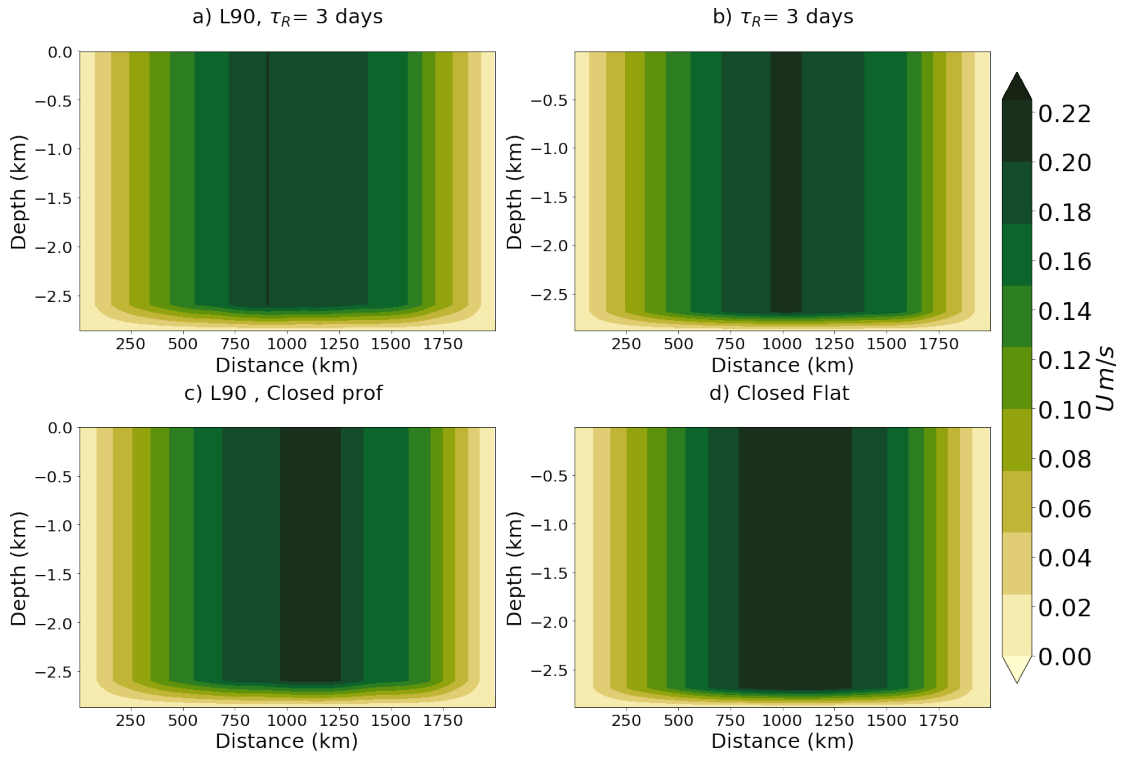

Figure 5.13: Zonal mean barotropic component of zonal velocity for a) Surface restoring with strong sponge layer, b) fixed heat fluxes and strong sponge layer, c) Surface restoring with Closed northern boundary and d) fixed heat fluxes with a closed northern boundary.

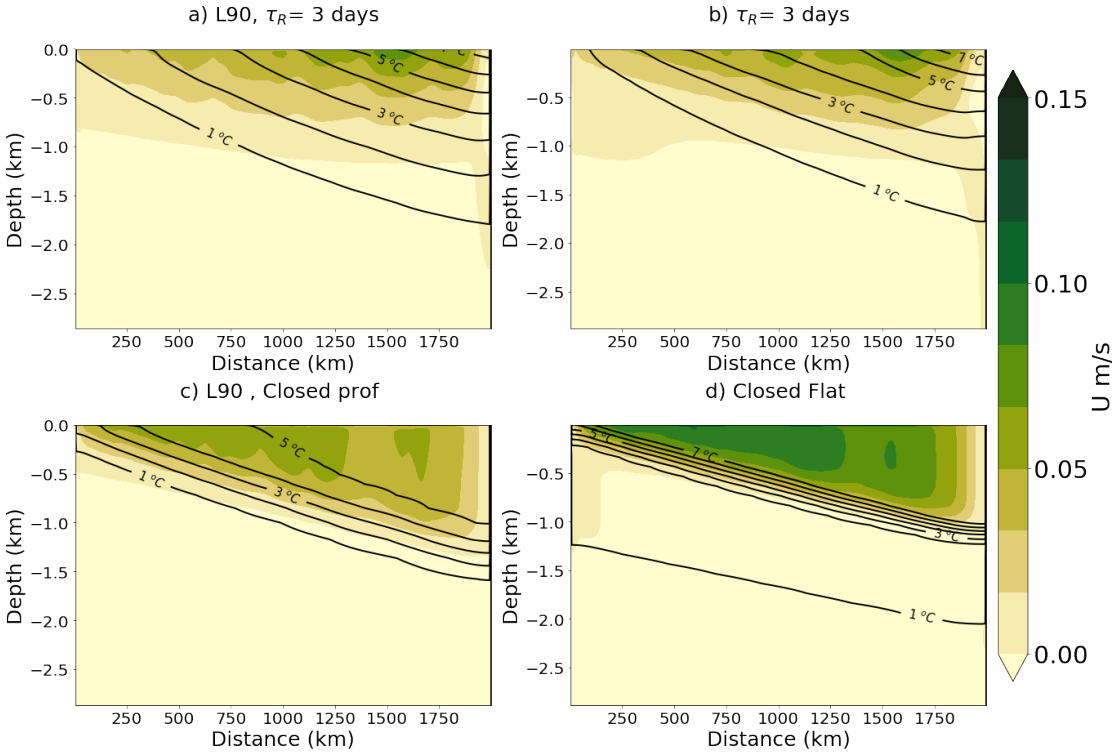

Figure 5.14: Zonal mean baroclinic component of zonal velocity for a) Surface restoring with strong sponge layer, b) fixed heat fluxes and strong sponge layer, c) Surface restoring with Closed northern boundary and d) fixed heat fluxes with a closed northern boundary.

ation from depth averaged Fig. 5.14) components show the surface heat forcing has little effect on the transport with a 3-day relaxation timescale. The major changes between open and closed northern boundary occur in the baroclinic component although a slight increase in the barotropic component is noted. When the northern boundary is closed there is a large increase in baroclinic transport, this increase is mostly seen in the surface mixed layer but this increase extends to depth. Arising from the sharp internal boundary layer, largest in the fixed flux runs where the internal boundary layer creates the strongest gradient. Interestingly the barotropic transport is more noticeably increased when the northern boundary is closed with fixed surface heat fluxes, this could suggest that the choice of surface heat forcing has an effect on the degree of eddy saturation which corroborates the findings of *Zhai and Munday* (2014) who found shorter time scales of surface restoring increased eddy saturation. With surface restoring at shorter timescales the isotherms are 'pinned' both at the surface and at the northern boundary here the baroclinic part of the ACC is dependent on the buoyancy gradient across the ACC which here is set by the restoring conditions rather than the wind. Suggesting that saturation is effectively set by the northern boundary condition. Interestingly we see for 3-day relaxation time scale sponge runs there is little difference in the ACC transport and similar isopycnal slope, yet drastically differing SO ROC strength suggesting greatly increased eddy compensation in the surface restoring run. This is in fitting with the results of *Morrison and Hogg* (2013) and *Zhai and Munday* (2014) who suggest that eddy compensation and saturation are strongly dynamically linked. This suggests the boundary conditions applied in Southern Ocean channel models may affect the SO ROC and ACC in vary different ways and must be taken in consideration when investigating their response to altered parameter most significantly wind stress variation.

Chapter 6

Discussion

6.1 Summary

The original motivation for this work was to investigate far field forcing of the Southern ocean, we showed in all cases for our channel model the upper cell of the SO ROC collapses when diabatic forcing in the northern sponge-layer is absent. These results underscore the inter hemispheric link between the SO ROC and the northern hemisphere Atlantic Meridional Overturning Circulation (AMOC) . Such links were previously demonstrated in *Gnanadesikan and Hallberg* (2000) and *Wolfe and Cessi* (2011). More fundamentally however these results showed the limitations and considerations required when setting up a regional model of the Southern Ocean. Here, by altering the northern boundary condition we showed how the SO ROC adjusts to changes in stratification at the northern end of the SO channel. It should be stressed that the representation of the far-field forcing, i.e. NADW formation, by a sponge layer with a prescribed e-folding stratification is crude and should be tested against other ways of closing the SO ROC. Nevertheless, the absence of any mimicking of far-field forcing implies a disconnection between the SO ROC and the AMOC , and our results imply that in this case the upper cell of the SO ROC cannot be maintained. Both the choice of northern boundary

and surface forcing conditions greatly alter the dynamics of the Southern Ocean. Despite the SOROC collapsing in a variety of channel model set ups, the processes contributing to the collapse of the SO ROC are altered by the very sensitive set up of the channel model.

The crucial role of diabatic eddy heat fluxes in the adjustment process to such changes highlights the need for a carefully designed diabatic eddy representation in the surface mixed layer of the ocean, which should also depend on the atmospheric state and forcing. Our results also imply that diabatic eddy fluxes can be essential in closing the heat budget and that coarse resolution ocean (and hence climate) models that do not represent mesoscale eddies without parameterizing the diabatic eddy fluxes may not adequately close the heat budget and simulate the response to changing heat fluxes. We chose here to evaluate the diabatic eddy heat fluxes as the diapycnal heat flux divergence in the heat budget to account for the variation between runs altering the effectiveness of various approximations in the mixed layer using TEM framework. The diapycnal eddy heat flux divergence strongly responds to changes in the northern boundary condition, becoming larger (increasing by 250% in amplitude) when the stratification at the northern boundary is better able to freely evolve and is less constrained by the circulation and diabatic processes in the sponge layer. The resulting changes in diabatic forcing lead to a dramatic increase in surface mixed layer depth, which leads to enhanced baroclinic instability, larger EKE and EPE . This result is qualitatively robust to the surface boundary condition but, when surface restoring is applied instead of a fixed flux formulation, a much smaller increase in diabatic fluxes occurs and EKE is more constrained. Nevertheless, the role of diabatic eddy fluxes in the vertically integrated heat budget is equally large for both surface boundary conditions. The diabatic eddy heat flux divergence is sensitive to both the strength and sense of the surface heat forcing and the diabatic forcing in the sponge layer.

6.2 Closing the Northern Boundary

Motivated by the notions of far field forcing of the Southern Ocean, we investigated what considerations would be required to understand the dynamics of how this would be achieved. We found that the boundary conditions chosen can have large impacts on the eddy dynamics in a channel model. Here we have hinted at some processes that may be involved in altering the SO ROC in different climatic states but, more fundamentally we have shown the various limitations of channel model boundary conditions when investigating idealised SO ROC theory.

Using a standard set up, we achieve the MR03 predicted 3 cell SO ROC. When the northern boundary is closed the SO ROC upper cell, which could be thought of as an extension of the AMOC, disappears. In all cases when the northern boundary is closed the traditional 3 cell SO ROC ceases to exist. Depending on the boundary condition we may see different circulation patterns, such as the surface intensified circulation seen in the surface restoring runs (Fig. 3.9), but these surface cells have no connection to the northern boundary or the deep. When diabatic forcing becomes stronger in the sponge layer (short τ_R), the upper cell in the SO ROC gains in amplitude and becomes comparable to the observed SO ROC strength. In this regime the diapycnal eddy heat flux divergence is always of first order importance, counteracting the advective heat transport, with opposing divergence-convergence patterns producing and effective surface heat forcing term as a smaller residual.

The vertical integral of the diapycnal eddy heat flux convergence decreases by an order of magnitude for weaker diabatic forcing in the sponge layer, although the eddy flux divergence terms themselves increase by a factor of 2 to 3 between a closed basin and a configuration with a strong relaxation to a prescribed temperature profile in the sponge layer. Using fixed fluxes these changes are reconciled by the establishment of a strong internal boundary layer with a large vertical temperature gradient. Advective heat transport divergence by a weak SO ROC is confined to a strong northward deepening mixed layer and the diapycnal eddy heat flux di-

vergence appears as dipoles of opposing signs due to our choice of heat budget terms. Diapycnal eddy heat flux convergence occurs above the internal boundary layer and divergence below, while the advective heat transport divergence associated with the SO ROC in the mixed layer shows the opposite pattern. Without diabatic forcing in a northern boundary sponge layer diabatic eddies cancel the effective surface buoyancy forcing, while the heat transport divergence by the SO ROC integrates to zero in the vertical. As a result, below the surface mixed layer the SO ROC completely collapses, because the connection to an adiabatic pole-to-pole circulation ceases to exist.

For fixed surface heat fluxes the SO ROC responds to changing northern boundary conditions via changes in the effective buoyancy forcing achieved though increased diabatic eddy fluxes. Throughout this thesis a selection of model runs were shown but many additional runs were performed, particularly, for the experiments varying the relaxation time-scale. If we examine all the fixed flux runs performed, there is a common factor between all these experiments: the sponge layer profile changes the background stratification. We can compare all these runs in terms of stratification by looking at Brunt Väisälä frequency N^2 (T_z in our model). We plot the average sponge layer % increase in N^2 (increase from the run with the lowest average N^2 as a percentage) vs % decrease in domain integrated SO ROC strength for all fixed surface flux experiments (8 relaxation timescale experiments and 9 altered sponge layer temperature profiles), this includes runs referenced to but not shown in earlier chapters. To establish if there is a relationship we linearise the curve N^2 vs domain integrated SO ROC by taking the natural logarithm of the increase in N^2 and perform a linear regression to give a line of best fit shown in Fig. 6.1[1]. This gives an exponential decay with N^2. With fixed surface fluxes it appears a very strong negative correlation with increased integrated N^2 and integrated SO ROC with R value of -0.91.

[1]Some runs that were not shown previously were not spun up completely, slightly larger kinetic energy fluctuations are seen in these runs, which may account for some of the outliers in Fig. 6.1

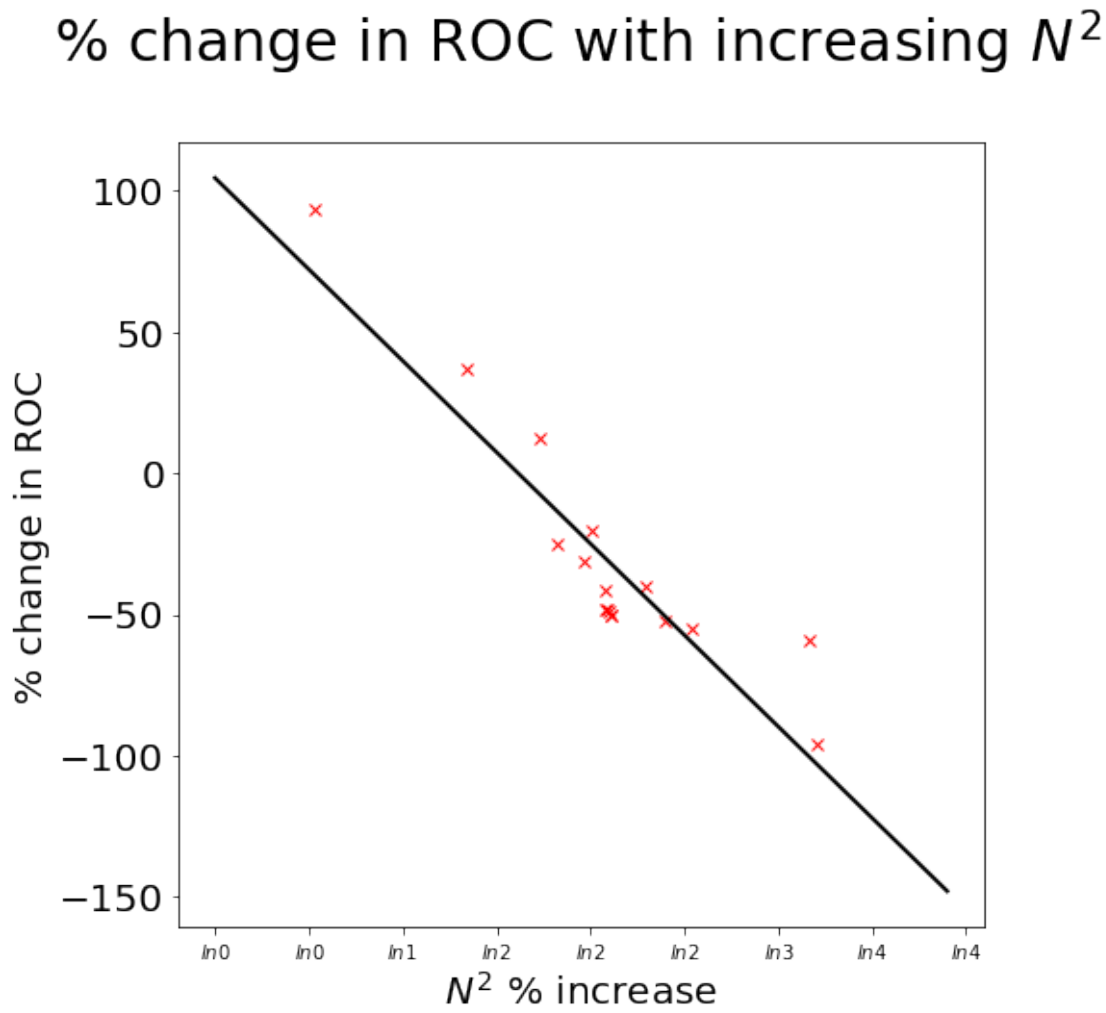

Figure 6.1: Linear regression line of best fit for % increase in integrated absolute SO ROC strength with natural logarithm of % increase in N^2. y = mx +c , m = -27, c = -2, R value of -0.91 and a P value = 3 x 10^{-7}.

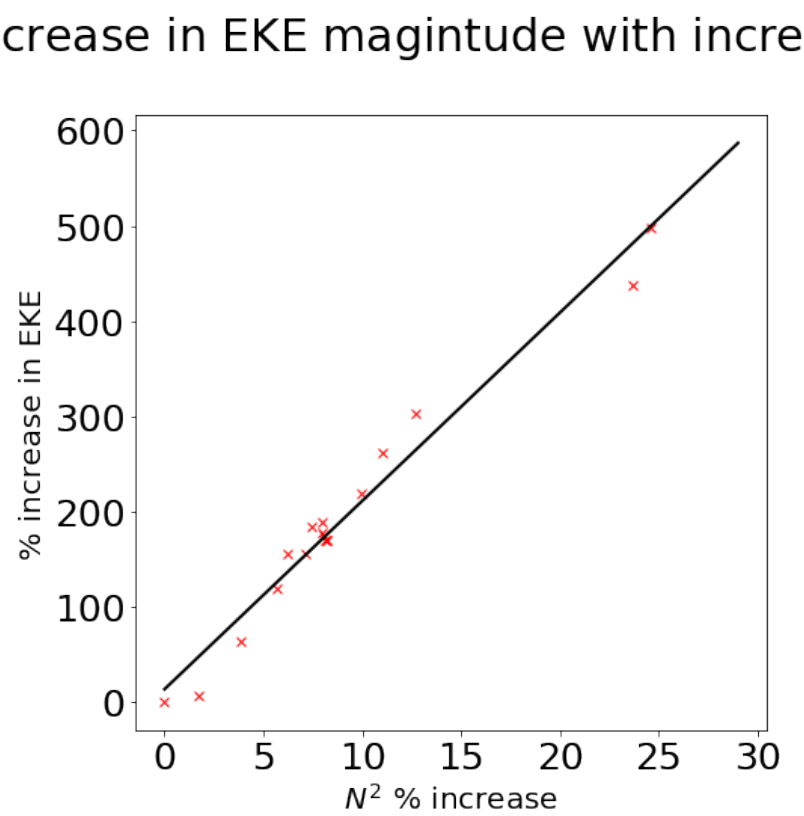

Figure 6.2: Linear regression line of best fit for % increase in EKE with % increase in N^2. y = mx +c , m = 15, c = 15, R = 0.98, p value = 1.5^{-13}

As we can see a clear trend of increasing integrated sponge N^2 leading to decreasing integrated SO ROC and one of the major patterns we've seen with the collapsing SO ROC is increasing EKE that leads into the increase of increased diabatic eddy heat fluxes. This is also seen when plotting % increase in domain integrated EKE against % increase in sponge integrated N^2. Fig. 6.2 shows a 25 % increase in N^2 gives rise to a dramatic 400% increase in EKE.

This implies that the choice of northern boundary condition influences the domain wide dynamics e.g. lower relaxation time-scales or deeper thermocline will lead to increased amounts of EKE and greater eddy compensation before altering the surface forcing.

6.3 The Surface Heat Forcing

Regardless of our choice in surface heat forcing there is a collapse in the SO ROC which, with a sponge, can be weakly maintained even in absence of any surface heat forcing (Fig. 3.8 *See chapter 3*) by the diabatic forcing of the sponge layer alone. There are large changes in the channel dynamics with surface restoring, primarily in the surface mixed layer altering the diapycnal fluxes. When using a restoring boundary condition the main balance in the vertically integrated heat budget is somewhat different because no internal boundary layer develops and the northward deepening of the mixed layer is absent. The role of the changing surface heat forcing mimics salinity driven (fixed fluxes) vs temperature driven (restoring) dynamics and this plays a role in setting the Southern Ocean dynamics in these differing regimes. For most of the worlds ocean buoyancy variations are dominated by temperature variations (variations in atmospheric temperature) most accurately represented by a restoring condition. The Southern Ocean, however, differs from this and is dominated by freshwater fluxes (*Pellichero et al.*, 2018). which is more accurately represented by fixed-flux surface conditions[2] although in reality the ocean is like likely to be best represented through a mixture of these boundary conditions (*Stewart et al.*, 2014). The choice of surface heat forcing alters the depth of the mixed layer, isopycnal slope, EKE and domain wide stratification, which impacts the ACC and SO ROC. Our results show that the choice of correctly matching the surface restoring profile and the sponge layer forcing have very large implications on the response of the SO ROC. When a different surface profile is used we can achieve a full collapse of the SO ROC. Surface restoring versus fix-fluxes has been to shown as large control on degree of eddy compensation in ocean models (*Gent*, 2015). Due to these factors we can not find any such promising relation between the Northern Boundary stratification and SO ROC strength or EKE strength as we could see in the fixed flux cases. This should serve as strong consideration when setting up channel models to investigate SO theory.

[2]Very poorly constrained, so fixed-flux is simply more adequate (*Jansen and Nadeau*, 2016)

6.4 Effects of Topography

When considering the Southern Ocean it is important to consider the effects of topography as it affects the ACC generating stationary meanders (*Naveira Garabato*, 2009) and alters the distribution of EKE (*Thompson and Sallée*, 2012). We briefly ran some experiments to assess the possible implications of topography on the SO ROC response to altering the northern boundary conditions. In these runs we still see qualitatively the same scenario despite the topography altering the distribution of EKE and the channel dynamics. The same 3 cell SO ROC is established at short relation timescales and this circulation collapses when the northern boundary is closed, existing only as an intense diabatically driven surface cell. As with the flat bottomed experiments deep mixed layer is generated when the northern boundary is closed alongside a large increase in EKE associated with a diminished SO ROC. Qualitatively the overall trends are similar, but with a much more localised response with topography. *Rosso et al.* (2015) suggests that the role of topography may be further underestimated as a forward cascade of energy may lead to large influences on submesocale scales influencing diabatic eddies in the mixed layer.

6.5 Future Work

Our channel model is very idealised: the next steps in understanding the role of diabatic eddies would need to involve the implementation of a more appropriate framework alongside moving to a less idealised setup. The original theory we worked from uses buoyancy budgets, not simply temperature alone, to evaluate the SO ROC. In the cold temperatures of the Southern Ocean salinity plays a large role in setting the density of the ocean. Changing to an equation of state varying with salinity and temperature may lead to a clearer understanding of the role of surface forcing, with large discrepancies between fixed surface heat fluxes and surface restoring here suggesting differences between salinity driven and temperature

driven forcing, however the true surface forcing is likely to be a combination of temperature and salinity. Coupling to an atmosphere would provide insight into the implications for air sear fluxes, that these large changes in mixed layer heat flux divergence would lead to. The air-sea interactions may enhance the diabatic buoyancy forcing or dampen them. Sea ice can alter the surface buoyancy forcing and studies such as *Ferrari et al.* (2014) suggest that sea ice can play a large role on the forcing of the deep ocean though altering the northern extent of the summer sea ice.

In chapter 5 both the surface heat condition and the northern boundary condition affected eddy saturation suggesting closing the northern boundary and surface restoring increased saturation. Surface restoring is already known to have effects on setting the eddy saturation of a channel model, with stronger restoring giving stronger saturation (*Zhai and Munday*, 2014).

In the introduction and in chapter 2 we introduced TEM theory from *Marshall and Radko* (2003) and the original *Andrews and McIntyre* (1976). One of the limitations is that we calculate the residual overturning stream function as an isopycnal streamfunction which deviates from the real residual streamfunction the most in the surface layers, this deviation is reduced by increasing the number of temperature layers the stream function is calculated over, however this is very computationally expensive. In atmospheric sciences *Pauluis et al.* (2011) developed a Statistical Transformed Eulerian Mean (STEM) which when applied to the ocean does not break down at the surface (*Wolfe*, 2014). STEM assumes that velocity and tracer fields can be represented by random processes possessing the same moments as the modelled field. STEM also uses standard model output fields which makes for easier implementation which, in light of suggesting that realistic set-ups are required to fully understand the SO dynamics, could be a tool to do so in a less computationally demanding manner.

There is still a lot more we need to understand about the Southern Ocean dynamics

to fully comprehend all the feedbacks that may determine the SO ROC response to altered climates. The theory we have discussed here about the role diabatic eddies might play as well as highlighting the challenges in setting up experiments to test Southern Ocean. Demonstrating how the SO ROC and eddy dynamics may be set by the northern boundary and surface forcing condition regardless of parameter being varied in a channel model experiment.

Bibliography

Abernathey, R., and P. Cessi, Topographic enhancement of eddy efficiency in baroclinic equilibration, *Journal of physical oceanography*, *44*(8), 2107–2126, 2014.

Abernathey, R., and C. Wortham, Phase Speed Cross Spectra of Eddy Heat Fluxes in the Eastern Pacific, *Journal of Physical Oceanography*, (2010), 1285–1300, 2015.

Abernathey, R., J. Marshall, and D. Ferreira, The dependence of Southern Ocean meridional overturning on wind stress, *Journal of Physical Oceanography*, *41*(12), 2261–2278, 2011.

Abernathey, R., D. Ferreira, and A. Klocker, Diagnostics of isopycnal mixing in a circumpolar channel, *Ocean Modelling*, *72*, 1–16, 2013.

Adcroft, A. J., C. Hill, and J. Marshall, Representation of topography by shaved cells in a height coordinate ocean model, *Monthly Weather Review*, *125*(9), 2293–2315, 1997.

Adcroft, A. J., C. Hill, J.-M. Campin, J. Marshall, and P. Heimbach, Overview of the formulation and numerics of the MITgcm, *Proceedings of the ECMWF seminar series on Numerical Methods Recent developments in numerical methods for atmosphere and ocean modelling*, pp. 139–149, 2004.

Allison, L. C., H. L. Johnson, D. P. Marshall, and D. R. Munday, Where do winds drive the Antarctic Circumpolar Current?, *Geophysical Research Letters*, *37*(12), 1–5, 2010.

Andrews, D. G., and M. E. McIntyre, Planetary waves in horizontal and vertical shear: The generalized Eliassen-Palm relation and the mean zonal acceleration, *Journal of the Atmospheric Sciences*, *33*, 2031–2048, 1976.

Ballarotta, M., S. Drijfhout, T. Kuhlbrodt, and K. Döös, The residual circulation of the Southern Ocean: Which spatio-temporal scales are needed?, *Ocean Modelling*, *64*, 46–55, 2013.

Boccaletti, G., R. Ferrari, and B. Fox-Kemper, Mixed layer instabilities and restratification, *Journal of Physical Oceanography*, *37*, 2228–2250, 2007.

Böning, C. W., A. Dispert, M. Visbeck, S. R. Rintoul, and F. U. Schwarzkopf, The response of the Antarctic Circumpolar Current to recent climate change, *Nature Geoscience*, *1*(12), 864–869, 2008.

Britain, G., R. A. D. E. Szoeke, R. A. de Szoeke, and M. D. Levine, The advective flux of heat by mean geostrophic motions in the Southern Ocean, *Deep Sea Research Part A. Oceanographic Research Papers*, *28*(10), 1057–1085, 1981.

Campin, J.-M., A. J. Adcroft, C. Hill, and J. Marshall, Conservation of properties in a free-surface model, *Ocean Modelling*, *6*(3-4), 221–244, 2004.

Cerovečki, I., A. Plumb, and W. Heres, Eddy transport and mixing in a wind-and buoyancy-driven jet on the sphere, *Journal of Physical Oceanography*, *39*(5), 1133–1149, 2009.

Cerovečki, I., L. D. Talley, and M. R. Mazloff, A comparison of southern ocean air-sea buoyancy flux from an ocean state estimate with five other products, *Journal of Climate*, *24*(24), 6283–6306, 2011.

Cessi, P., W. R. Young, and J. A. J. Polton, Control of large-scale heat transport by small-scale mixing, *Journal of physical oceanography*, *36*(10), 1877–1894, 2006.

Chang, J., et al., *Methods in computational physics. Vol._17: General circulation models of the atmosphere.*, 1977.

Collins, S. N., R. S. James, P. Ray, K. Chen, A. Lassman, and J. Brownlee, Grids in numerical weather and climate models, in *Climate Change and Regional/Local Responses*, edited by Y. Zhang and P. Ray, chap. 04, InTech, Rijeka, 2013.

Cox, M., and K. Bryan, A numerical model of the ventilated thermocline, *Journal of physical oceanography*, *14*, 674–687, 1984.

Daru, V., and C. Tenaud, High order one-step monotonicity-preserving schemes for unsteady compressible flow calculations, *journal of computational physics*, *193*, 563–594, 2004.

Döös, K., and D. Webb, The Deacon cell and the other meridional cells of the Southern Ocean, *Journal of Physical Oceanography*, 1994.

Farneti, R., and T. L. Delworth, The role of mesoscale eddies in the remote oceanic response to altered Southern Hemisphere winds, *Journal of Physical Oceanography*, *40*(10), 2348–2354, 2010.

Ferrari, R., M. F. Jansen, J. F. Adkins, A. Burke, A. L. Stewart, and A. F. Thompson, Antarctic sea ice control on ocean circulation in present and glacial climates, *Proceedings of the National Academy of Sciences*, *111*(24), 8753–8758, 2014.

Ferreira, D., J. Marshall, and P. Heimbach, Estimating eddy stresses by fitting dynamics to observations using a Residual-Mean ocean circulation model and its adjoint, *Journal of Physical Oceanography*, *35*, 1891–1910, 2005.

Ferreira, D., J. Marshall, C. M. Bitz, S. Solomon, and A. Plumb, Antarctic ocean and sea ice response to ozone depletion: A two-time-scale problem, *Journal of Climate*, *28*(3), 1206–1226, 2015.

Gaspar, P., Y. Grégoris, and J. Lefevre, A simple eddy kinetic energy model for simulations of the oceanic vertical mixing., *Journal of Geophysical Research*, *95*(C9), 179–193, 1990.

Gent, P. R., The Gent-McWilliams parameterization: 20/20 hindsight, *Ocean Modelling*, *39*(1-2), 2–9, 2011.

Gent, P. R., Effects of Southern Hemisphere wind changes on the meridional overturning circulation in ocean models, *Annual Review of Marine Science*, pp. 1–34, 2015.

Gill, A., Atmospheric-ocean dynamics, *Int. Geophys. Ser.*, *30*, 662, 1982.

Gill, A., J. Green, and A. Simmons, Eddy partition in the large-scale ocean circulation and the production of mid-ocean eddies, *Deep Sea Research Part A. Oceanographic Research Papers*, *21*, 499–528, 1974.

Gnanadesikan, A., A simple predictive model for the structure of the oceanic pycnocline, *Science*, *283*(5410), 2077–2079, 1999.

Gnanadesikan, A., and R. W. Hallberg, On the relationship of the circumpolar current to Southern Hemisphere winds in coarse-resolution ocean models, *Journal of Physical Oceanography*, *30*, 2013–2034, 2000.

Griffies, S. M., C. W. Böning, F. O. Bryan, E. P. Chassignet, R. Gerdes, H. Hasumi, A. Hirst, A.-M. Tréguier, and D. Webb, Developments in ocean climate modelling, *Ocean Modelling*, *2*(3), 123–192, 2000.

Hallberg, R. W., and A. Gnanadesikan, The role of eddies in determining the structure and response of the wind-driven Southern Hemisphere overturning: Results from the Modeling Eddies in the Southern Ocean (MESO) project, *Journal of Physical Oceanography*, *36*(12), 2232–2252, 2006.

Haney, R. L., Surface thermal boundary condition for ocean circulation models, *Journal of Physical Oceanography*, *1*(4), 241–248, 1971.

Hausmann, U., A. Czaja, and J. Marshall, Estimates of air-sea feedbacks on sea surface temperature anomalies in the Southern Ocean, *Journal of Climate*, *29*(2), 439–454, 2016.

Hidaka, K., and M. Tsuchiya, On the antarctic circumpolar current, *Journal of Marine Research*, *12*(2), 214, 1953.

Hill, C., D. Ferreira, J.-M. Campin, J. Marshall, R. Abernathey, and N. Barrier, Controlling spurious diapycnal mixing in eddy-resolving height-coordinate ocean models–Insights from virtual deliberate tracer release experiments, *Ocean Modelling*, *45*, 14–26, 2012.

Hogg, A., An Antarctic Circumpolar Current driven by surface buoyancy forcing, *Geophysical Research Letters*, *37*(23), n/a–n/a, 2010.

Hogg, A., M. P. Meredith, D. P. Chambers, E. P. Abrahamsen, C. W. Hughes, and A. K. Morrison, Recent trends in the Southern Ocean eddy field, *Journal of Geophysical Research*, *120*(1), 257–267, 2015.

Ilcak, M., A. J. Adcroft, S. M. Griffies, and R. W. Hallberg, Spurious dianeutral mixing and the role of momentum closure, *Ocean Modelling*, *4546*, 37–58, 2012.

Jansen, M. F., and L.-P. Nadeau, The effect of Southern Ocean surface buoyancy loss on the deep ocean circulation and stratification, *Journal of Physical Oceanography*, pp. JPO–D–16–0084.1, 2016.

Jansen, M. F., A. J. Adcroft, R. W. Hallberg, and I. M. Held, Parameterization of eddy fluxes based on a mesoscale energy budget, *Ocean Modelling*, *92*, 28–41, 2015.

Johnson, G. C., and H. L. Bryden, On the size of the Antarctic Circumpolar Current, *Deep Sea Research Part A. Oceanographic Research Papers*, *36*(1), 39–53, 1989.

Kang, D., and O. Fringer, On the calculation of available potential energy in internal wave fields, *Journal of Physical Oceanography*, *40*(11), 2539–2545, 2010.

Kara, A. B., P. A. Rochford, and H. E. Hurlburt, An optimal definition for ocean mixed layer depth, *Journal of Geophysical Research*, *105*(C7), 16,803–16,821, 2000.

Karsten, R., H. Jones, and J. Marshall, The role of eddy transfer in setting the stratification and transport of a circumpolar current, *Journal of Physical Oceanography*, *32*(1), 39–54, 2002.

Kazantsev, E., Optimal boundary conditions for ORCA-2 model, *Ocean Dynamics*, *63*(8), 943–959, 2013.

Kuo, A., A. Plumb, and J. Marshall, Transformed Eulerian-mean theory. Part II: Potential vorticity homogenization and the equilibrium of a wind-and buoyancy-driven zonal flow, *Journal of physical oceanography*, *35*(2), 175–187, 2005.

Landschützer, P., et al., The reinvigoration of the Southern Ocean carbnon sink, *Science*, *349*(6253), 1221–1224, 2012.

Large, W. G., and S. G. Yeager, The global climatology of an interannually varying air - Sea flux data set, *Climate Dynamics*, *33*(2-3), 341–364, 2009.

Large, W. G., J. C. McWilliams, and S. C. Doney, Oceanic vertical mixing - A review and a model with a nonlocal boundary-layer parameterization, *Reviews of Geophysics*, *32*(94), 363–403, 1994.

Le Quéré, C., et al., Saturation of the Southern Ocean CO₂ sink due to recent climate change, *science*, *316*(5832), 1735–1738, 2007.

Legg, S., and J. C. McWilliams, Convective modifications of a geostrophic eddy field*, *Journal of Physical Oceanography*, *31*(4), 874–891, 2001.

Lorenz, E. N., Energy and numerical weather prediction, *Tellus*, *12*(4), 364–373, 1960.

Madec, G., and P. Delecluse, Institut Pierre Simon Laplace Ocean General Circulation Model reference manual, *Tech. rep.*, 1998.

Marshall, D. P., Subduction of water masses in an eddying ocean, *Journal of Marine Research*, *55*(2), 201–222, 1997.

Marshall, J., and T. Radko, Residual-mean solutions for the Antarctic Circumpolar Current and its associated overturning circulation, *Journal of Physical Oceanography*, *33*(11), 2341–2354, 2003.

Marshall, J., and K. Speer, Closure of the meridional overturning circulation through Southern Ocean upwelling, *Nature Geoscience*, *5*, 171–180, 2012.

McWilliams, J. C., and G. Danabasoglu, Eulerian and eddy-induced meridional overturning circulations in the tropics, *Journal of Physical Oceanography*, *32*, 2054–2071, 2002.

Meredith, M. P., and A. Hogg, Circumpolar response of Southern Ocean eddy activity to a change in the Southern Annular Mode, *Geophysical Research Letters*, *33*(16), 2006.

Meredith, M. P., and P. L. Woodworth, Sustained monitoring of the Southern Ocean at Drake Passage: Past achievements and future priorities, *Reviews of ...*, (2010), 1–36, 2011.

Meredith, M. P., A. C. Naveira Garabato, A. Hogg, and R. Farneti, Sensitivity of the overturning circulation in the Southern Ocean to decadal changes in wind forcing, *Journal of Climate*, *25*(1), 99–110, 2012.

Mignone, B. K., A. Gnanadesikan, J. L. Sarmiento, and R. D. Slater, Central role of Southern Hemisphere winds and eddies in modulating the oceanic uptake of anthropogenic carbon, *Geophysical Research Letters*, *33*(1), 2006.

Moore, G., and I. Renfrew, An assessment of the surface turbulent heat fluxes from the NCEP NCAR reanalysis over the western boundary currents, *Journal of Climate*, pp. 2020–2037, 2002.

Morrison, A. K., and A. Hogg, On the relationship between Southern Ocean overturning and ACC transport, *Journal of Physical Oceanography*, *43*(1), 140–148, 2013.

Munday, D. R., L. C. Allison, H. L. Johnson, and D. P. Marshall, Remote forcing of the Antarctic Circumpolar Current by diapycnal mixing, *Geophysical Research Letters*, *38*(January), 2–5, 2011.

Munk, W. H., and E. Palmén, Note on the dynamics of the Antarctic Circumpolar Current, *Tellus*, *3*(1), 53–55, 1951.

Naveira Garabato, A. C., Cruise Report N0. 35 RRS James Cook Cruise 29. 01 Nov - 22 Dec 2008 SOFine cruise report: Southen Ocean fine structure principal scientist A Naveira Garabato, *Tech. rep.*, 2009.

Nikurashin, M., and G. Vallis, A Theory of the interhemispheric meridional overturning circulation and associated stratification, *Journal of Physical Oceanography*, *42*, 1652–1667, 2012.

Nurser, A., and M. Lee, Isopycnal averaging at constant height. Part I: The formulation and a case study, *Journal of physical oceanography*, pp. 2721–2739, 2004.

Pauluis, O., T. Shaw, and F. Laliberté, A statistical generalization of the Transformed Eulerian-Mean circulation for an arbitrary vertical coordinate system, *Journal of the Atmospheric Sciences*, *68*(8), 1766–1783, 2011.

Pedlosky, J., Geophysical fluid mechanics, 1987.

Pellichero, V., J.-B. Sallée, C. C. Chapman, and S. M. Downes, The southern ocean meridional overturning in the sea-ice sector is driven by freshwater fluxes, *Nature Communications*, pp. 1–9, 2018.

Plumb, A., and R. Ferrari, Transformed Eulerian-mean theory. Part I: Nonquasigeostrophic theory for eddies on a zonal-mean flow, *Journal of physical oceanography*, pp. 165–174, 2005.

Prather, M., Numerical advection by conservation of second order moments, *Geophysical Research Letters*, *91*(D1), 6671–6681, 1986.

Rintoul, S. R., et al., *The Southern Ocean observing system: initial science and implementation strategy*, Scientific Committee on Antarctic Research, 2012.

Rosso, I., A. Hogg, A. E. Kiss, and B. Gayen, Topographic influence on submesoscale dynamics in the Southern Ocean, *Geophysical Research Letters*, *42*, 1139–1147, 2015.

Saenz, J. a., A. Hogg, G. O. Hughes, and R. Griffiths, Mechanical power input from buoyancy and wind to the circulation in an ocean model, *Geophysical Research Letters*, *39*(13), 2012.

Sallée, J.-B., K. Speer, S. R. Rintoul, and S. Wijffels, Southern ocean thermocline ventilation, *Journal of Physical Oceanography*, *40*, 509–529, 2010.

Shakespeare, C. J., and A. Hogg, An analytical model of the response of the meridional overturning circulation to changes in wind and buoyancy forcing, *Journal of Physical Oceanography*, *42*(8), 1270–1287, 2012.

Smith, W., and D. Sandwell, Global sea floor topography from satellite altimetry and ship depth soundings, *Science*, *80*, 80–90, 1997.

Speer, K., S. R. Rintoul, and B. Sloyan, The Diabatic Deacon Cell*, *Journal of physical oceanography*, *30*(12), 3212–3222, 2000.

Stewart, A. L., R. Ferrari, and A. F. Thompson, On the importance of surface forcing in conceptual models of the deep ocean, *Journal of Physical Oceanography*, *44*(3), 891–899, 2014.

Taylor, G., Eddy Motion in the Atmosphere, *Royal Society*, *CXCIV*(a), 1–26, 1914.

Taylor, G., Stability of a Viscous Liquid Contained between Two Rotating Cylinders Author, *Royal Society*, *223*(a), 289–343, 1922.

Thompson, A. F., The atmospheric ocean: eddies and jets in the Antarctic Circumpolar Current, *Philosophical Transactions of the Royal Society A: Mathematical, Physical and Engineering Sciences*, *366*(1885), 4529–4541, 2008.

Thompson, A. F., and J.-B. Sallée, Jets and topography: jet transitions and the impact on transport in the Antarctic Circumpolar Current, *Journal of Physical Oceanography*, *42*, 956–972, 2012.

Thompson, D. W. J., and S. Solomon, Interpretation of recent Southern Hemisphere climate change, *Science*, *296*(5569), 895–899, 2002.

Toggweiler, J. R., and J. L. Russell, Ocean circulation in a warming climate., *Nature*, *451*(17), 286–288, 2008.

Tréguier, A.-M., I. M. Held, and V. D. Larichev, Parameterization of quasigeostrophic eddies in primitive equation ocean models, *Journal of Physical Oceanography*, *27*(4), 567–580, 1997.

Tréguier, A.-M., M. England, S. R. Rintoul, G. Madec, J. Le Sommer, J.-M. Molines, and Others, Southern Ocean overturning across streamlines in an eddying simulation of the Antarctic Circumpolar Current, *Ocean Science Discussions*, *4*(4), 653–698, 2007.

Viebahn, J., and C. Eden, Standing eddies in the meridional overturning circulation, *Journal of Physical Oceanography*, *42*(9), 1486–1508, 2012.

Visbeck, M., J. Marshall, T. Haine, and M. Spall, Specification of eddy transfer coefficients in coarse-resolution ocean circulation models*, *Journal of Physical Oceanography*, *27*(3), 381–402, 1997.

von Storch, J.-S., C. Eden, I. Fast, H. Haak, D. Hernández-Deckers, E. Maier-Reimer, J. Marotzke, and D. Stammer, An estimate of Lorenz energy cycle for the world ocean based on the 1/10 degree STORM/NCEP simulation, *Journal of Physical Oceanography*, *42*(1992), 120821111920,009, 2012.

Winters, K. B., and W. R. Young, Available potential energy and buoyancy variance in horizontal convection, *Journal of Fluid Mechanics*, *629*, 221–230, 2009.

Wolfe, C. L., Approximations to the ocean's residual circulation in arbitrary tracer coordinates, *Ocean Modelling*, *75*(0), 20–35, 2014.

Wolfe, C. L., and P. Cessi, Overturning circulation in an eddy-resolving model: The effect of the pole-to-pole temperature gradient, *Journal of Physical Oceanography*, *39*, 125–142, 2009.

Wolfe, C. L., and P. Cessi, The adiabatic pole-to-pole overturning circulation, *Journal of Physical Oceanography*, *41*(9), 1795–1810, 2011.

Wolfe, C. L., P. Cessi, J. L. McClean, and M. E. Maltrud, Vertical heat transport in eddying ocean models, *Geophysical Research Letters*, *35*(23), L23,605, 2008.

Wunsch, C., and R. Ferrari, Vertical mixing, energy, and the general circulation of the oceans, *Annual Review of Fluid Mechanics*, *36*(1), 281–314, 2004.

Zhai, X., and D. R. Munday, Sensitivity of Southern Ocean overturning to wind stress changes: Role of surface restoring time scales, *Ocean Modelling*, *84*, 12–25, 2014.

Appendices

A Example datafile

To give a full overview of the parameters used in the standard model set up below is an example data input file with the run time model flags and in italics a brief explanation.

& **PARM01**

tRef=Reference Profile, *This the reference temperature for EOS, setting the sponge profile*

viscosity

viscAh=12.000000, *Laplacian viscosity coefficient (m^2/s) Set so that horizontal Reynolds number is 0, this scales with resolution of one less than the order (so linearly here) - basically it is to ensure that the velocity is not too fast that a wave can pass through a cell in less than one time step with the scaling relation $A_h < \frac{L^2}{4\Delta t}$ (Courant-Freidrichs-Lewy Constraint on viscosity). Griffies et al. (2000) notes that it actually scales to one less power.*

viscAz=0.000300,*vertical eddy coefficient. default*

viscA4=9.0E8,*Bi-harmonic viscosity coefficient (m^4/s) With the relation $A_4 <= \frac{L^4}{32\Delta t}$.* Allows a less viscous yet numerically stable simulation than harmonic (laplacian) as eddy viscosities can be focuses on the dynamics at the grid scale as large motions would be 'resolved'.

viscA4GridMax=0.500*Maximum grid dependent biharmonic viscosity*

viscAhGridMax=0.500*Maximum lateral grid dependent eddy viscosity*

Diffusion

diffKhT=0.000000,*Laplacian diffusion of heat laterally (m^2/s) the boundary condition on this operator is $\frac{\partial}{\partial x} = \frac{\partial}{\partial y} = 0$ on all boundaries. Default.*

diffKzT=0.00000, *Laplacian diffusion of salt vertically can be set implicitly by setting implicitDiffusion to .TRUE. Default.*

diffKhS=0.000000,*Laplacian diffusion of salt laterally (m^2/s) same applies as for T. Default.*

diffKzS=0.00000,*Laplacian diffusion of salt vertically (m^2/s) same applies as for S. Default.*

Advection Scheme

tempAdvScheme=7,*The seventh-order one-step method with monotonicit-preserving limiter (OS7MP) (Daru and Tenaud, 2004) and minimises numerical diffusion (Ilcak et al., 2012; Shakespeare and Hogg, 2012)*

Timestepping

StaggerTimeStep=.TRUE.,*Staggered baroclinic time stepping rather than synchronous time stepping. The thermodynamics solver is delayed from half a time step, allowing the use of the most recent velocities to compute the advection terms*

saltStepping=.FALSE.,*Salinity equation off.*

equation of state

eosType='LINEAR',*Sets linear EOS, buoyancyRelation is automatically set to OCEANIC. For the nonlinear case, you need to generate a le of polynomial coefficients called POLY3.COEFFS. To do this, use the program utils/knudsen2/knudsen2.f instead of tAlpha and sBeta*

tAlpha=2.0E-4,*thermal expansion coefficient in* K^{-1} *for EOS. Default.*

sBeta =0.,*salt is passive here* (ppt^{-1})

Boundary conditions

no_ slip_ sides=.TRUE., *Free slip or no slip. Free slip give zero stress on boundaries (more convenient to code). No slip defines the normal gradient of a tangential flow such that the flow is zero on the boundary by adding an additional source term in cells next to the boundary*

no_ slip_ bottom=.TRUE.,

bottomDragLinear=1.1E-03,*linear bottom-drag coefficient (m/s)*

bottomDragQuadratic=0.000000E+00,*quadratic bottom-drag coeff. Default.*

physical parameters

f0=-1.E-4,*Coriolis parameter* (s^{-1})*,* $f = 2\omega sin\phi$ *Here this is set to the negative reference value and as beta is non zero f0 is the value of f at the southern edge of the domain.*

beta=1E-11,$\frac{\partial f}{\partial y}$ $(m^{-1}s^{-1})$

gravity=9.81,

exact volume conservation

exactConserv=.TRUE.,

C-V scheme for Coriolis term

useCDscheme=.FALSE.,

partial cells for smooth topography

HfacMin=0.05, *Limit partial cells to 50m thickness*

file I/O parameters

readBinaryPrec=64,*double precision*

useSingleCpuIO=.TRUE.,

debugLevel=1,

Default surface conditions

rigidLid=.FALSE.,

implicitFreeSurface=.TRUE.,*these lines suppress the rigid lid formulation of the surface pressure inverter and activate the implicit free surface form of the pressure inverter.*

&

& PARM02

cg2dMaxIters=500,*Upper limit on 2d con. grad iterations, default is 150.*

cg2dTargetResidual=1.E-9, *default is 1.E-7*

cg3dMaxIters=40,*Sets the maximum number of iterations the three-dimensional, conjugate gradient solver*

cg3dTargetResidual=1.E-9,

&

& PARM03

deltaT=450,*time steps scales with resolution*

7.5 minute time step: 69120 time steps/year

nIter0=0,*Start at..*

nTimeSteps=1382400,*20 years*

cAdjFreq = -1.,*Convective adjustment interval (s), the frequency at which the adjustment algorithm is called to a non-zero value, a negative value sets to tracer time step*

abEps=0.1, *Adams-Bashforth stabilizing parameter, required as staggerTimeStep is set to TRUE*

Permanent restart/checkpoint file interval (s)

Try 10 year interval (two per run)

pChkptFreq=311040000.00,*Checkpoint file interval (s)*

dumpFreq=0.0, *Model state write out interval (s)*

monitorFreq=0.0, *Monitor output interval (s)*

dumpInitAndLast=.TRUE.,

pickupStrictlyMatch=.FALSE.,

&

& PARM04

usingCartesianGrid=.TRUE., *Uses cartesian co-ordinate system with uniform grid space via dXspacing or dYspacing or by vectors DelX or DelY in (m)*

usingSphericalPolarGrid=.FALSE.,

delXfile='delX', *Can be set as a 1D array file or as gridlines * spacing i.e 300*5E3 300 grid lines at 5km spacing*

delYfile='delY',

delZfile='delZ'

&

& PARM05

surfQfile='Qsurface'

bathyFile='topog'

zonalWindFile='Wind',

meridWindFile=,

hydrogThetaFile='T.init',

&

B Example Gendata.py

Gendata_Nchannel_Surface_restoring_wQ

August 1, 2017

1 Generate model inputs

1.1 This will set up the forcing for Abernathey Style Forcing

This is an example python script for generating the standard channel model, with additional surface restoring.

```
In [1]: import numpy as np
        import matplotlib.pyplot as plt
        import os
        import csv
        import netCDF4
        import sys
        import math
        from pylab import *
        from IPython.display import display, Math, Latex
        from numba import jit
        import glob
        %matplotlib inline
        # Use writeFile to write files in the correct format!
        sys.path.append('/noc/users/hb1g13/Python/python_functions/')
        from Writebin import *
        import SG
        sys.path.append('/noc/users/hb1g13/Python/python_functions/MITgcmUtils/')
        import utils
```

When writing in python it is very important to note reverse dimensions!! MITgcm assumes column major order (as does matlab) Python, uses row major order. Mosty it's fine just to write straight to binary, but to absolutely specific of the format for MITgcm the WriteFile fuction (taken from the MITgcm csv gendata.py):

1.2 Decide parameters:

Resolution Depth Domain Boundary Condition Topography Forcing

```
In [2]: Topo = "flat"  # Please Choose ridge, slope or flat
        Wind = "Standard"  # Sine bell 0.2N/m$^2$
        Heat = "nonetQ"  # Please Choose Abernathey or nonetQ
```

```
BC = "Sponge"  # Please Choose Sponge or Diffusion
Name = "My_restoring_90wQ"  # Give Experiment Name
N = 1e3 # Set stratification
deltaT0 = 8 # top to bottom temp diff
N0 = 1000 # Natural stratification
```

In [3]:
```
# Adjust accordingly
Res = 5000 # Resolution (m)
Ly = 2000e3 # Domain legth
Lx = 1000e3 #Full domain = 4000km otherwise 1000km
H = 3000.0 # Depth
nz = 30 # Diffusion = 24 level, Sponge= 30 levels
```

In [4]:
```
# File structure
x = ( os.path.expanduser('~')+"/MITgcm/"+Name+"/input/")
if not os.path.exists(x):
       os.makedirs(x)
os.chdir(x)
```

1.3 Set up grid:

In [5]:
```
#Dimensions
nx = int(np.round(Lx/Res))
ny = int(np.round(Ly/Res))
dx = np.ones(nx)*Res
dy = np.ones(ny)*Res
#Write binary output
writeFile('delY',dy)
writeFile('delX',dx)
# Create c-grid with grid points in dead center
x = (np.cumsum(dx)-dx/2)-Lx/2
y = (np.cumsum(dy)-dy/2)-Ly/2
[Y, X] = np.meshgrid(y, x)
```

1.4 Now Create topography:

Start with flat, then add slope and ridges

In [6]:
```
h= -H*np.ones((nx,ny)) # Flat bottom
if Topo == "ridge":#2500 and 2000 for full depth
        h= h+((2500 + 300*np.sin(10*pi*Y/Ly) + 400*np.sin(8*pi*Y/Ly)
              + 300*sin(25*pi*Y/Ly) )*(1/np.cosh(((X)-0.2*Y+3e5)/1.2e5)))
        h= h+((2000 + 600*np.sin(11*pi*Y/Ly) + 300*np.sin(7*pi*Y/Ly)+
              500*sin(21*pi*Y/Ly) )*(1/np.cosh(((X)+0.1*Y+1.5e6)/1.2e5)))
if Topo == "slope" or Topo=="ridge":
    for i in range(int(nx)):
        slope= np.transpose(H*(np.divide((Y[i,0:round(0.2*ny)]
                                          -Y[i,0]),(Y[i,0]-Y[i,round(0.2*ny)])))))
        h2 = h[:,0:round(0.2*ny)]
```

```
            h[:,0:round(0.2*ny)]=np.maximum(slope,h2)
    # Close both ends
    h[:,0] = 0
    h[:,-1] = 0
    # Write to binary
    writeFile('topog',np.transpose(h))
```

In [7]:
```
fig1 = plt.figure()
if Topo == "flat" or Topo == "slope":
    plt.plot(y/1000,h[nx/2,:])
    plt.title('Topography')
    plt.ylabel('Depth (m)')
    plt.xlabel('Y (km)')
if Topo == 'ridge':
    # plt.contourf(x/1000,y/1000,np.transpose(h),30)
    plt.contourf(np.transpose(h))
    cb = plt.colorbar()
    plt.title('Topography')
    plt.ylabel('Y (km)')
    plt.xlabel('X (km)')
    cb.set_label('Depth (m)')
# netcdf check
f = netCDF4.Dataset('topog.nc','w')
f.createDimension('X',nx)
f.createDimension('Y',ny)
h2=f.createVariable('h','float',('X','Y'))
h2[:] = h
f.close()
```

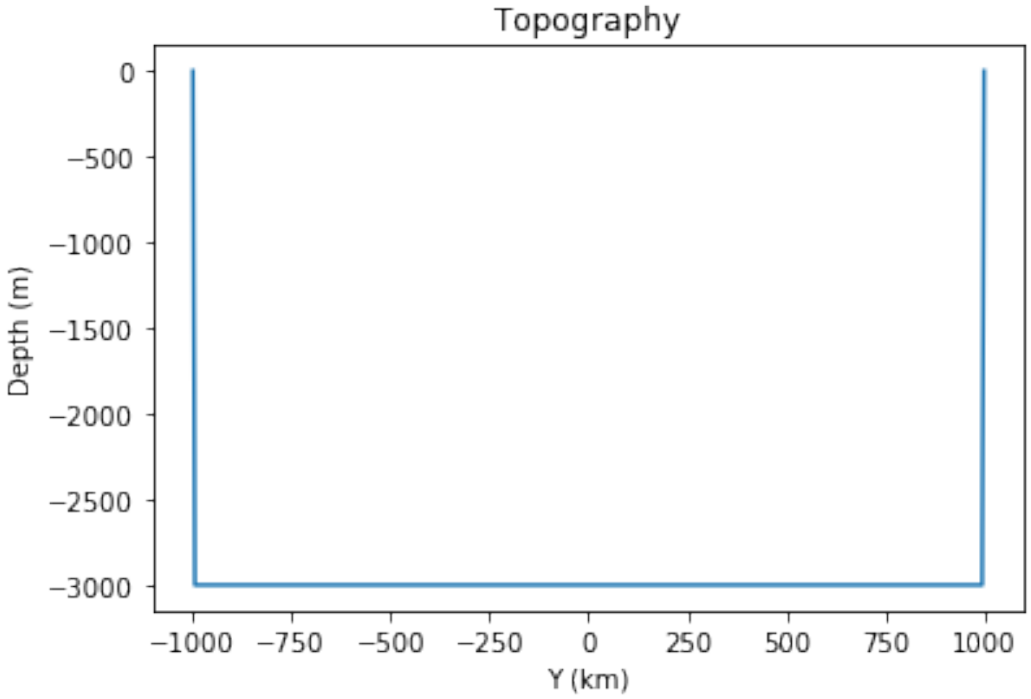

1.5 Windstress

Plus the Windress with τ_o set to $0.2Nm^-2$

$\tau_s(y) = \tau_0 sin(\frac{\pi y}{Ly})$

```
In [8]: tau=0.2*((np.sin((Y+Ly/2)*(pi/Ly)))) #Y is centred at 0 so put that back!
        if BC=='Diffusion':
            Taunew = tau + 2e-3 * (np.random.random((nx,ny)) - 0.5)
            tau=Taunew
        # Write to binary
        writeFile('Wind',np.transpose(tau))
        # netcdf check
        f = netCDF4.Dataset('Wind.nc','w')
        f.createDimension('Xp1',nx+1)
        f.createDimension('Y',ny)
        tau3=np.zeros((ny,nx+1))
        tau3[:,1:]=np.transpose(tau)
        tau2=f.createVariable('tau','double',('Xp1','Y'))
        tau2[:]=np.transpose(tau3)
        f.close()
```

```
In [9]: plt.plot(y/1000,tau[100,:])
        plt.title('Surface Wind Stress $N/m^2$')
        plt.ylabel('$\tau$ ($N/m^2$)')
        plt.xlabel('Meridional Distance (m)')
```

Out[9]: <matplotlib.text.Text at 0x2ab848301b50>

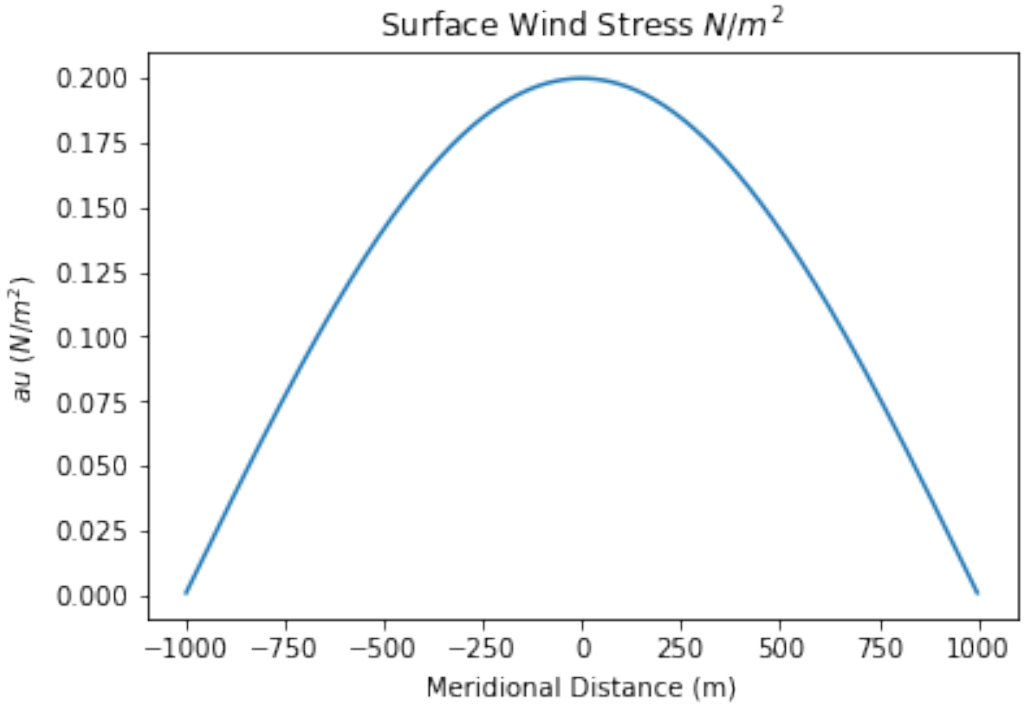

In [10]:
```
#MITgcm opposite way round
Q_0 = 2
Q=Q_0*(np.sin(Y*(3*pi/Ly)))
Q[:,ny-(np.round(ny/6)):ny]=0
x1 = (np.cumsum(dx)-dx/2)
y1 = (np.cumsum(dy)-dy/2)
[Y1, X1] = np.meshgrid(y1, x1)
if Heat=="nonetQ":
    Q[:,0:int(5*ny/36)]=Q_0*(np.cos(Y1[:,0:int(5*ny/36)]*(pi/(Y1[1,int(10*ny/36)]))))
    Q[:,int(5*ny/36):int(20*ny/36)]= -Q_0*(np.sin((Y1[:,int(5*ny/36):int(20*ny/36)]
                                                   -Y1[1,int(5*ny/36)])*(pi/(Y1[1,int(15*
    Q[:,int(20*ny/36):int(30*ny/36)]= Q_0*(np.sin(Y1[:,0:int(10*ny/36)]*(pi/(Y1[1,int(1
    Q[:,0:int(30*ny/36)] = Q[:,0:int(30*ny/36)]+(-sum(Q)/(5*ny*nx/6))
# Write to binary
writeFile('Qsurface',np.transpose(Q))
# netcdf check
f=netCDF4.Dataset('Qsurface.nc','w')
f.createDimension('X',nx)
f.createDimension('Y',ny)
Q2=f.createVariable('Q','float',('X','Y'))
Q2[:]=Q
f.close()
```

```
In [11]: fig1 = plt.figure()
         plt.plot(y/1000,Q[100,:])
         plt.title('Surface Heat Flux $W/m^2$')
         plt.ylabel('Heat Flux ($W/m^2$)')
         plt.xlabel('Meridional Distance (m)')

Out[11]: <matplotlib.text.Text at 0x2ab866ade690>
```

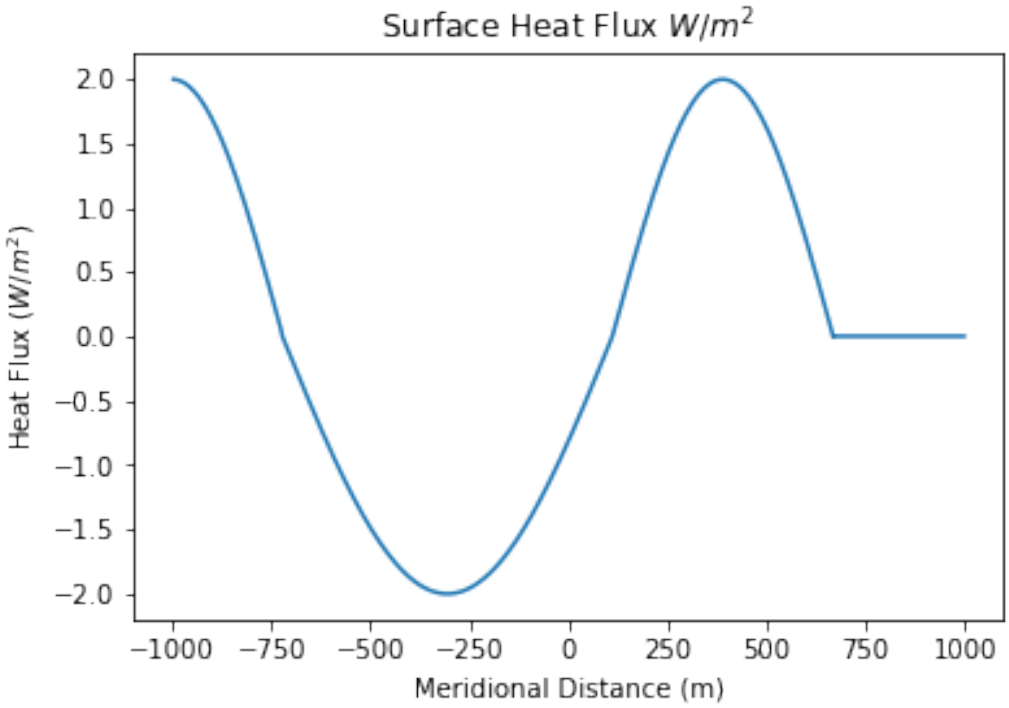

1.6 Generate Sponge

Now creat a Sponge mask and a reference profile to relax to:

```
In [12]: # Parameters
         deltaT = deltaT0#-((N-N0)/N0)
         Tref = np.zeros(nz)
         # Create depth array:
         # Tanh - normal
         zp = np.linspace(1,0,31)
         zp = H+H*1.0153*(tanh(-0.9*pi*zp))
         zp = zp - zp[0]-(zp[1]-zp[0])
         zp = np.round(zp,2)
         dz = zp[0:-1] - zp[1::]
         dz[-3::] = dz[-3]
         zp[-1] = H
```

```
zp[1::] = np.cumsum(np.round(dz))
zp[0] = 0.5*zp[0]
writeFile('delZ',-dz)
# Z center points
z = zeros((nz))
z[1::] = (zp[1:-1]+zp[2::])/2
z[0]= zp[0]/2
```

```
In [13]: print  ",".join(map(str,-dz))
```

```
4.39,5.29,6.38,7.68,9.25,11.13,13.38,16.08,19.31,23.14,27.7,33.11,39.49,46.98,55.73,65.88,77.56,
```

$$T^*(z) = \Delta T \frac{(e^{z/N} - e^{-H/N})}{1 - e^{-H/N}} + \left(\frac{N - N_0}{N_0}\right), \tag{1}$$

N max = H

```
In [14]: Tref = deltaT*(exp(z/N)-exp(-H/N))/(1-exp(-H/N))+2*((N-NO)/NO)
         if N >= H:
             deltaT = 8 -((H-NO)/NO)
             Tref = deltaT*(exp(z/N)-exp(-H/N))/(1-exp(-H/N))+1+((H-NO)/NO)
```

```
In [15]: plt.plot(Tref,z)
         print 'max: ', np.max(Tref), '\n min: ', np.min(Tref)
         #plt.gca().invert_yaxis()
         plt.title('Temperature Profile')
         plt.ylabel('Depth (m)')
         plt.xlabel('Temperature $^oC$')
```

```
max:  7.9907650344
 min:  0.0605848438775
```

```
Out[15]: <matplotlib.text.Text at 0x2ab866adee50>
```

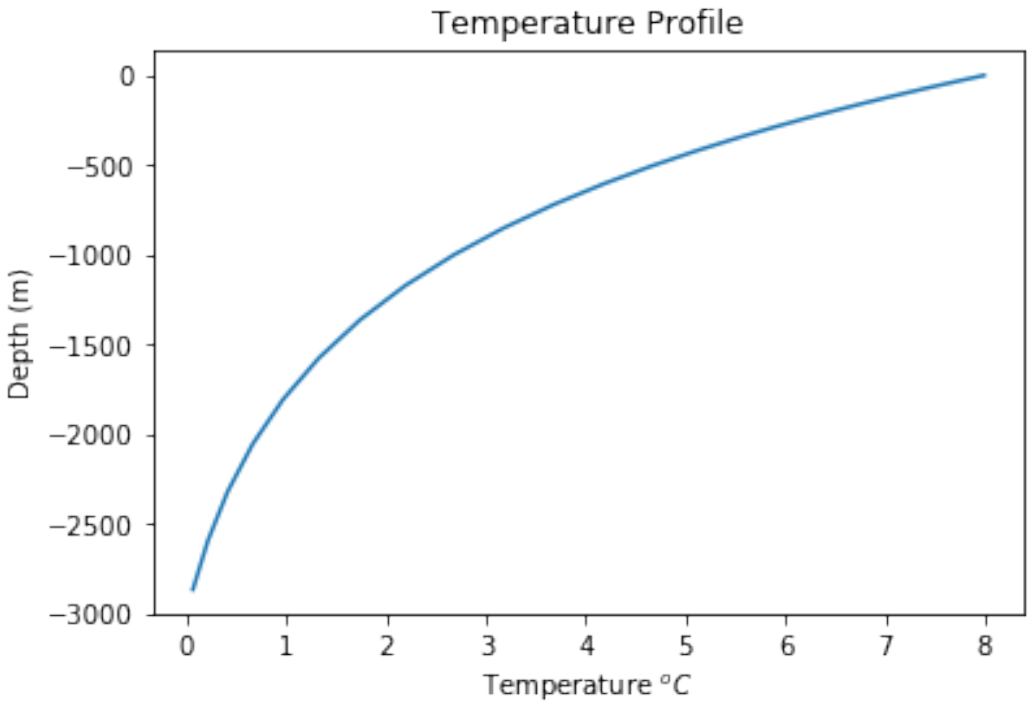


```
In [16]: #Make a 3D array of it
         T=np.ones((nz,ny,nx))
         Temp_field=np.zeros(np.shape(T))
         for i in range(int(nx)):
             for j in range(int(ny)):
                 Temp_field[:,j,i]=np.multiply(Tref,T[:,j,i])
```

```
In [17]: Tnew = transpose(tile(Temp_field.mean(axis=2),(nx,1,1)),[1,2,0])
         Tnew[:,-1] = Tnew[:,-2]
         #Maybe add more
         if BC=='Diffusion':
             Tnew = Tnew + 2e-3 * (np.random.random((nz,ny,nx)) - 0.5)
         else:
             Tnew = Tnew + 1e-3 * (np.random.random((nz,ny,nx)) - 0.5)
```

1.7 Surface restoring

$$T_s = T_{ref} - \frac{Q}{\rho C_p \lambda \Delta z} \tag{2}$$

```
In [18]: x = '/noc/msm/scratch/students/hb1g13/Mobilis'
         fname = x+'/3daynokpp/'
         c = utils.ChannelSetup(output_dir=str(fname))
         Tavlat = c.get_zonal_avg('Tav.nc','THETA')
```

```
Tref = Tavlat[0,:]
Tref[-1] = Tref[-2]
Tref[0] = 0
Q = c.mnc('SURF.nc', 'oceQnet').mean(axis=0).mean(axis=1)
rho = 1030.0
Cp = 3985.0
lamba = 1.0/(90*24*60*60)
dz = c.dzf[0]
Ts = Tref - Q/(rho*Cp*lamba*dz)
#Ts[-1] = Ts[-2]
Ts[0:40] = np.arange(0.0,2.,0.05)
Ts = SG.savitzky_golay(Ts,21,1) # Smooth just a little!
plt.plot(Ts,c.yc/1000)
plt.title('Surface Temperature',fontsize=20)
plt.ylabel('y (km)')
plt.xlabel('Temp $^o$ C')
Tsxy = np.tile(Ts,(nx,1))
Temp_field[0,:,:] = Tsxy.T
```

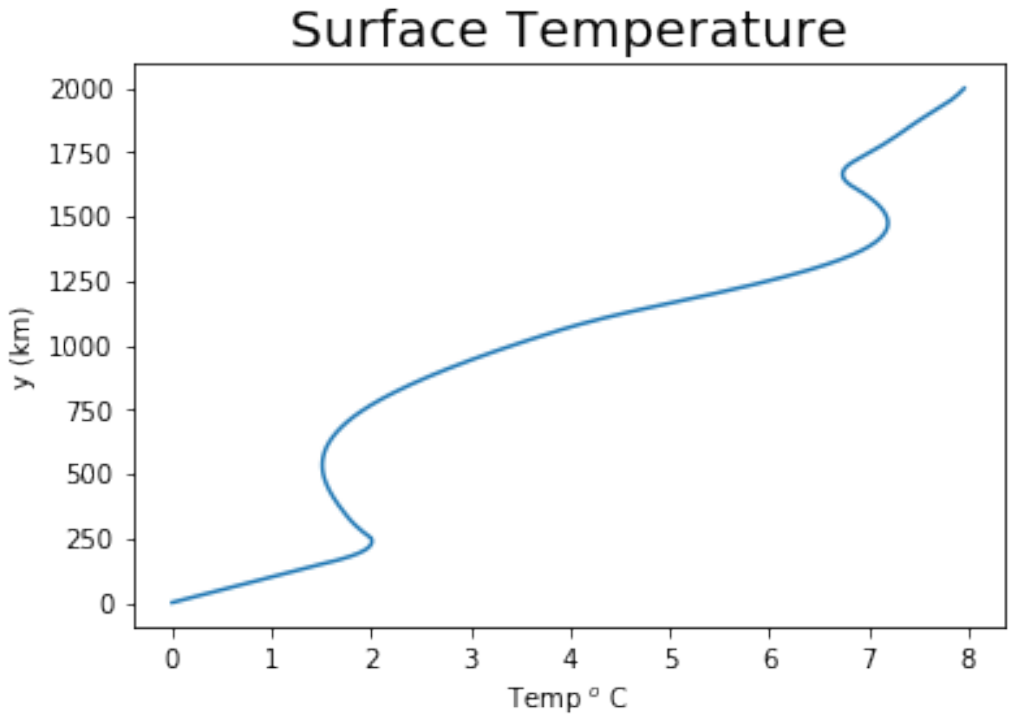

In [19]:
```
# Write to binary
writeFile('T_Sponge',Temp_field)
writeFile('T.init',Tnew)
# netcdf check
```

```
f = netCDF4.Dataset('TSponge.nc','w')
f.createDimension('X',nx)
f.createDimension('Y',ny)
f.createDimension('Z',nz)
Temp=f.createVariable('Temp','double',('Z','Y','X'))
Temp[:]=Temp_field
f.close()
```

In [25]:
```
#Make 3D mask
#Must vary between 0 (no Relaxation) and 1 (full relaxtion)
#I have gone for a parabolic decay in x and linear decay in z (from playing around)
msk = np.zeros(np.shape(T))
for k in range(0,len(z)):
    for i in range(nx):
        msk[k,ny-20:ny,i]=((np.divide((Y[i,ny-21:ny-1]-Y[i,ny-21]),(Y[i,ny-1]-Y[i,ny-21
msk[0,:,:] = 1
# Write to binary
writeFile('T.msk',msk)
# netcdf check
f = netCDF4.Dataset('Mask.nc','w')
f.createDimension('X',nx)
f.createDimension('Y',ny)
f.createDimension('Z',nz)
Mask=f.createVariable('Mask','double',('Z','Y','X'))
Mask[:]=(msk)
f.close()
```

In [26]:
```
plt.contourf(y/1000,z[0:5],msk[0:5,:,100],24,cmap=cm.plasma_r)
cbar = plt.colorbar()
plt.gca()#.invert_yaxis()
plt.title('Mask Matrix')
plt.ylabel('Depth (m)')
plt.xlabel('Meridional Distance (km)')
```

Out[26]:
```
<matplotlib.text.Text at 0x2ab86bdc05d0>
```

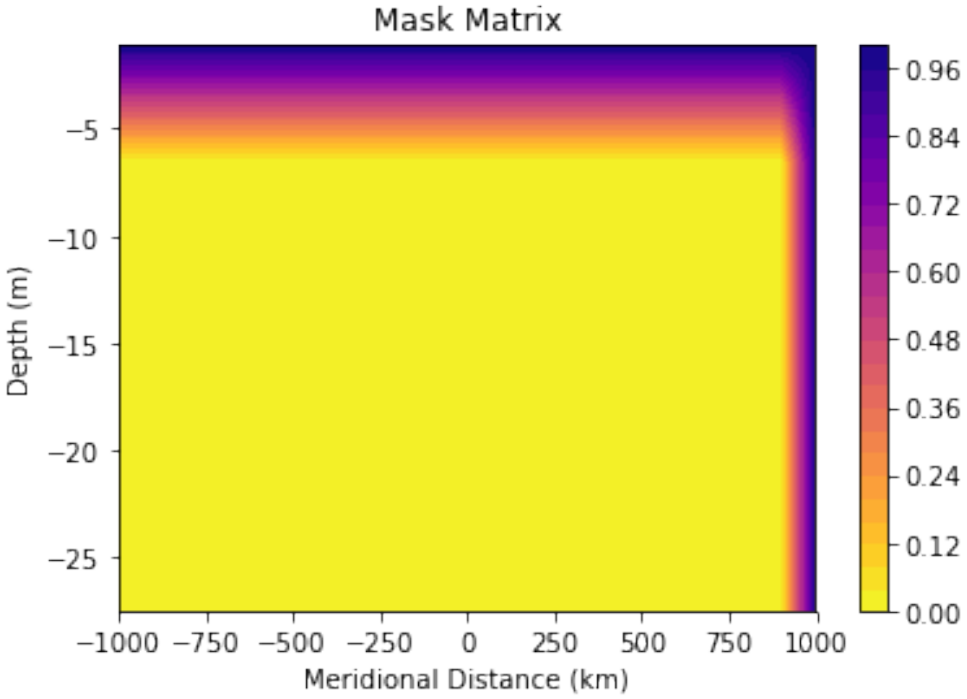
Mask Matrix
Depth (m)
−5
−10
−15
−20
−25
−1000
−750
−500
−250
0
250
500
750
1000
Meridional Distance (km)
0.96
0.84
0.72
0.60
0.48
0.36
0.24
0.12
0.00

C Advective assumptions on model grid

Here we demonstrate, by using a one dimensional example of Eq. 2.7, that this equation is not valid on the model grid. In our model runs, we used the MITgcm advection scheme 7 (*Daru and Tenaud*, 2004) with modifications from Adcroft and Campin, (MITgcm support mailing list communications 2010). This is a one step monotonicity-preserving 7th order scheme. Referring to *Adcroft et al.* (2004) and MITgcm model code (*Marshall*, 1997), for a 1-D advection problem in the y-direction for a tracer Q the discrete fluxes become:

$$\frac{\partial Q}{\partial t} + v\frac{\partial Q}{\partial y} + = \frac{1}{\Delta t}\left(Q_j^{n+1} - Q_j^n\right) + \frac{v}{\Delta y}\Bigg(Q_j^n + \frac{1}{2}(1-C)(Q_{j+1}^n - Q_j^n) - \frac{1}{6}(1-C^2)(Q_{j+1}^n - 2Q_j^n + Q_{j-1}^n) - Q_{j-1}^n - \frac{1}{2}(1-C)(Q_j^n - Q_{j-1}^n) + \frac{1}{6}(1-C^2)(Q_j^n - 2Q_{-j}^n + Q_{j-2}^n)\Bigg) + O^4 \quad (1)$$

where C is the Courant number $\left(\frac{u\Delta t}{\Delta x}\right)$. Monotonicity-preserving flux limiters not described here are also applied. In the MITgcm the advection scheme FORTRAN routine generalises 1-D advection to 3-D by removing the local divergence flow separately in each dimension. Using the identity:

$$v\frac{\partial Q}{\partial y} = \frac{\partial vQ}{\partial y} - Q\frac{\partial v}{\partial y}, \quad (2)$$

This indicates on a discrete model grid Eq. (2.7) would have to be written:

$$\overline{\nabla \cdot \mathbf{u}T} = \overline{\mathbf{u}} \cdot \nabla\overline{T} - \overline{T} \cdot \mathbf{u}, \quad (3)$$

and applying Eq. 2 on a C-grid (Fig. 1.5) Eq. 2.7 does not hold on the model grid i.e:

$$\frac{\partial Q}{\partial t} + v\frac{\partial Q}{\partial y} \neq \frac{\partial vQ}{\partial t} + \frac{\partial vQ}{\partial y} \quad (4)$$